REDOX-COUPLED SPIN CROSSOVER IN COBALT COORIDNATION COMPLEXES

Charles A. McCabe

Submitted in Partial Fulfillment of the Requirements
for the Degree of

DOCTOR OF PHILOSOPHY

Approved by:
Dr. Peter H. Dinolfo, Chair
Dr. Peter J. Bonitatibus
Dr. Jacob T. Shelley
Dr. Vidya Chakrapani

Department of Chemistry and Chemical Biology
Rensselaer Polytechnic Institute
Troy, New York

[May 2024]

© Copyright 2024
By
Charles A. McCabe
All Rights Reserved

TABLE OF CONTENTS

LIST OF TABLES

LIST OF FIGURES

ACKNOWLEDGEMENT

Over the last six years many people have offered their support, friendship, and guidance without which I would not have been able to complete my dissertation. There are too many people deserving of thanks to mention them all here, so with careful consideration I would like to thank the following people.

First, I would like to thank my parents. My mother for her endless and unwavering support and my father, who is no longer with us. He was always an enthusiastic, if awkward supporter. If he could, he would no doubt be waiting at my defense with some kind of corny question once it was all over. And I would like to thank my fiancé, Emily, for her support and encouragement all these years.

I would also like to thank my advisor Dr. Dinolfo for his immense patience and advice over these past six years. The rest of the Dinolfo Lab deserves thanks as well. Even though I cannot name them all here a special thanks to David Hontz, Naomi Robinson, and Tyler Mucci, who were great labmates during times when there were few others to share the office with. I would also like to thank Andrea Mitchell whose contributions were essential to completing parts of this thesis. Thanks are due to each member of my doctoral committee and especially to Dr. Bonitatibus for his invaluable help in obtaining X-ray structures.

I would also like to thank just a few of the friends I have made at RPI including Lauren Gandy, Keith Denivo, Cody Edson, Evelyn Grace-Rugaber, and Matthew Van der Wielen as well as all the members of the Rensselaer Music Association for their hard work creating musical opportunities for busy STEM students. Additional thanks are due to Tristan Wise and all the other Age of Empires players in our weekly sessions.

Finally, I would also like to thank my many brothers in Phi Mu Alpha who are much too numerous to list here. I would specifically like to thank Tyler Youngman, Rian West, Nicholas Rivera, Surya Vaidy, and Dr. Vernon Huff. With whom I have had the pleasure of serving on the board of the Upstate New York Alumni Association

ABSTRACT

Cobalt coordination compounds consisting of a single five-coordinate cobalt(III) salen ($\mathbf{Co^{III}Sln^{+}}$) complex and two cobalt β-diketonate complex $\mathbf{[(Co(acac)_{2}((CC)_{2}bpy)]}$ and $\mathbf{[Co(dbm)_{2}((CC)_{2}bpy)]}$ were synthesized. The redox-coupled spin crossover behavior of these complexes were then studied using electrochemical and spectroscopic methods. $\mathbf{Co^{III}Sln^{+}}$ is high-spin in both its +2 and +3 oxidation states, but its remaining open coordination site allows for exogenous ligands to bind to the +3 oxidation state inducing a high-spin to low-spin transition. This transition is accompanied by changes in color and induces a drastic electrochemical shift. The changes in electrochemistry correlate nicely to the basicity of the ligand as measured by gas phase basicity. For pyridine ligands the shift also correlates to the Hammett parameter of the para substituent. This complex is a notable example of a cobalt complex which undergoes both redox-coupled spin crossover and coordination-induced spin crossover. In pursuit of a better understanding of these interactions a review of similar coordination-induced spin crossover systems was performed. The two β-diketonates also undergo redox-coupled spin crossover. The +2 oxidation states are both high-spin, but upon oxidation a rearrangement takes place that results in a low-spin cobalt(III) metal center. Like $\mathbf{Co^{III}Sln^{+}}$, the high- and low-spin states of $\mathbf{[Co(acac)_{2}((CC)_{2}bpy)]}$ and $\mathbf{[Co(dbm)_{2}((CC)_{2}bpy)]}$ have very different spectral properties. Attempts to fashion electrochromic multilayers out of these complexes were unsuccessful. These failed experiments provided insights into the synthetic modifications needed for related complexes to be made into functional multilayers and multiple future directions for this research is discussed.

1. INTRODUCTION

1.1 Building Efficiency and Sustainability

Climate change is the greatest problem of our time and possibly the greatest problem we have ever faced in all our history. With extreme weather events and record setting heat waves becoming a frequent occurrence the world needs new technologies that not only generate energy from renewable sources (i.e. wind, solar, hydroelectric, etc.) but also reduce our overall energy demand.

Buildings are one such area where an increase in efficiency could pay dividends in terms of sustainability. Buildings account for the majority of energy consumption worldwide.[1] As much as 50% of this energy consumption may be attributed to the HVAC systems used to heat and cool building interiors.[2] A significant portion of this demand is due to the need to keep up with increasing indoor temperatures caused by incident solar radiation which enters a building throughout the day. By decreasing the amount of incident light which can enter a building through the windows and increase its internal temperature great cost savings can be achieved. To achieve this, many have looked to smart windows as a way of modulating incident light and improving energy efficiency. Multiple schemes for smart windows have been proposed and many remain in active development. One category of smart window that has shown a great deal of promise are electrochromics. Trials conducted using the Department of Energy's DOE-2.1E building simulation program have shown that energy usage can be decreased by as much as 20-30% during peak demand times by using electrochromic panels.[3] With such drastic energy savings known to be possible, the development of new building materials is a priority for many in both government and industry.

1.2 The Promise of Electrochromics

Smart windows are based on the well-studied phenomenon known as electrochromism. Electrochromism is a process in which a redox event causes a material to change color, reflectance, or transmittance. Electrochromic panels are already available commercially. Boeing's has utilized tungsten oxide panels in the 787 Dreamliner,[4] luxury car makers like Maclaren have begun to incorporate self-dimming panels into sunroofs, and smartphone maker OnePlus has explored using electrochromic lenses in its smartphones' cameras.[5] These are just a few of the applications that have already been found for electrochromic materials, but the technology is still in its early stages and there continues to be significant research to overcome the limitations of current electrochromic materials.[6]

Energy consumption continues to be a challenge in electrochromic design. As long as a panel is in its darkened "on" state it will consume energy. This is a limitation shared by all current devices, which tend to be built using layers of solid metal oxides or other bulk materials sandwiched between panels of indium tin oxide (ITO) coated glass,[7] and continues to limit the viability of many envisioned applications. The above example of the OnePlus smartphone, for example, was criticized at its unveiling for the added drain it introduced to the device's battery. The example of the car sunroof would similarly drain the vehicles battery if it was left on while the engine was turned off. This is not the only challenge in building electrochromic panels, switching efficiency, coloration efficiency, cycle lifetime, and chemical stability are all critical factors.[8] However, the need for the need for a continuous supply of energy to remain in an "on" state remains a significant drawback of electrochromics that limits their ability to introduce new energy savings in buildings and prevents their employment in certain novel applications.

Figure 1 shows the structure of a traditional electrochromic panel. Sandwiched between two transparent ITO electrodes is a bulk metal oxide electrochromic layer, a gel electrolyte layer, and an ion storage layer.[7,8] Bulk oxides are not the only option for the design of electrochromics and new approaches may help to address many of the limitations of current devices. Molecular systems, both organic and inorganic, represent and area of active research.[9] This subfield of molecular electrochromics offers multiple advantages. Unlike the bulk metal oxides in current devices molecular electrochromics can be endlessly customized through synthetic modification. Besides the obvious benefit that this allows for careful control over the color, these molecular electrochromics function in different chemical environments than metal oxides films. Classes of molecules including, but not limited to, viologens,[10] pyroles,[11,12] perylene diimides,[13,14] and transition metal complexes,[15] have all be investigated for their electrochromic properties for use in these devices.

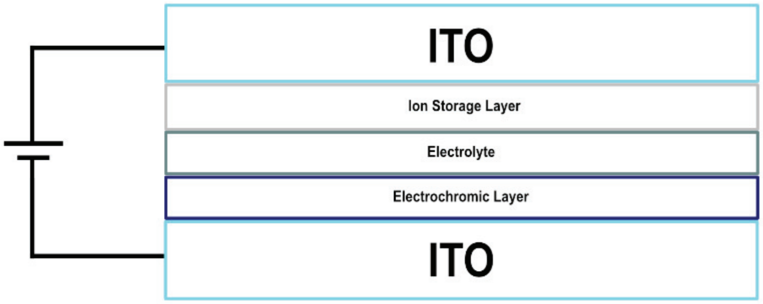

Figure 1: General schematic of an electrochromic device.

1.3 Layer-by-Layer Assembly as A Method For Building Electrochromic Multilayers

Many approaches to layer-by-layer (LbL) assembly can be found in the literature. LbL films are easy to prepare in a laboratory setting and allow for precise control of layer thickness and composition.[16,17] Figure 2 shows a generalized LbL process. In these procedures, the substrate is first prepared with an initial layer linker molecule anchored to the surface. Successive layers are then built up by exposure to alternating solutions of layer and linker molecules until the films reach a desired thickness.[16] Precise control over film thickness is achieved through self-limiting mechanisms for joining these layers and linkers together. These mechanisms include covalent attachments, ionic interactions, hydrogen bonding, or coordinative interactions where metal ions form the layers and ligand assemblies act as the linkers between these layers.[17] Substrates may be dipped, sprayed, or spin coated, and solutions can be altered to control the chemical composition of each layer making a variety of complex architectures possible. LbL films have been used in microelectronics, hydrophobic coatings, nanoparticles, chemical sensors, and solar cells.[18,19]

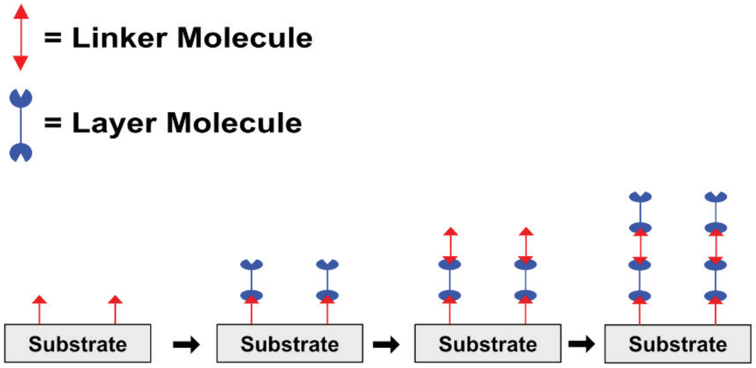

Figure 2: General schematic of a layer-by-layer assembly using alternating layers of analyte held together by linker molecules.

The foundational self-assembled monolayer (SAM) on which multilayers are built can be made from several classes of molecules, three of which are depicted in Figure 3.[20] The quintessential monolayer for LbL techniques is the gold-thiol self-assembled monolayer (SAM) which established the paradigm for SAM research.[21] These SAMs are assembled by submerging freshly cleaned gold substrates in solutions of thiol-functionalized molecules. With sufficient time, thiol head-groups adsorb onto the surface of the gold and Van der Waals forces between alkyl chains lead to the formation highly ordered SAMs.[22] Once deposited these SAMs may be used for a variety of purposes depending on the functional group attached the end of its alkyl tail. This approach is commonly employed in electrochemical studies at gold electrodes where these SAMs may be used to control the behavior of the electrode interface.[23–25] Fundamental studies of the electrochemical properties of alkane-thiols on gold have been performed with ferrocene both attached covalent to the end of these alkyl chains and in solution with the SAM acting as a spacer between the electrode and analyte.[21,26] Cysteines added to the end of the alkyl chains have been used to coordinatively attach porphyrins electrode surfaces.[27] Others have used azide-functionalized alkane-thiols to covalently attach electrophores to the SAM through copper (I)-catalyzed azide-alkyne cycloadditions (CuAAC) "click" reactions.[28]

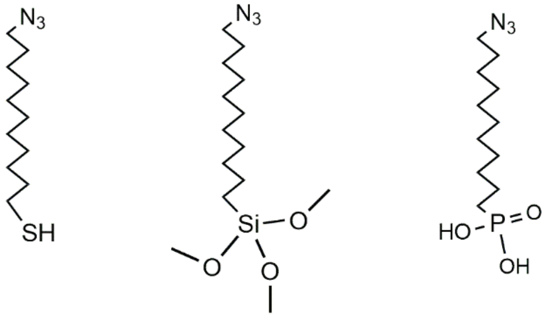

1 **2** **3**

Figure 3: Structures of three molecules suitable for constructing azide-functionalized SAMs including (1) alkyl thiol (2) 11-Azidoundecyltrimethoxysilane (3) phosphonic acid.

This last method, shown in Figure 4, is especially appealing because in principle any molecule containing an appropriate ethynyl group may be covalently attached to this surface forming a 1,2,3-triazole linkage between the molecule and the SAM. If the molecule of interest contains multiple ethynyl groups pointing in opposite directions, then multiple layers may be deposited by using linker layers consisting of azide-functionalized molecules.[29]

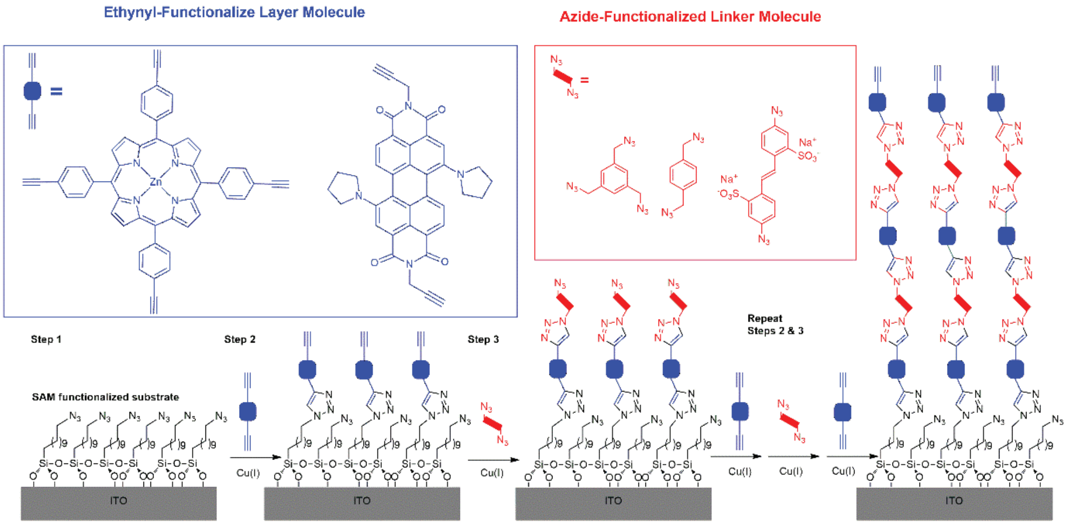

Figure 4: Schematic of the CuAAC LbL used with examples of linker molecules (red) and layer molecules (blue).

These methods offer many opportunities for researchers interested in constructing molecular electrochromics combining the customizability that this molecular approach entails with the precise control of coating structure and thickness conferred by LbL methods. Our group has used silanes extensively in the past to construct multilayers on glass coated with a conducting Indium Tin Oxide (ITO) film using silane anchors to study charge transfer and layer growth behavior in a variety of molecules including porphyrins and perylenediimides.[29–31] This technique required careful preparation of the ITO glass surface followed by submersion in a single-use solution 11-azidoundecyltrimethoxysilane under a nitrogen atmosphere to construct the monolayer. These methods were highly effective but in recent years some challenges have arisen in reliably depositing the initial SAM. Phosphonates offer an alternative to these silane-based SAMs and have several advantages.

Multiple materials may be used as substrates for phosphonate-based SAM. These include various oxides of alumnium, titanium, silicon, and iron, as well as ITO.[32–34] This includes the oxide layers that form naturally on the surfaces of many metals.[35–38] The phosphonate head groups have several modes of interactions with the substrate. These interactions may consist of M-O-P bonds or of coordinative or ionic interactions between the metal oxide surface and the P=O functional group. After submersion in the phosphonate solution SAMs are often annealed to drive the condensation reaction forward and ensure the formation of covalent bonds between the phosphonate and the oxide surface.[39] Phosphonate SAMs on ITO (Figure 5) have several advantages compared to silane SAMs on ITO and thiolate SAMs on gold surfaces. They have greater stability when compared to the thiolate gold SAMs which oxidize readily and are also not transparent. They are more stable in acidic conditions than the corresponding silane-based SAM. And unlike silanes, phosphonate anchors do not undergo self-polymerization reactions that can impede SAM formation.[33,39]

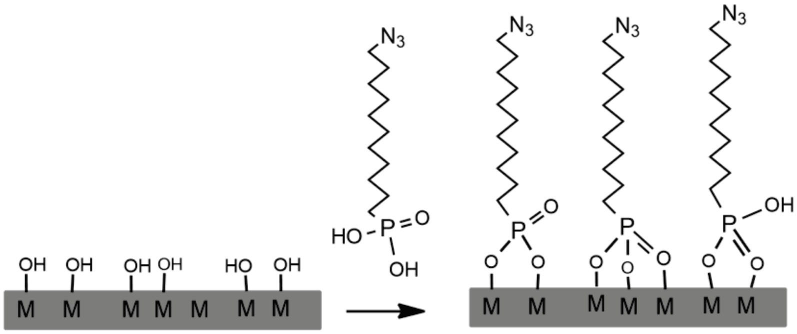

Figure 5: Generic schematic of SAM formation on a metal oxide substrate from 11-Azidoundecylphsophonic acid.

1.4 Spin Crossover as a Mechanism for Energy Efficient Electrochromics

1.4.1 History and Fundamentals of Spin Crossover

Spin-crossover (SCO) phenomena form the foundation of an active field of research spanning more than eight decades all the way back to its discovery in 1931 when it was first reported by Cambi and coworkers.[40] Like many of the interesting properties of transition metal complexes, SCO involves the arrangement and behavior of a metal's d-electrons and the influence of coordinated ligands on their behavior. Changes in temperature, pressure, or incident light are commonly used to induce SCO. When subjected to one or several of these stimuli, a spin crossover compound will undergo a rearrangement of its d-electrons from a low-spin (LS) to high-spin (HS) state or vice versa. The effects of this transition can be seen in changes in metal-ligand bond lengths, spectroscopic properties, and magnetic moment. These drastic changes have inspired a great deal of interest among researchers interested in understanding how to design and control useful SCO materials for use in displays, data storage, and other applications.[41–43]

Despite the difficulty of designing purpose-made SCO materials the underpinnings of the process can be explained simply through ligand field theory. When ligands bind to a metal ion they interact with the metal's d-orbital electrons and in doing so they break the degeneracy of the d-orbitals separating them into the higher energy e_g* orbitals and the lower energy t_{2g} orbitals. The separation between these two sets of orbitals is known as the ligand field splitting energy (Δ_O).[44] Electron occupancy in these orbitals depends on this ligand field splitting energy as well as the electron pairing energy (Π) associated with placing an electron into an orbital in which one electron already resides. If the splitting energy is large relative to pairing energy, electrons will preferentially occupy the low energy t_{2g} orbitals despite the energy penalty incurred by two electrons sharing an orbital. If the splitting energy in small in comparison to the pairing energy, then the d-electrons will instead populate the higher-energy orbitals. These two arrangements are referred to as low-spin and high-spin respectively. This relationship is depicted for a d^6 metal center in Figure 6. Typically, a transition metal complex with four to seven d-electrons is either low-spin or high-spin, but if the field splitting energy is approximately equal to the pairing energy, then SCO may occur.[42,45,46]

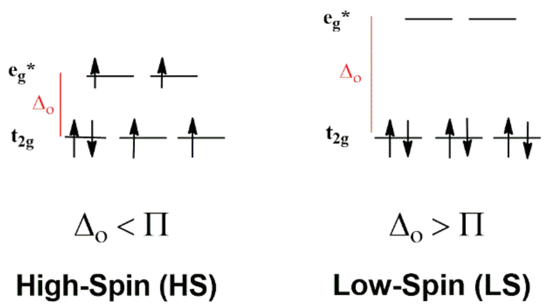

Figure 6: The influence of ligand field splitting energy on the spin state of an octahedral d^6 metal center.

Ligand design is an important factor in the intentional design of SCO materials not solely because of their ligand field effects but for their steric influence as well.[47–49] In the solid phase, intermolecular interactions between ligands of adjacent complexes or blocking interactions caused by intercalated solvent molecules are often responsible the stability of low- and high-spin states.[45,48,50–56] SCO's structural and electronic effects are routinely studied using spectroscopic methods,[48,57–59] but temperature-dependent magnetic susceptibility studies best illustrate one of the primary metrics by which SCO materials are evaluated. If the spin states are bistable the magnetic susceptibility data will show a hysteresis loop (Figure 7) in which the low-spin to high-spin and high-spin to low-spin transitions occur at different temperatures. The separation of these transition temperatures is then used to judge the stability of the two spin states.[60]

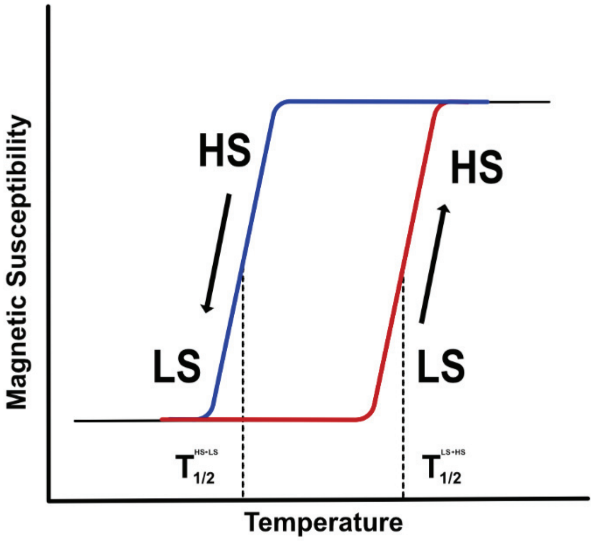

Figure 7: Idealized depiction of a hysteresis loop created from temperature-dependent magnetic susceptibility data.

For an SCO material to be useful its spin transition must be rapid, consistent, and stable. [61] In the binary parlance of computer science low-spin and high-spin states may be thought of as "off" and "on" or alternatively as 0 and 1. Users depending on an SCO-based data storage device would require spin states to change abruptly and remain stable for extended periods. The same concern is shared by other potential SCO applications. A chemical sensor must reliably change states only in the presence of its intended analyte. The same is true for thermochromic paints that could be used to monitor the freshness of frozen and refrigerated products.[62] Display technologies, electrochromics included, require abrupt color changes on demand that do not fade with time. Currently, this bistability is easy to achieve in the solid phase where steric interactions are able to control SCO hysteresis.[48] Because most SCO devices are expected to be used under standard temperature and pressure an abrupt hysteresis with a separation of around 50 K at room temperature is generally considered desirable.[60] Stability of high- and low-spin states, measured by magnetic or spectroscopic methods, can be readily achieved in solids or at low temperatures. Achieving bistability in solution phase molecules, or in molecules located at an interface, remains a challenge. To address these limitations researchers have increasingly turned to uncommon SCO stimuli whose mechanisms make bistable SCO possible outside of the solid phase.

1.4.2 Uncommon Stimuli

Although heat, pressure, and light are the most common stimuli seen to induce SCO behavior in the literature there are many other stimuli that are less often studied and offer opportunities for designing novel molecular devices. These uncommon SCO stimuli are gaining increased attention in the literature as bistable SCO in the solid phase has become common but bistability in solution or at in interface remains rare.[63] Two of these uncommon stimuli include electron transfer, a process known as redox-coupled spin-crossover (RCSCO), and ligand coordination/dissociation, known as coordination induced spin crossover (CISCO).

At first glance RCSCO appears to be little different from a standard redox event in which a complex's metal center either gains or loses an electron. Unlike a typical redox event, which consists of a single charge-transfer step, when RCSCO is involved not only is there a transfer of charge but there is drastic rearrangement of the complex's electronic structure which results in significant chemical changes following oxidation or reduction. In a cyclic voltammogram this appears as an irreversible electrochemical process like the one shown in Figure 8 due to the change in geometry imposed by the spin transition. Theoretically, a reversible redox reaction appears on a cyclic voltammogram with a minimum peak separation of 59 mV,[64] in practice under experimental conditions the peak separation may be as large as 100 mV. Voltammograms with separations significantly larger than this are considered irreversible.[65]

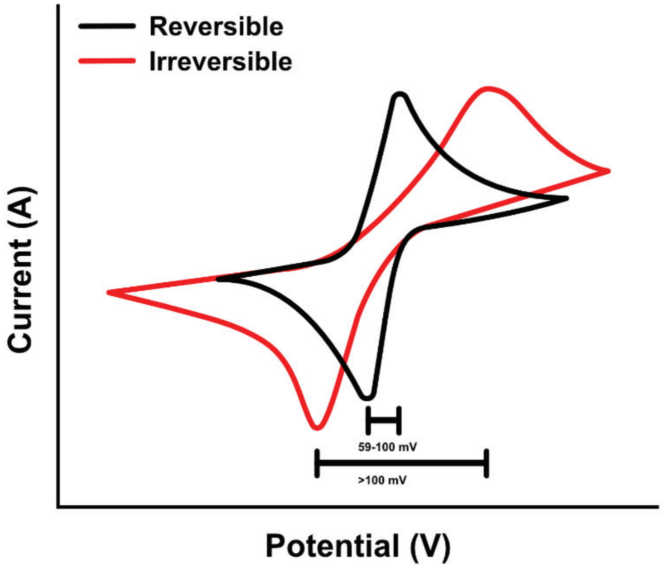

Figure 8: Qualitative depiction of reversible (black) and irreversible (red) cyclic voltammograms.

RCSCO is often depicted using the square scheme shown in Figure 9 in which steps A and C correspond to charge transfer reactions, steps B and D represent the electronic rearrangement that follows the charge transfer reaction as the complex assumes a new, more stable spin state. Steps B and D are described by the spin equilibrium constants $K_{se,2+}$ and $K_{se,3+}$ respectively. These constants represent the process of electronic rearrangement that follows the initial redox event. If $K_{se} << 1$ then the equilibrium will favor a low-spin configuration, if $K_{se} >> 1$ the equilibrium will favor a high-spin configuration. Large differences in $K_{se,2+}$ and $K_{se,3+}$ will result in cyclic voltammogram with large peak separations. [66]

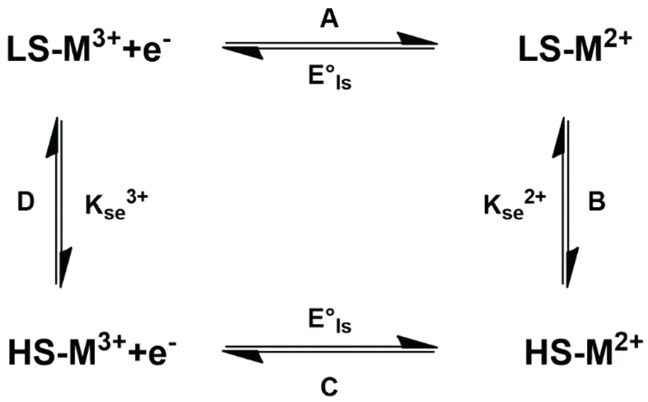

Figure 9: Simplified square scheme depicting a typical RCSCO mechanism adapted from Turner and Schultz.[66]

RCSCO is commonly seen in biological systems. It is an essential part of the catalytic cycle of redox proteins with cytochrome P450 being the classic example of such an enzyme.[67,68] In these environments, RCSCO functions in concert with a series of ligand association and dissociation events which also influence the spin state of metals they are coordinated to.[66] Interplay between RCSCO and ligand-coordination is complex, and, in some instances, it can be argued that the mechanism is primarily CISCO rather than RCSCO and disentangling the two can be a challenge.

CISCO happens as a result of the well-established fact that certain ligand and first-row metal combinations will result in the formation of low-spin or high-spin complexes depending on the strength of the metal-ligand interactions. As a ligand coordinates to the metal center interactions between it and the metal's d-orbitals result in changes to the ligand field which may result in high- or low-spin electronic configurations.[44] This fact is at the core of all SCO research, but instead of relying on perturbations to an existing ligand field as is typical in most SCO, CISCO functions by changing the ligand field environment directly. Simple examples of this may consist of metal complexes of high-spin cobalt(III) or iron(III) metal center that possess an unoccupied axial coordination site. Coordination of suitable ligands, like pyridine or imidazole, that readily coordinate to the metal center induces a change to the ligand field that favors a low-spin conformation. More recently, researchers have begun to synthesize and study systems where this coordination can be regulated through the application of an external stimulus. Many of these systems have been designed using porphyrins that have been covalently modified with axial ligands whose bonding can be controlled through conformational changes induced by incident light or changes in pH. [58,69–71] Other ligand scaffolds suitable for CISCO exist and will be elaborated on in Chapter Two.

An interesting and compelling factor in both RCSCO and CISCO systems is that the bistability that arises in both cases is due to their unique SCO mechanisms. This unique characteristic makes them ideal for use as SCO switches in solution, at interfaces, or in other SCO materials without the temperature requirements that limit other classes of SCO molecules.

1.4.3 Coupled Charge Transfer and Spin Crossover Reactions of Cobalt Coordination Complexes

RCSCO is known to occur in reactions of the $Co^{II/III}$ redox couple. The unique properties of the $Co^{II/III}$ couple have been an area of interest to electrochemists for decades. Some of this interest has been a result of a biological and catalytic significance of certain cobalt complexes including vitamin B12 and its cobaloxime analogues.[72,73] On a more fundamental level, this interest arises from the changes in spin state that are necessitated by the changes in d-electron count between cobalt(II) and cobalt(III) complexes depicted in Figure 10.

This was highlighted during the 1980s by multiple studies and reviews which interrogated the sluggish electron exchange reaction between $Co(NH_3)_6^{3+}$ and $Co(NH_3)_6^{2+}$ in solution. Electron exchange from the high-spin Co^{II} species to the low-spin Co^{III} requires a change in spin states for both metal centers that is not only due to the loss or gain of a single electron but also a change in d-orbital occupancy with an accompanying change in spin multiplicity.

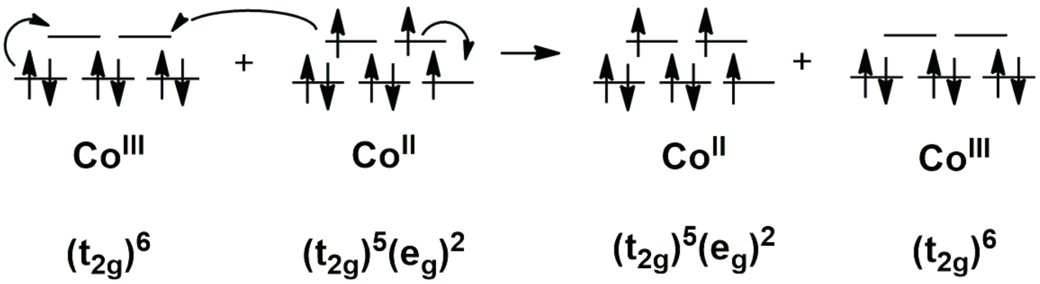

Figure 10: Illustration of SCO in conjunction with electron self-exchange between Co^{II} and Co^{III} complexes in solution with idealized octahedral geometries. Adapted from Geselowitz.[74]

Authors noted early on that the barrier imposed by spin forbidden transitions seemed to be small when compared to the barriers imposed by changes in bond length leading to attempts to reconcile theory and data by finding spin allowed pathways for electron exchange proceeding through various ground and excited state configurations.[74–76] Concurrent studies of similar exchange reactions in complexes of cobalt with various amine cage ligands sought to probe outer-sphere mechanisms and the impact on exchange rates caused by the addition of functional groups to the ligand cages.[77] A later study of the redox behavior of similar caged compounds at an electrode led the authors to conclude that the sluggishness of these Co$^{II/III}$ electron transfers are not due to spin-forbidden properties of the transition, but to the frequent changes in geometry that occur in more flexible complexes.[78] This lively debate exemplifies the numerous factors involved in RCSCO reactions, each of which offers a possible "handle" for the modulation of RCSCO behavior to meet desired operating parameters.

1.4.4 Leveraging Uncommon Stimuli for Novel Electrochromics

Traditional SCO materials that exhibit hysteretic behavior in bulk solids might be suitable for use in traditional electrochromics, but their mechanisms require specific temperature regimes and stimuli that are difficult to provide in household and commercial settings where electrochromic panels might find use. Even if bulk SCO materials were to be incorporated into an electrochromic panel the dependence on solid-phase interactions to achieve bistability ignores the many advantages offered by molecular electrochromics. Developing molecular SCO systems with novel mechanisms based on bistable RCSCO reactions will enable us to design new energy efficient electrochromics with the synthetic tunability offered by molecular electrochromics.

Electrochemical reactions of the $\mathrm{Co}^{\mathrm{II/III}}$ redox couple are known to be both sluggish and dependent on ligand structure. Thus, the RCSCO energy barrier could provide the bistability needed for effective electrochromics. This energy barrier could then be modulated through careful ligand design and CISCO interactions.

Once promising molecular systems are identified through solution studies, ligand modifications can be made to allow for LbL assembly using well-established copper-catalyzed click techniques to build multilayers on ITO electrodes. These electrodes may serve as a basis for proof-of-concept multilayers demonstrating novel RCSCO electrochromics. Once made these multilayers can be evaluated by submersion in electrolyte for spectroelectrochemical studies. The electrochemical peak splitting should be proportional to the lifetimes of the “on” and “off” states. This could be examined by first applying a potential to the multilayer and once the color changes caused by spin-crossover were observed that potential would be removed. If these are truly bistable systems, no change in absorbance will be observed until an appropriate potential is applied to drive the equilibrium in the other direction.

These new bistable electrochromic complexes would make conventional smart windows more energy efficient by removing their passive energy needs and thereby realizing additional energy savings. This technology would make novel applications for electrochromics viable for the first time. Wearable electrochromics have been tried in the past and been abandoned.[9] The examples of electrochromics used in smart phones and car sunroofs are impressive but they are inherently limited by their energy needs. Every addition of an electrochromic panel to a device not connected to a wider power grid merely increases the already growing demand on limited battery capacities. Bistable electrochromics based on molecular RCSCO materials could remove these obstacles and allow for more widespread use .

1.5 Thesis Outline

Chapter 2 will include the contents of a review paper on the topic of coordination-induced spin crossover (CISCO). This is a rarely studied phenomenon in the area of SCO research which offers numerous possibilities for achieving bistability in solution and at solid-solution interfaces. CISCO is essential to regulating the redox behavior of Cytochrome P450 and other heme-based redox enzymes. This behavior is often referenced in the SCO literature even when the specific SCO mechanisms have little to do with the CISCO functionalities in these enzymes. This review aims to fill a gap in the literature highlighting the innovative work taking place in this sub-field of SCO research within the past two decades. Many examples of functional molecules with promising switchable CISCO have been published in the last two decades but there has not yet been an effort to review the progress of this field and provide a "jumping off point" for scholars interested in exploring this field further.

Chapter 3 will cover the ligand-dependent redox-coupled spin crossover behavior of a five-coordinate cobalt salen which was originally synthesized and studied by previous students in our lab Drs James Buchwald and Subadeep Kal. The high-spin to low-spin switch they observed following coordination of an exogenous ligand and the accompanying changes in electrochemistry were further studied with a series of Lewis basic heterocycles and a handful of anions. The peak splitting seen in cyclic voltammograms of this complex in the presence of exogenous ligands is correlated to the structural properties and basicities of the ligand and important parameters for intuiting the degree of peak splitting are identified. This work constitutes a first step to the design of tunable redox switches using this and similar complexes.

Chapter 4 will discuss the synthesis and characterization of two cobalt(II) β-diketonate complexes that exhibit redox-coupled spin crossover behavior in solution. These complexes are based on similar complexes first reported by Harding in 2012.[79] The key differences between Harding's work and the work presented here are that the complexes highlighted have been synthetically modified with ethynyl functional groups with the goal of constructing electrochromic multilayers on ITO glass substrates. Efforts to assemble these multilayers were unsuccessful and the chapter concludes with several hypotheses for why this was the case and describes several paths forward involving the synthesis of new related complexes which may be more suitable for multilayer assembly.

2. A REVIEW OF COORDINATION-INDUCED SPIN CROSSOVER IN NATURE AND ON THE BENCHTOP

Coordination-induced spin-crossover (CISCO) is a common feature of naturally occurring enzymatic systems. Nature has used this process in thousands of cytochrome enzymes to metabolize foreign compounds, transfer electrons, catalyze redox reactions, and synthesize biological signaling molecules. Cytochrome enzymes in particular are often cited as examples of naturally occurring spin-crossover (SCO). However, while many entries in the literature cite these natural examples of SC[1]O few go on to describe synthetic coordination compounds with clear parallels to these natural systems. Many natural systems exhibit SCO transitions linked to the coordination of some guest species or through interactions with a redox mediator. Often these SCO processes are complex and are merely a small segment of a much larger catalytic cycle. Synthetic systems which mimic these behaviors offer opportunities to examine the influence of ligand environment, structure-function relationships, active site surroundings, and solution conditions on SCO behavior in detail. This review seeks to summarize notable examples of ligand-dependent spin-crossover and highlight areas where more attention should be focused.

2.1 Introduction

2.1.1 Spin Crossover

Spin crossover is one of the most interesting and frequently studied phenomena in coordination chemistry. At first glance it seems like a simple concept; through the application of an external stimulus, the electronic structure of a complex is changed, resulting in a change in spin multiplicity as low-spin (LS) configurations are converted into high-spin (HS)

Portions of this chapter are in preparation as: McCabe, C. A.; Mitchell, A. L.; Dinolfo, P. H. Coordination-Induced Spin Crossover in Nature and on the Benchtop.

configurations and vice versa.[80] This apparent simplicity obscures the depth and breadth of spin crossover research and its implications for future devices. Any change in the electronic structure of a transition metal complex has drastic effects on its properties including color, magnetic susceptibility, and bond length.[41,61,81] Thus, the ability to readily change the spin state of a coordination complex at will offers researchers an unparalleled ability to tune molecular properties towards desired functionalities.

In the available literature, spin crossover behavior is most frequently seen in complexes of iron, cobalt, and manganese but has been observed in other transition metals as well.[80,82] Reliable methods for the targeted design of SCO materials remains an active area of research. With that said, a great deal has been learned about SCO and there are two factors of universal importance in SCO material design.

1. The metal center must have a d-electron count between d^4 and d^7, so that there will always be partially or fully unoccupied orbitals ready to accommodate alternate electronic configurations.[46,83]

2. The ligand field splitting energy (Δ_O) must be comparable to the electron pairing energy (Π).[46] For this reason, ligands which coordinate through nitrogen atoms are common, but mixed coordination spheres of nitrogen and oxygen have also been documented.[43,84]

When subjected to an external stimulus such as heat, light, or pressure, the similar pairing and splitting energies allow the complex to adopt a lower energy state by transitioning from a low-spin to a high-spin state or vice versa (Figure 11).

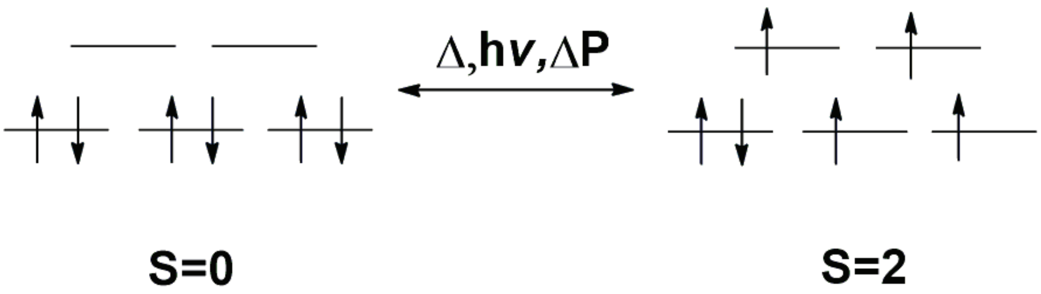

Figure 11: Schematic illustration of d-electron configurations for a low-spin to high-spin transition in an octahedral d^6 metal center.

Since this transition is often accompanied by changes in color, magnetic moment, and bond length, the change in spin state is easily detectable. These properties make spin crossover materials appealing for use in sensors, displays, computer storage, and other spintronic devices.[43,61,85–87] Also of interest to researchers is the presence of spin crossover centers in naturally occurring systems including the many cytochrome enzymes found throughout the natural world.[88,89]

While cytochrome is commonly cited as an example of naturally occurring SCO, there are comparatively few examples of synthetic systems displaying coordination-induced spin crossover (CISCO) like that which is displayed by these enzymes. Although many examples of supramolecular crystal lattices exist where control of the SCO process is linked to interactions between the lattice and solvent molecules have been reported on extensively in Hoffman frameworks, [50,54,55,90,91] instances where spin crossover is induced by coordination of a guest ligand are less well studied. Instead, the majority of spin crossover research seems focused on achieving thermal SCO with a $T_{1/2}$ at or near room temperature.[60]

Spin crossover may be detected using many common instrumental techniques.[60] One of the most popular methods for evaluating SCO behavior in solids is temperature-dependent magnetic susceptibility experiments often performed using a SQUID and the data is displayed as a hysteresis curve similar to the one shown in Figure 12.

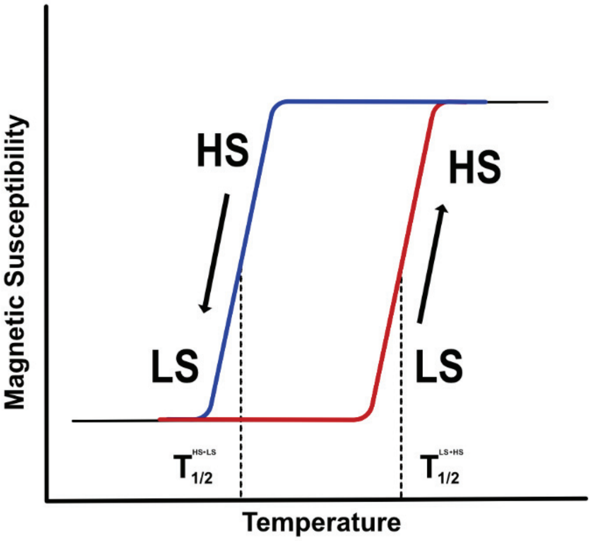

Figure 12: Depiction of a thermal hysteresis curve.

These thermal experiments tend to be less useful in studying the CISCO systems covered in this review. They do, however, provide an excellent illustration of one of the key metrics in SCO research, hysteresis. Nearly all envisioned applications for SCO materials require bistable spin-states. In a data storage device for example, the user needs to know with a high degree of confidence that a bit that has been set to a 1 or a 0 will still be in that state when it comes time to reference the stored data. There is a similar requirement for sensors where a high degree of contrast is required and also for displays which may be expected to maintain a current state for extended periods of time.[61] For this reason, in an ideal SCO system the energy barrier must be high enough to limit interconversion at room temperature. In magnetic susceptibility studies this is seen visually as a hysteresis loop.[60] These hysteresis loops are most common in bulk materials where interactions between molecules in the crystal lattice introduce cooperative effects the result in bistable hysteretic transitions, these same considerations are often not present for molecules in solution.[92,93] This is a significant limiting factor in SCO systems which limits their potential applications to bulk materials that makes applications of solution phase SCO in sensors and sensitizers out of reach of most current materials.

2.1.2 Coordination-Induced Spin Crossover

Coordination-induced spin crossover (CISCO), depicted in a generalized scheme in Figure 13, offers a unique path to SCO bistability in solution or at an interface. Instead of introducing modifications to ligands while attempting to maintain the careful balance between Δ_O and Π a CISCO approach does away with this limitation and manipulates spin state by changing the coordination environment entirely.[63] This approach opens up an entirely new synthetic toolbox for control of SCO behavior. Peripheral ligand structural elements still matter here but in subtly different ways. Ligand modifications are made with the goal of tuning the acidity of the metal center or the basicity of the ligand or restricting the type of ligand that is able to access the metal in emulation of protein active sites. That is not to say that cooperative effects are irrelevant in CISCO. There have been examples of CISCO interactions on metal and metal oxide surfaces,[94,95] and it is easy to envision CISCO active moieties incorporated into polymers and other bulk materials where cooperative effects would likely have a pronounced effect. Ligand lability is a primary consideration in most CISCO research and the methods used to study CISCO reflect this. To best characterize these interactions, CISCO is often quantified through equilibrium constants describing ligand association or through determination of the change in Gibbs Free Energy and the underlying thermodynamic terms involved.[58,96] These may be studied through spectroscopic techniques but may also be studied through electrochemical experiments. Redox changes accompanying CISCO, detected through direct electrochemistry, are useful indicators of CISCO often observed in the study of enzymes and are applicable to synthetic systems as well.[97]

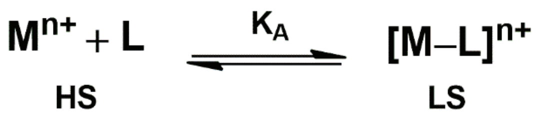

Figure 13: Generalized CISCO interaction.

In this area CISCO overlaps significantly with another subset of SCO known as Redox-Coupled Spin Crossover (RCSCO) that ties CISCO together with the redox-cycles of cytochrome proteins. Here, instead of light or heat, charge transfer is the stimulus which precipitates a spin-transition. The reorganization energies involved here are not just those involved with a simple electron transfer, but also those energy costs associated with the drastic electronic rearrangements that result in a new spin state being achieved. These considerations impose significant energy barriers that are seen in a cyclic voltammogram as a large splitting between the oxidation and reduction peaks (Figure 14), something which is irreversible electrochemically speaking and is indicative of RCSCO. Such interactions are complicated and often depicted conceptually as a square scheme diagram (Figure 15). [66]

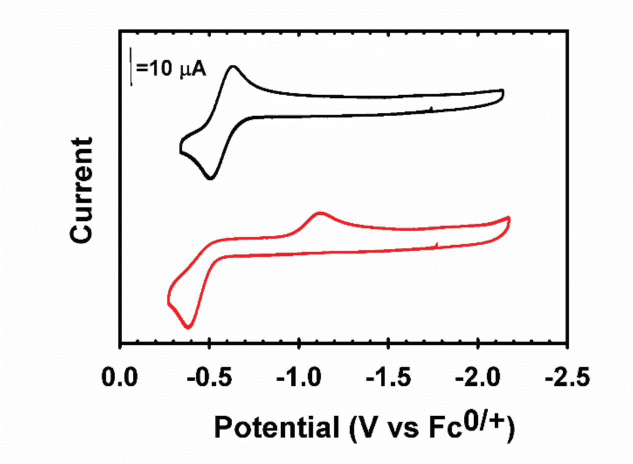

Figure 14: Electrochemistry of a five-coordinate Co^{III} Salen alone in solution (black) and in the presence of 10 eq. of imidazole (red). The peak splitting is the result of RCSCO phenomena coupled to ligand coordination to the metal center. Scans were taken at 500 mV/s in dichloromethane with 0.1M tetrabutylammonium hexafluorophosphate.

It should be noted that not all RCSCO is also CISCO but the two together have the potential to enable novel functionalities that would not be possible otherwise. An example of this is the Co^{II} ion. The odd number of d-electrons means that even in a low-spin arrangement there will still be an unpaired electron leading to an overall spin multiplicity of S=1/2. Because of this a cobalt(II)-based CISCO system, and cobalt(II) SCO systems in general, will be limited in usefulness unless a change in the number of electrons is achieved.[41] Redox reactions offer an easy way to achieve this, coupling this RCSCO to ligand binding allows an easy way to switch between HS Co^{II} and LS Co^{III}. Oxidation of a high-spin Co^{II} metal will yield a high-spin d^6 Co^{III} that will favor a low-spin configuration if a sixth exogenous ligand is available for binding following oxidation.[44,98] Thus, RCSCO coupled to CISCO offers an avenue to achieve new functionalities that are not possible with more conventional SCO mechanisms.

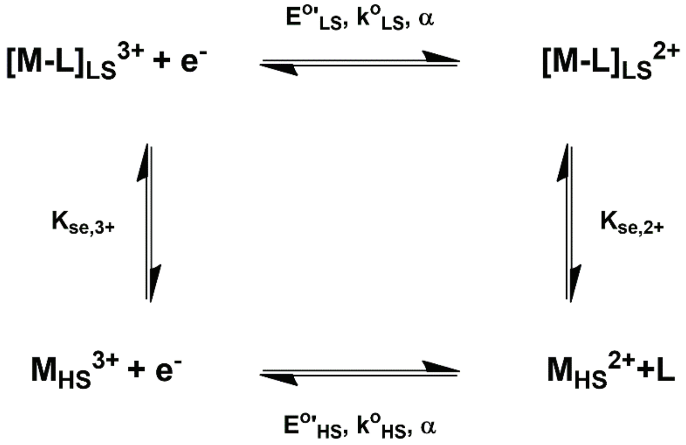

Figure 15: Redox square depicting the interplay between electrochemical and spin exchange parameters in RCSCO reactions coupled to ligand association and disassociation. Adapted in part from Turner and Schultz.[66]

A redox square clearly illustrates how RCSCO depends not only on potential (E), the electron transfer rate constant (k), and the electron transfer coefficient (α), but also on the spin-exchange constant (K_{se}) which accounts for the d-electron structural rearrangements that result in a new spin state. Large differences between the two spin exchange constants $K_{se,2+}$ and $K_{se,3+}$ increased the separation of the anodic and cathodic redox potentials. Changes to the coordination environment achieved through exogenous ligands can therefore affect redox potentials by altering these spin equilibriums.[66] This behavior is seen in the prototypical CISCO system cytochrome P450,[99] and has been mirrored in synthetic complexes. Much information can be derived from electrochemical experiments, but this data is also of value because it may indicate the presence of CISCO in the literature where SCO was not the main focus of the work being done but where the resulting electrochemical data may indicate that more attention is warranted from a CISCO perspective.

Aside from a recent review by Khusniyarov which highlighted several categories of non-thermal SCO,[63] CISCO has received little attention in the literature compared to more conventional varieties of spin crossover. Most of the literature seems concerned with either thermal or light-induced spin crossover. Our review is concerned with a particular subcategory of non-thermal SCO in which complexes undergo SCO in response to change in metal coordination environment. This approach is a departure from "classical" SCO. Instead of being limited to metal coordination with the right coordination environment for spin exchange to occur, CISCO instead works by changing this environment entirely. We begin our survey of CISCO with a brief look at biological CISCO in Cytochrome P450 and Cytochrome c. While our focus here is primarily on artificial systems these biological systems are worthy of discussion. Many in-depth studies and reviews of these enzymes have been published and as a result there is no shortage of data available to inform the rational design of synthetic CISCO systems.[67,68,88,100–107] For the most part, the examples of artificial CISCO that we cover in this review concerns porphyrin complexes of iron or nickel. This is unsurprising, as porphyrins have many similarities to the heme active sites found in cytochrome enzymes and are synthetically versatile.[108,109] This provides several straightforward pathways to the design of intricate CISCO active molecules which we have highlighted in this review. Salens are another class of molecule we discuss in this review which show promise in this field but have received less attention than porphyrins. Additionally, there are other examples of CISCO in the literature that have yet to garner more attention. We have made attempts to identify these molecules and highlight them here as avenues to designing useful molecules that warrant further study. To that end, our primary focus is examples of coordination complexes where authors have demonstrated that the spin state of the metal center can be controlled through reversible ligand binding and have shown that this binding may regulated through an external stimulus. These examples are rare compared to studies which show a given complex may have a different spin state after titration with an exogenous ligand. The later examples are important in identifying potentially useful molecules but do not go as far as to investigate ways by which binding can be manipulated to achieve a desired spin state on demand. Wherever possible we have chosen to focus on those more mature examples of CISCO which show potential for the design of molecular machines, sensors, and catalysts. However, the context provided by those earlier titration studies is still valuable and where appropriate we have included these for the purpose of providing historical context and identifying systems which deserve more attention.

The most obvious application for these materials is as sensors. This near-term application is not the only reason to be interested in CISCO in the long term. In biology, CISCO interactions serve as on/off switches in catalytic cycles and electron transport chains.[110] Similar uses for artificial CISCO systems might be found in the future to form electron transport chains in molecular machines or as a mechanism for locking electrochromics into a given coloration state.

2.2 Spin Crossover in Biochemical Systems

CISCO is commonly seen in biological systems. Prominent examples include the many and varied cytochrome enzymes in which spin modulation of an Fe atom within a heme prosthetic group play important roles in regulating redox cycles.[88,101] While this review is concerned primarily with synthetic examples of CISCO, a brief introduction to a pair of interesting natural systems is included here to illustrate the importance of this process in biochemical systems.[110] In these examples a few of the many variables involved in axial ligand coordination are highlighted. The significance of these interactions in the biological roles these systems play alone makes this a topic worthy of study. But better understanding of this behavior may benefit synthetic research endeavors as well. Cytochromes are valuable reference system in which the many variables relevant to CISCO including ligand characteristics,[111] and active site environment,[112,113] have already been studied in great detail.

2.2.1 CISCO Interactions in Cytochrome P450cam

One of the most prominent cytochrome enzymes is cytochrome P450. Cytochrome P450 is a large superfamily of monooxygenases named for the strong absorbance of their carbon monoxide bound adducts at 450 nm. These enzymes are found in many organisms where they serve in two broad functional roles; synthesizing signaling molecules, and metabolizing potential toxins by oxidizing them to water-soluble derivatives ready for excretion.[103] More specifically, these reactions include the metabolization of nicotine, the conversion of catechol to muconic acid via cleavage of a benzene ring with dioxygen, synthesis of steroid hormones, and the conversion of polyunsaturated fatty acids into biologically useful molecules.[103,114] There are many excellent reviews and studies of this large family of enzymes and they will not be covered in depth here. Instead, we will briefly describe the role of spin crossover in P450cam, a well-studied example of a cytochrome P450 enzyme obtained from the bacteria Pseudomonas putida. P450cam was the first member of the P450 superfamily for which a structure was determined and has been used as a model enzyme in many studies since. P450cam is primarily involved in the hydroxylation of camphor to 5-exo-hydroxycamphor at biological temperature and pH, a reaction that would otherwise require much harsher conditions.[115]

A single heme group resides within the active site of P450cam (Figure 16). Of the two axial coordination sites available on the metal center, one is occupied by a single cysteine residue, while the active side is occupied by a single water molecule. This bound water serves an important function in regulating the activity of P450cam. Without it, the Fe^{III} center would be continually reduced by the P450cam's redox partner leading to the spontaneous formation of potent oxidizing agents. In the resting state, this water molecule remains coordinated to the iron center and serves to maintain a low-spin (S=1/2) resting state in the Fe^{III} metal center. Substrate binding is aided by hydrogen-bonding interactions between a number of amino acid residues present in the active site and the camphor substrate. As camphor approaches the active site it displaces the axial water molecule. This water molecule functions as an on/off switch for the enzyme. When bound the water molecule enforces a low-spin state (S=1/2) ensuring that the d_{x2-y2} and d_{z2} orbitals of the Fe^{III} center are too high in energy to accept an electron from P450cam's redox partner putidaredoxin. Displacement of this water by the approaching camphor substrate removes its influence on the ligand field of the heme iron, lowering the energy of the $d_{x^2-y^2}$ and d_{z^2} orbitals, and allowing the metal to assume a high-spin state (S=5/2). In this state, the reduction potential of the bound Fe^{III} changes considerably resulting in a positive shift in the reduction potential of the iron center from -300 mV to -170 mV. The high energy $d_{x^2-y^2}$ and d_{z^2} orbitals are now within the reach of P450cam's redox partner and at this point, a one-electron reduction takes place following an electron transfer from putidaredoxin and the catalytic cycle continues.[110]

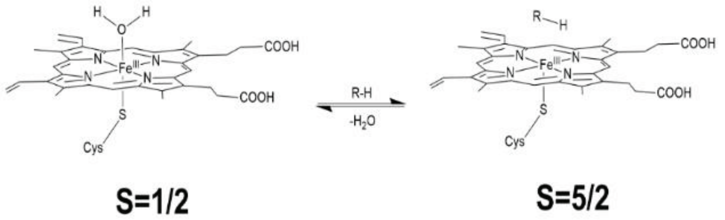

Figure 16: Schematic of the low-spin to high-spin transition induced in cytochrome P450 the displacement of an axially coordinated water molecule caused by an approaching substrate. Structures adapted from Harris et al.[110]

Similar interactions have also been observed with related compounds with these studies exemplifying importance of steric interactions especially in the highly structured and specific bind pockets found in enzyme active sites. In this case, substrates that are too small to fit adequately in the active site do not come close enough to the Fe^{III} center to displace the bound water, meaning the enzyme remains in its "off" state and consequently no reactions are observed. This was shown in Raag's X-ray studies of three different substrates and their interactions with P450cam. Camphor, the protein's normal substrate, approached closely enough to the metal center to displace the bound water and induce a low-spin to high-spin transition. A larger adamantanone was shown to do the same. The smaller norcamphor however failed to induce this transition as it was too small to adequately fit into the binding pocket and displace the bound water.[113]

The above example is an interesting one that takes advantage of cytochrome P450cam's typical mechanism which controls spin state by displacing the coordinated ligand rather than introducing an entirely new ligand. Other research has looked at more explicit coordination of Lewis bases to P450cam's central heme. Mohamed and coworkers have reported the binding of a series of pyridine- and imidazole-derived ligands to P450cam and have detected numerous possible binding modes via UV-vis spectroscopy, since depending on steric factors even an N-donor does not displace the bound water and may instead hydrogen bond to the water protons instead. [116] As a demonstration of the importance of the iron spin state to P450cam's catalytic cycle, they noted that ligand binding inhibited the enzyme's catalytic cycle and favored the low-spin Fe^{III} state. Presumably this is because the N-donors used here are stronger Lewis bases than water and thus bind more tightly to the Fe^{III} center. This bond was evidently strong enough to resist displacement by the enzyme's normal substrate. Especially interesting was that reduction of the low-spin Fe^{III} center to Fe^{II} broke the Fe-N bond to give a high-spin Fe^{II}.[117] These strong N-donor ligands are much stronger bases than water alone, their binding to the metal center would result in a much larger reduction potential of the low-spin Fe^{III} as a result of the larger field splitting energy keeping the $d_{x^2-y^2}$ and d_{z^2} orbitals even further out of reach of P450cam's typical redox partners. The breaking of the Fe-N bond upon reduction is an excellent demonstration of the utility of coupled RCSCO and CISCO interactions where a redox event can be used to control ligand binding and ligand binding can be used to control redox potentials. These experiments provide examples of steric influences on ligand coordination and on the usefulness of a metal center's oxidation state for regulating ligand binding that could be of use in synthetic redox-coupled CISCO.

2.2.2 CISCO in Cytochrome c

Another cytochrome which appears frequently in the literature is cytochrome c. Cytochrome c is a class of small, thermodynamically stable electron transfer proteins found in in both eukaryotes and bacteria and has been widely studied thanks to its ease of purification. Cytochrome c's active site is depicted in Figure 17 and incorporates a c-type heme through a pair of thioether bonds formed with cysteine residues, a histidine axial ligand, and a second axial ligand situated at the end of a peptide loop that is normally, but not always, methionine.[102]

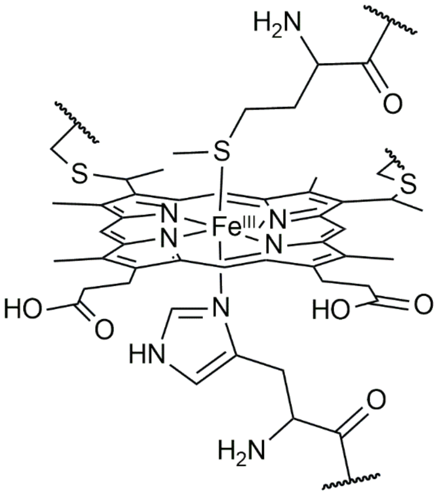

Figure 17: The heme group found at the center of Cytochrome c. Adapted from Bertini et al.[102]

Cytochrome c is not typically known for acting on substrates in same manner as P450cam, instead it serves as an important intermediary in the mitochondrial electron transport chain leading to the synthesis of ATP and acts as a signaling protein in apoptosis.[118] This has inspired a great deal of research into the effects of ligation of the central heme in an effort to understand how the coordination environment around the heme group influences the behavior of these charge transfer proteins. For example, instead of methionine as is typical, the axial coordination site of the heme may instead be occupied by other amino acid residues, hydroxide ions, or a water molecule. Distortions to the peptide loop holding the methionine residue in place have been reported upon changes in pH with evidence to suggest that these changes result in a high-spin iron center. [107] Multiple spin states for the heme of cytochrome c have been observed including a low-spin S=1/2 in the presence of a strong field ligand, an intermediate S=3/2 state when bound to a single intermediate strength ligand or two weak ligands, and a five-coordinate high-spin S=5/2 state in which one coordination site remains unoccupied. [88]

Direct electrochemistry of mutant and wild type cytochrome c proteins by Ye et al indicated several of these changes. In these experiments the quasi-reversible redox wave for the

$Fe^{II/III}$ redox couple was shown to shift based on environmental conditions and is dependent on the structure of the peptide loop containing the axial ligand. Conformational changes to this axial loop caused by changes in hydrogen bonding as a result of pH or because of residue substitution that resulted in positive half-potential shifts.[112]

Other research has focused on the introduction of exogenous binding ligands rather than differences in protein structure have been shown to induce even more dramatic shifts. Shifts in potential have been observed in Fe^{III}/Fe^{II} redox couple in direct electrochemical experiments where the reduction potential of unbound cytochrome c was reported to be +263 mV vs SHE. In the presence of ligands meant to displace the axially coordinated methionine residue new more negative reduction potentials of the low-spin Fe^{III} adduct were measured for ammonia (-127 mV), azide (-145 mV), imidazole (-135 mV), and 2-methyl-imidazole (-135 mV) with shifts as large as 408 mV in the negative direction induced by azide.[111] The example of these four ligands gives us a look at important factors in the binding behavior of the three ligands if we assume the magnitude of the cathodic potential shift corresponds to the influence of the ligand on the magnitude of the $K_{se,3+}$ term. While the difference provided by a single methyl group appears to be small based on the minor differences in the reduction potential their much higher basicity compared to ammonia clearly induced a great field splitting owning to the fact that they act as stronger sigma-bond donors. This is confirmed by a reference of the respective gas phase basicity of each ligand. Ammonia has a basicity of just 819.0 kJ/mol while imidazole and 2-methyl-imidazole have basicities of 909.2 kJ/mol and 929.6 kJ/mol respectively. Azide would at first seem to defy this trend with a value of just 723.5 kJ/mol reported for hydrogen azide.[119] The much larger shift in reduction potential can instead be explained by the negative charge on the anion that is not present in the other three bases which would increase its affinity for the positively charged metal center and increase the electron density around the metal leading to a higher reduction potential.

2.3 CISCO in Synthetic Systems

While artificial systems inspired by the binding properties of cytochrome are rare compared to systems in which SCO is induced by heat, pressure, or light, there are a handful of interesting examples in the field. Besides potential applications as sensors and data storage devices alongside other spin crossover compounds, these examples may be of interest to researchers seeking to develop new catalytic complexes. Enzyme mimics incorporating host-guest interactions and transition metal centers are vibrant areas of research that can draw greatly on the examples presented by natural systems.[120–122] Control over these interactions is also worth considering. Many examples couple ligand binding to some other stimulus, such as light,[123,124] pH, or electrochemical potential.[125]

2.3.1 Metallo Porphyrins

It is perhaps most appropriate to begin our discussion of synthetic CISCO systems with those that most closely imitate those found in nature. Porphyrins, depicted in Figure 18 are aromatic tetradentate heterocyles composed of four pyrole moieties joined together by methine bridges.[108,109] When coordinated to a metal center this results in a four-coordinate square planar geometry with axial sites available to coordinated additional ligands which influence the spin states and redox properties of the metal center. The methine bridges are often modified synthetically to create meso-substituted porphyrins, as are the carbons of the pyrrole rings to create β-substituted porphyrins. These modifications may be done to introduce electron-withdrawing or electron-donating groups, improve solubility, or mimic binding pockets.[126–128]

The central importance of the heme group to a number of biological functions has created a vibrant research community across decades with objectives ranging from studies of porphyrins as heme analogues,[69,129] to synthetically modified porphyrins optimized to serve as molecular catalysts in reactions of industrial importance,[130,131] and as chemical sensors in variety of contexts.[132] Synthetic modifications have shown that electron withdrawing substituents increase the Lewis acidity of the metal center with respect to Lewis bases,[133] making porphyrins an ideal platform for the design and testing of tunable CISCO systems of biological relevance.

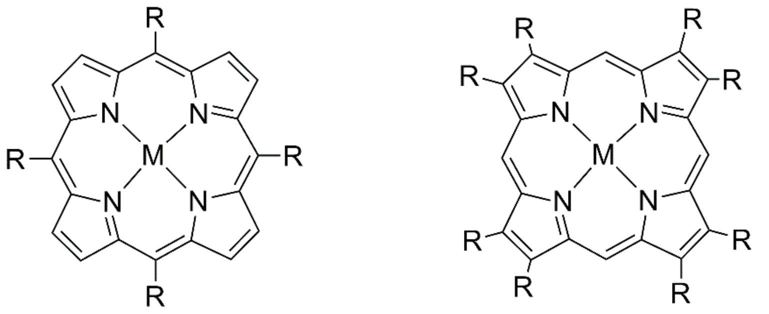

1 **2**

Figure 18: Generic structures of meso-substituted porphyrin (1) and β-substituted porphyrin (2).

There are three broad categories of porphyrin which we have chosen to focus on for nickel- and iron-containing porphyrins which are the most common examples of CISCO in the current literature. There are also a handful of cobalt-containing porphyrins which we have highlighted in less detail owing to fewer available references. Porphyrins described in this section fall into one of three categories.

1. Binding of diatomic ligands such as cyanide and hydroxide anions as well as diatomic oxygen.
2. Binding of nitrogen-containing heterocycles which can themselves be synthetically modified to modulate binding behavior.

3. Binding of any of the above ligands to porphyrins modified with functional groups to control the binding of ligands through bulky groups on the ring which limit the approach of exogenous ligands or incorporate such ligands into the porphyrin itself.

Synthetically modified porphyrins include strapped porphyrins in which a multi-carbon chain is covalently attached to the porphyrin ring on either side of the metal center to allow only ligands of sufficiently small size to reach the metal.[134] Another example are "hangman" porphyrins which are popular in biomimetic catalysis research. Here, a functional group is synthetically attached to the porphyrin ring so that it is held above the metal center where it can hold a substrate in place through hydrogen bonding interactions.[135,136] Also of interest are "picket fence" porphyrins which do not explicitly block the coordination site but do introduce bulky functional groups that help to create hydrophobic pockets analogous to enzyme active sites.[69] Some examples of picket fence porphyrins incorporate axial ligands into the framework as well.[137] All these motifs have found a place in CISCO research, further bridging the gap between natural enzyme systems and the synthetic CISCO systems currently under development.

2.3.1.1 Iron Porphyrins

The first category of porphyrins we will examine are those that have the most similarities with the hemoproteins we have already explored in Cytochrome P450 and Cytochrome c and for which many examples in the literature exist that are not explicitly focused on CISCO but contain useful information for synthetic chemists. Early examples of CISCO in iron porphyrins were, like other examples of CISCO as we will see, largely restricted to characterization of bound and unbound adducts without much focus on reversible ligand-binding which might lead to the development of molecular switches.

Coordination of diatomic molecules to heme active sites is found throughout biological systems to facilitate oxygen transport and molecular signaling.[138] Spin state is highly relevant to these mechanisms.[89] This prominence is mirrored in synthetic systems studied by researchers in search of molecular analogues capable of elucidating the complex mechanisms of hemoproteins. Reversible binding of NO has been an intense focus of research for decades owing to its biological significance as a signaling molecule. Hemeproteins have exhibited multiple reactions with NO which has been shown to have a role in various signaling processes and has been implicated in iron-centered catalytic cycles together with H_2S resulting in the synthesis of sulfide and nitrosyl species thought to be important to cascade signaling processes.[139,140] An early example of this research was carried out by Wayland and Olson in 1973 who explored the pressure-dependent binding of NO to Fe^{III} Tetraphenyporphyrin ($[Fe^{III}TPP]Cl$) both in a solution of toluene and as a frozen glass. The high-spin (S=5/2) state remained constant at both 293 K and 77 K indicating that no temperature-dependent SCO occurs in the unbound $[Fe^{III}TPP]Cl$. Only when exposed to gaseous NO did $[Fe^{III}TPP]Cl$ convert to a low-spin (S=1/2) state. Furthermore, this transition was shown to be reversible on a relatively long timescale by removing the gaseous NO allowing $[Fe^{III}TPP]Cl$ to release the bound NO gas and return to its initial high-spin state over the span of one hour.[141] More recent studies of water-soluble Fe^{III} porphyrins have also displayed reversible binding to NO accompanied by a change in spin-state.[142] Photoinduced dissociation of NO has also been reported.[139]

Whereas binding to diatomic ligands has immediate parallels to the binding of diatomic substrates in natural systems, the bonding of N-containing heterocylces such as pyridine or imidazole offer many options for synthetic modification to achieve desired binding properties through the introduction of steric bulk or modulation the electron-donating ability of the nitrogen heteroatom. Like bonding to diatomic molecules, the study of iron porphyrin interactions with N-containing heterocycles has long been an area of interest and there are early indications of spin crossover accompanying pyridine coordination to [Fe^{III}TPP]Cl evidenced by both a shift of reduction potentials and breaking of electrochemical reversibility reported by Kadish et al, who also explored the influence of the Hammett parameters of the substituted pyridine ligands.[143] Association constants for some of these Fe^{III} porphyrins with pyridine is higher than what has been reported for Ni^{II} porphyrins but lower than values reported for Co^{III} porphyrins. LogK$_1$ and logK$_2$ values for Fe^{III} porphyrin range from 1.85-2.44 and 0.78-1.29 respectively.[143] Ligand structure and interactions with the larger complex, Low-spin adducts of [Fe^{III}(TPPBr)(1-MeIm)$_2$](ClO$_4$) have been evaluated using EPR and X-ray crystallography and compared to mixed intermediate and high-spin states in the corresponding methanol and water complexes respectively. Hydrogen bonding was shown to be one of the key differences in the conformation of the porphyrins in question and in the case of water/methanol contributed to the stabilization of the low- and intermediate-spin states.[144]

These examples are not necessarily within the scope of CISCO laid out for this review as there was no reversible binding reported for either of the kind that could be used to create a chemical switch, but they do establish that the presence of an axial bound heterocycle may induce a particular spin state in an iron porphyrin system. All that is needed then to create a chemical switch from these systems is to find an appropriate stimulus. Light is one such stimulus and has been used in a particularly interesting spin switch which showcases the synthetic versatility of N-containing heterocycles in designing customizable chemical switches. Solvent effects for an [Fe^{III}TPP](ClO$_4$) showed that the porphyrin assumes a mixed spin state of S=5/2 and S=3/2 in acetone where two acetonate solvent molecules are bound as axial ligands, as well as in cases of mixed ligand involved both acetone and dimethyl sulfoxide, while ligation with dimethyl sulfoxide alone favored only the S=5/2 high-spin state. Coordination of a pyridine ligand, however, yields a low-spin S=1/2 complex. A switching mechanism for this system was devised by Shankar and coworkers through synthetic modification of a pyridine ligand with an azo-bridged substituent at the meta position. Photoinduced *cis/trans* isomerization of this azo-bridge served to control the coordination of the ligand and thus the spin state of the [Fe^{III}TPPP](ClO_4) complex through the steric hindrance introduced by the trans isomer to achieve a switching efficiency of 76%. These ligands could form both 1:1 and 1:2 adducts.

While porphyrins alone may demonstrate many interesting chemical properties with interesting coordination environments there is a limit to how complex a CISCO mechanism may be without other structure features added to the ring. To create more complicated systems, especially ones which more closely mimic the complicated active sites found in enzymes where axial-coordination of amino acid residues and interactions within hydrophilic or hydrophobic pockets control which substrates can reach the active site. Researchers have increasingly looked to synthetically modified porphyrins with functional groups that introduce added steric bulk, enclose one axial position, or even incorporate an axial ligand into the structure. Many of these developments come from an interest in oxygen binding and other forms of catalysis. Oftentimes these involve a hanging functional group above the axial site which helps hold a substrate in a desired conformation above the active site which may also include a coordinating moiety on the opposite side of the porphyrin scaffold at the other axial position. In most cases the proximal base is included not as a spin switch but as a way to ensure that the metal center remains set in the spin state desired for the complex’s catalytic activity by inducing a larger ligand field strength. But there are examples of reversible binding of the proximal base including a triazolate-strapped iron porphyrin investigated by Peters et al.[70] which undergoes a multistep CISCO mechanism beginning with a proximal axial ligand which switchable binding that in its "on" state prepared the metal center for a reversible coordination to a photo-switchable ligand similar to that seen in Shankar's work (Figure 19).[145]

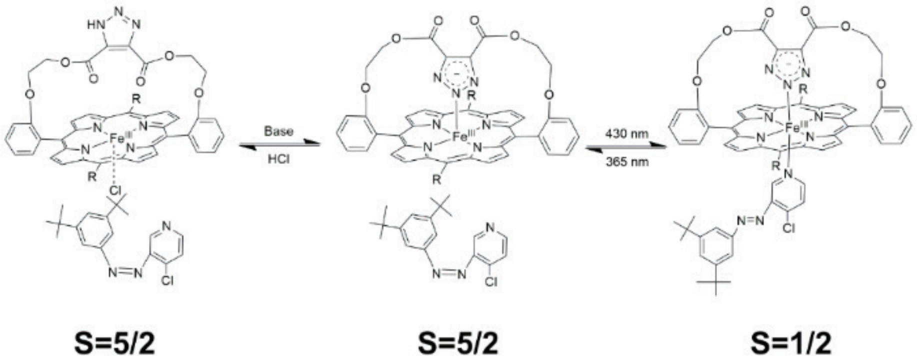

Figure 19: pH-dependent mechanism of CISCO for a triazolate-strapped Fe^{III} porphyrin. Adapted from Shankar et al.[145]

In this system's resting state, a 1,2,3-triazolate is held above the Fe^{III} metal center opposite a chloride ligand. In this configuration the iron center is in a high-spin S=5/2 state. The introduction of a base in solution deprotonates the triazolate and a dramatic conformational change ensues as the negatively charged triazolate moves to coordinate to the Fe^{III} center and simultaneously displaces the chloride ligand which occupies the other axial coordination site. This first binding event activates the metal center towards binding an additional ligand, which causes the Fe^{III} center to assume a low-spin S=1/2 state. This second ligand may be one of several heterocycles including triazolate rings and p-methoxypyridine which may serve to both deprotonate the triazole group and act as a ligand coordinating to the Fe^{III} center, but most notable was a photo-dissociable ligand similar to that employed by Shankar at al., here the p-methoxy version used by Shankar was replaced by a chlorine substituted variant instead. The reason for this, according to the authors, was that the p-methoxy variant would not dissociate in the cis conformation while the chloride derivative did so readily.[70] With the inclusion of this photo-dissociable ligand both binding events are made reversible. The initial triazolate binding may be reversed through the addition of hydrochloric acid and the binding of p-methoxypyridine can be reversed through a photoinduced cis/trans isomerization of the pyridine ligand.

2.3.1.2 Cobalt Porphyrins

There is a notable absence of research CISCO in cobalt porphyrin systems in the current literature despite the importance of vitamin B_{12} and other cobalt porphyrin groups in biochemical systems.[146] There are however multiple electrochemical studies in the literature where the binding of exogenous pyridine ligands induces shifts in measured redox potentials. This could be a sign that ligand binding is modulating the spin exchange equilibrium for the $Co^{III/II}$ redox couple.

An example of this was published by Yan et al. They observed a change in the electrochemistry of cobalt tetraphenylporphyrin in the presence of pyridine. Here they observed a marked shift in both reduction and oxidation potentials was observed. Following the addition of pyridine the oxidation peak shifted from 0.8 V vs SCE to 0.34 V vs SCE while the single reduction peak at 0.678 V vs SCE split and became two peaks at 0.25 V vs SCE and -0.40 V vs SCE which was attributed to the $[Co^{III}(TPP)(py)]$ and $[Co^{III}TPP(py)_2]$ adducts respectively.[147] Other examples in the literature study these interactions in more depth, although it can be difficult to judge the electrochemical irreversibility in cases where the authors chose to report only half-potentials. Truxillo et al. investigated the effect of added pyridine on the half-wave potentials of $Co^{III/II}$TPP and $Co^{II/I}$TPP redox couples. Results obtained in the course of these studies indicated shifts in the reduction potentials of both the Co^{III} and Co^{II} states attributed to dipyridyl and monopyridyl adducts respectively. A negative shift in the half-wave potentials of 320 mV was reported for Co^{III} and 730 mV for Co^{II}.[148] Similar results were observed by Kadish et al.[143] and by Jester et al.[149] Association constants for Co^{III} porphyrins are high indicating that these presumed lo-spin adducts form readily. Values for logK_1 range from 3.65 to 4.15 depending on solvent conditions and porphyrin structure while association constants for Co^{II} porphyrins are considerably lower with logK_1 values ranging from 1.15 to 1.58.[143] The low Co^{II} association constants compared to Co^{III} support the hypothesis that pyridine is dissociating following reduction of the Co^{III} state although one author did report the presence of a mono-pyridyl Co^{II} adduct following the reduction of the dipyridyl Co^{III} complex.[148]

None of the authors in the above examples chose to discuss the spin states of the cobalt porphyrins under study. Given that Co^{III} is known to favor six-coordinate low-spin coordination environments it is not unreasonable to assume that the formation of a low-spin $[\mathrm{Co^{III}TPP(py)_2}]^+$ is responsible for the negative shifts in reduction potential. With the high association constants reported in literature these systems have the potential to become reliable ligand-regulated spin switches if more attention is devoted to studying them.

2.3.1.3 Nickel Porphyrins

Ni^{II} porphyrins are unique among the compounds we cover here. With eight d-electrons, Ni^{II} is not normally included in discussions of spin crossover, although some authors have described spin crossover and “spin crossover like” behavior in complexes of Ni^{II} in non-CISCO contexts.[150,151] Within the growing CISCO subfield Ni^{II} complexes have achieved a place of prominence with many creative examples of molecular machinery intended to control ligand binding. Instead of undergoing a spin transition from high-spin to low-spin upon coordination, Ni^{II} porphyrins switch from low-spin to high-spin upon ligand coordination. This interaction is shown in Figure 20.

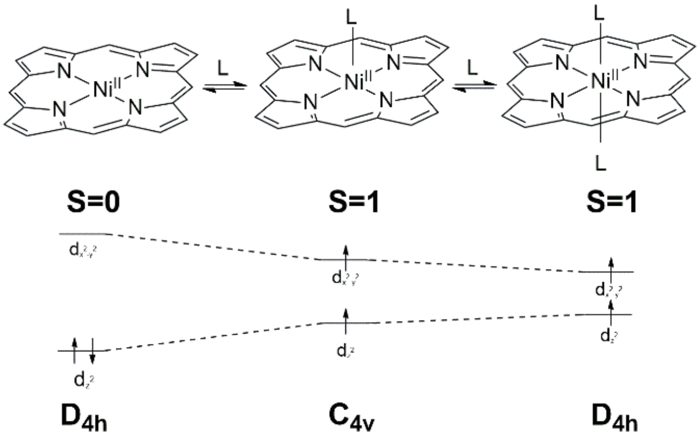

Figure 20: Electronic reaarangment in a Ni^{II} porphyrin following coordination. Adapted in part from similar figures by Thies et al.[124]

This is a consequence of changes to the electronic structure of the nickel (II) metal center as additional ligands are added and changes to its geometry result. With the addition of the first ligand the initial square planar four coordinate nickel (II) assumes a five-coordinate square pyramidal geometry. This change lowers the energy gap between the $d_{x^2-y^2}$ and d_{z^2} , allowing the previously paired electrons residing in the d_{z^2} orbital to separate with one electron moving to the $d_{x^2-y^2}$ orbital giving an overall spin of S=1. The addition of a second ligand converts the complex to an octahedral geometry where the two orbitals are now degenerate, thereby serving to stabilize the high-spin state. This interaction is not as highly favored as is the case for Co^{III} porphyrins. Association constants, determined at room temperature, describing the formation of the pyridine adducts in solution are low, but sufficient to induce a spin change with $\log K_1$ values ranging from -0.17 to 1.48 and $\log K_2$ values ranging from 1.06 to 1.36.[58]

Interactions between Ni^{II} porphyrin and heterocycles have been a subject of study for decades.[152,153] Recent studies of CISCO interactions with discrete ligands in solution have been performed by Thies through simply titration with pyridine and also in a switchable context using the photo-isomerizable ligand 3-phenyl-azopyridine and found that the percentage of complex converted to high-spin could be varied via irradiation with different wavelengths of light.[58,124] CISCO at air-water and metal interfaces has been an area of interest.[154,155] Switchable CISCO has been show in in these interfacial environments in the case of light-induced coordination of pyridine on TiO_2 thin films.[94]

This behavior is notable not only for being unique among CISCO complexes, but also because the "inverse" transition makes these compounds more useful in other contexts. One proposed application of Ni^{II} porphyrins that would particularly benefit from this are MRI contrast agents as an appropriate photosensitive ligand would allow these sensitizers to be activated through a conversion to a high-spin state in regions of particular interest.[156] This advantage has been highlighted in the work of Dommaschk et al featuring the Ni^{II} porphyrin Ni-$TPPF_{20}$, with photo-dissociable ligands in water (Figure 21).

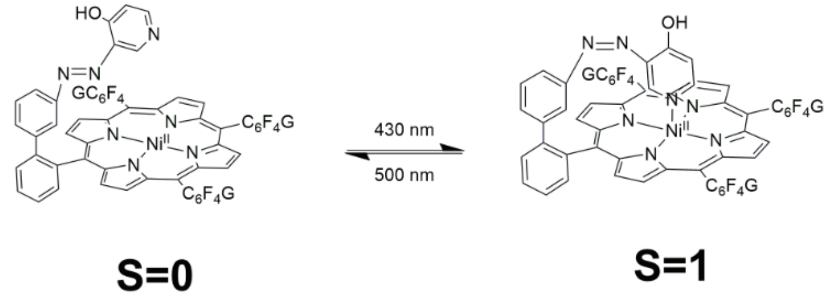

Figure 21: Water-soluble light-driven CISCO porphyrin spin switch demonstrated. Structures adapted from Dommaschk et al.[96]

Ni-$TPPF_{20}$ is water soluble thanks to the inclusion on glycerol side chains connected to the porphyrin ring, which when coordinated to the Ni^{II} center ensures a sufficiently electron-deficient environment to encourage axial coordination. Upon axial coordination, the complex assumes a paramagnetic S=1 state.[96] This water-soluble porphyrin concept was later combined with that of a porphyrin incorporating a 3-pheynyl-azopyridine proximal ligand, which achieved control over the coordination of this substituent through the cis/trans isomerization induced in the azopyridine at 500 and 430 nm,[157] resulting in a water-soluble record-player porphyrin that showed photo-induced CISCO. Interestingly, the azopyridine in this case was further modified with an additional electron-donating hydroxyl to increase the basicity of the proximal ligand, basicity that could be further increased by deprotonation of this hydroxyl group.[158]

2.3.2 Metallo Salens

Salens or salophens, are a popular group of chelating organic ligands which encompass a wide array of structure motifs all arranged around a common core structure consisting of a pair of phenolate oxygen donors alongside a pair of Schiff base nitrogen donors. The generic structure of the salen ligand is shown in Figure 22 with the synthetically modifiable groups labelled as R_1, R_2, and R_3 respectively.

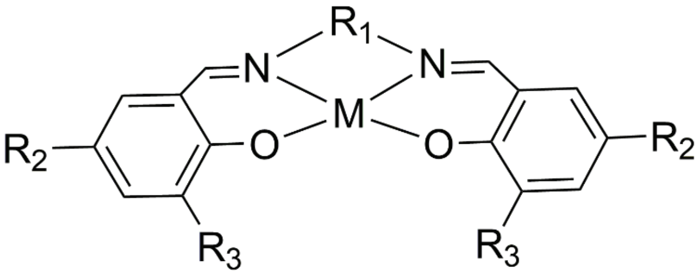

Figure 22: Generalized structure of a metal salen complex where R_1, R_2, and R_3 represent structural features that may be changes synthetically to tune behavior.

Most salens are tetradentate ligands favoring square planar coordination to the metal center leaving two open coordination sites. Owing to their ability to coordinate to metal ions in a variety of oxidation states and the ease of synthesis, salens have become popular scaffolds for new transition metal catalysts.[159,160] Like porphyrins, salens can be readily modified using conventional synthetic techniques. Classical salens are tetradentate ligands, but modification of the bridge between the two phenolate moieties (R_1) may introduce an additional nitrogenous base to give a pentadentate ligand. This modification alone is immediately of interest to any researcher looking to design a new CISCO molecule as this modification will change the number of open coordination sites available to an exogenous ligand from two to one. The R_2 and R_3 positions are also significant. Both positions allow for modifications to the electron distribution across the molecule to tune redox properties and the acidity of the metal center.[161–163] Additionally, modifications at R_3 might allow for other changes relevant to CISCO such as the addition of sterically bulky groups to regulate binding.[164,165] R_2 could also be modified to confer changes in solubility or to allow incorporation into polymeric materials.[166]

Many salens display thermal SCO behavior. Most of the available studies focus on the properties of both bound and unbound salens with iron, manganese, and cobalt metal centers.[167–171] This research is often carried out in the context of catalysis and there are few examples of salens investigated as molecular switches. While this research may not explicitly focus on SCO behavior, the catalytic mechanisms typically involve oxygen binding to the salen metal center before reacting with substrate molecules. While SCO is often not explicitly the focus of this research the existing literature may be instructive for future salen CISCO work. Salens are often used as asymmetric catalysts where coordination to and dissociation from the metal center are vital to their mechanisms.[160,170,172–174] Oftentimes four-coordinate salens are synthesized with an additional axial ligand which influences the behavior of the catalysts.[175–177] The addition of these ligands and the improvements to catalytic efficiency speak to the influence of the exogenous ligand on the metal center. All that would be needed to exploit this influence for CISCO is to find an appropriate mechanism to regulate binding.

In the 1980s Kennedy and coworkers published the results of numerous studies of cobalt and iron salens undergoing thermal SCO in a variety of conditions.[167,168] One of these works reported on the tunable thermal SCO behavior of a four-coordinate cobalt(II) salen. It was found that the transition temperature of the Lewis base adducts of this salen varied along with the structure of the Lewis base involved including imidazole and benzimidazole derivatives. In the case of one variant, a cobalt salophen complex coordinated to 2-methylimidazole a high-spin state was seen to be favored and attributed to structure distortions associated with ligand binding.[168] Similar cobalt(II) salens and their pyridyl adducts have since be studied using EPR where a similar correlation was found between sigma-donor strength and the increased formation of the high-spin adduct.[57] These examples are interesting, but due to the d^7 configuration of the Co^{II} metal center a diamagnetic low-spin state remains unobtainable. Like cobalt porphyrins, it would seem that much of the potential utility for cobalt salens as spin switches may require the incorporation of redox changes as well.

Zhang et al have investigated a Co^{III} salen bound to 1-methylimidazole where the redox properties could be modulated by changing the substituents on the salen's phenolate rings. Crucially, the electrochemistry indicated a significant electronic rearrangement upon conversion to the Co^{II} state indicating that 1-methylimidazole dissociates upon reduction. Differences in electrochemical behavior were also shown for synthetic variants of 1-methylimidazole coumarin ligands, demonstrating a relationship between axial ligand structure and electrochemistry.[163] These results are encouraging for the development of chemical spin switches based on CISCO interactions and agrees well with data collected in our own research. Cobalt bissalen complexes synthesized for use as electrocatalysts in our lab have shown spin crossover behavior as part of their catalytic cycle.[178] This led to the investigation of a simpler cobalt salen seen in Figure 23.

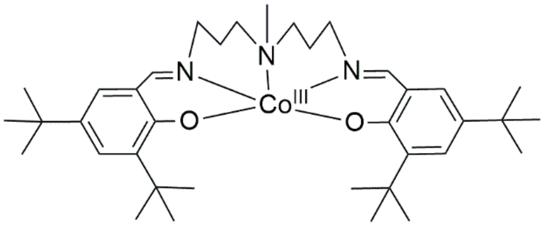

Figure 23: Structure of five-coordinate cobalt salen synthesized by Buchwald et al. Adapted from similar figures in the original publication.[125]

The spin state of this salen can be altered through a redox reaction that convert the complex that coverts the cobalt center from a high-spin d^7 Co^{II} to a high-spin d^6 Co^{III}. This high-spin Co^{III} can be converted to a low-spin state by coordination of pyridine which also results in increased reduction potentials much like behavior seen in cytochromes.[111,117,125] Further research by our group has demonstrated that this behavior can be modulated by changing the axial ligand and has been investigated using pyridine-derivatives, nitrogen heterocycles, as well as a handful of anions.

Other salens of interest include the Ni^{II} complexes not unlike the nickel(II) porphyrins synthesized by the Herges group in terms of CISCO behavior have been synthesized by Brandenburg and co-workers. These Ni^{II} salph complexes (Figure 24) feature four-coordinate ligands with two open coordination sites allowing two equivalents of pyridine to coordinate to the metal center and induce a LS to HS transition not unlike similar transitions seen in nickel(II) porphyrins.[58,179]

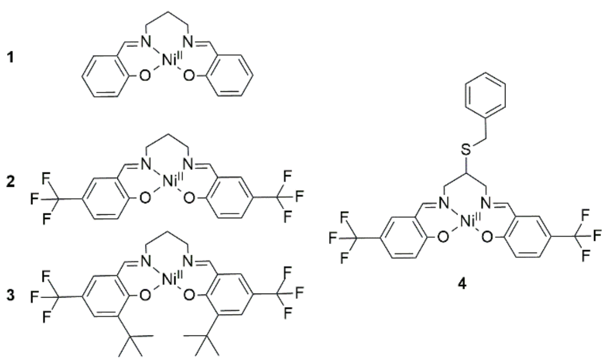

Figure 24: Nickel(II) saluculidenpropylene iminate complexes synthesized by Brandenburg et. al. (1) [Ni(salpn)], (2) [Ni(salpnCF$_3$)], (3) [Ni(salpntBuCF$_3$)], (4) [Ni(salpnSbenz)]. Structures are adapted from similar figures in the original publication.[180]

Their work primarily focused on the investigation of these saph complexes with a variety of R_1, R_2, and R_3 substituents. Two of these salens, [Ni(salpn)] and [Ni(salpnSbenz)] included no added substituents on the phenol rings while [Ni(salpnCF$_3$)] included electron-withdrawing CF_3 groups at the R_2 positions and [Ni(salpntBuCF$_3$)] added bulky t-butyl groups to the R_3 position. Perhaps unsurprisingly, the CF_3 modified salens demonstrated an increased affinity for pyridine upon titration likely owning the increased in Ni^{II}'s Lewis acidity caused by the electron withdrawing CF_3 groups. Modification at the R_1 position in the case of [Ni(salpnSbenz)] on the other hand was seen to decrease the complex's affinity for pyridine. Also of note was the interesting behavior attributed to the CF_3 groups which led to aggregations of the complex to form dimers which were broken up by the coordination of pyridine.[180] Most striking about this series of molecules is [Ni(salpnSbenz)], which hints at future variations of this complex which incorporate proximal ligands into the salen backbone. Here, the inclusion of this added functional group at the R_3 position decreased the complexes overall affinity for pyridine, but this is a shortcoming that could be overcome in the future with a proximal ligand modified with electron-donating groups to increase the basicity of the proximal ligand and enforce binding.

In summary, there are a number of intriguing salen complexes that display signs of CISCO upon ligand coordination but there are clear gaps in this segment of CISCO research that have yet to be filled. Given the importance of salens in catalysis it may not be unreasonable to suggest that more detailed studied of CISCO interactions might lead to the development of new catalysts with tunable reactivities. Other applications could include sensors and molecular switches in general as well. This would likely require the design of new salen ligands incorporating Lewis basic pendant groups as some authors have already indicated interest in exploring.

2.3.3 Other Coordination Compounds

Research into ligand binding in non-porphyrin compounds where spin crossover is the focus is somewhat more difficult. This is surprising since the prevalence of these interactions in a wide array of natural systems peaks to their utility. It stands to reason that while porphyrins that undergo CISCO may be versatile, exploring alternative ligand structures may lead to yet more functionalities and enable the design of new catalysts and chemical sensors. Fortunately, while porphyrins have gotten a great deal of the spotlight for several decades, there have been multiple examples of CISCO in recent years as the field continues to develop. This section seeks to highlight selected examples of CISCO and the mechanisms through which ligand coordination can be controlled.

2.3.3.1 pH Dependent SCO in [Fe(bipy)3]$^{2+}$

One particularly interesting example in recent years has been presented by Nowak et al.[181] Rather than inducing CISCO through the introduction of an extraneous ligand, Nowak and coworkers reported reversible spin state switching in diamagnetic tris(bipyridine)iron(II) ($[Fe(bipy)_3]^{2+}$), seen in Figure 25, and bis(2,6-bis(1H-pyrazol-3-yl)pyridine)iron(ii) ($[Fe(bpp)_2]^{2+}$) through a reversible protonation.

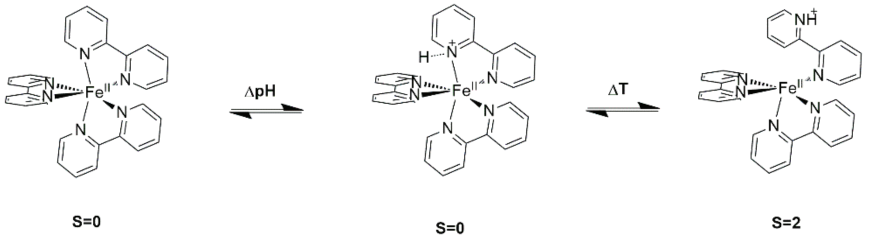

Figure 25: Mechanism of pH-dependent spin-crossover in $[Fe(bipy)_3]^{2+}$. Adapted from Nowak et al.[181]

Initial experiments on $[Fe(bpp)_2][BF_4]_2$ revealed an SCO transition with a $T_{1/2}$ near room temperature, indicating that the weak ligand field compared to the trisbipy complex allows for easy conversion between spin states.[182] Conversely, $[Fe(bipy)_3]Cl_2$ was shown to be entirely diamagnetic as a result of the strong field 2,2'-bipyridine ligands. At pH 1 the nitrogen of one of the coordinated bipyridines is protonated to form $[Fe(bipy)_3H]^{3+}$. This new species is also diamagnetic, but the protonation is followed by a weakening of the nitrogen-iron bond and presumably a decrease in ligand field splitting energy, allowing the iron(II) center to transition to a paramagnetic state upon heating. Additionally, the SCO behavior of this complex when embedded in the zeolite faujasite NaY was also investigated. This zeolite was sufficiently acidic to induce the previously observed SCO changes from LS to HS with the removal of water by heating until an internal pH of 1 was achieved. Results indicated that behavior was highly influenced by the zeolite environment. This unusual example of reversible SCO is an excellent example of a complex with potential applications in chemical sensing and, as the authors note, MRI contrast agents, and highlights the diversity of approaches available to tune the strength of the coordination environment.

2.3.3.2 Fluorescent-Linked Spin Crossover in Planar Ni^{II} Schiff Bases

CISCO behavior has been reported in a series of unique planar Ni^{II} complexes in solutions of chloroform and pyridine. In this complex (Figure 26) the Ni^{II} metal center is located in a Schiff base moiety featuring two synthetically variable R groups with an N_2O_2 coordination environment reminiscent of many four-coordinate salen complexes. Multiple R-group substituents were demonstrated including COOEt, COOOMe, and COMe, at the R_1 positions and CH_3, CF_3 at the R_2 positions. Like those four-coordinate salens, this nickel(II) Schiff base provides two open coordination sites which can be occupied by an axial ligand. In the initial square-planar S=0 state three of the four investigated complexes showed fluorescent behavior when excited with light at 430 or 431 nm.

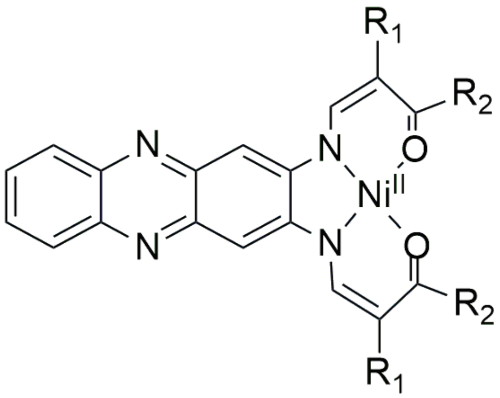

Figure 26: The planar Schiff base synthesized by Kurz et al. Adapted from similar figures in the original publication.[183]

Coordination of the first axial ligand enforces a square-pyramidal geometry with a full octahedral environment achieved by coordination of a second ligand. Coordination both induced a conversion to an S=1 state and also caused a bleaching effect and after coordination no fluorescence was observed. Binding affinity is similar to that of Ni^{II} porphyrins and pyridine. Results indicated that the R_2 substituent could also influence binding behavior and the nickel(II) center was markedly more acidic in the case of the CF_3 variant with logK values ranging from 0.88-1.08 depending on the ligand used.[183] This complex is notable not only for its CISCO behavior but also its fluorescent properties as well giving it a versatility not seen in other complexes.

2.3.3.3 CISCO in a Ni^{II} Dipyridyl Complex

Building on the extensive work now available in the literature on CISCO in nickel(II) porphyrins, Klaß and coworkers evaluated a unique dipyridyl nickel(II) complex seen in Figure 27 that displayed a low-spin to high-spin shift upon coordination by pyridine.[179]

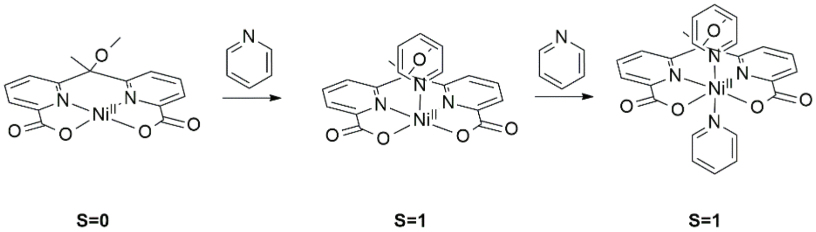

Figure 27: The nickel dipyrdyl complex synthesized by Klaß and coworkers shown with interactions with pyridine in solution. Structures adapted from similar figures in the original publication.[179]

Design of the dipyridyl ligand was assisted by computer simulations to screen for structures that would yield promising binding properties. Structures that would be amenable to future synthetic modifications to include azide switches and other functional groups were explicitly sought out. Like other systems, association of the pyridine ligands is temperature dependent. LogK_1 for this complex was larger than what has been reported for Ni^{II} porphyrins at 2.39 with logK_2 an order of magnitude lower at 1.46. Notably, the resulting complex displayed some level of paramagnetic behavior prior to the addition of pyridines. Calculations then showed that the carbonyl groups were able to coordinate to the nickel(II) centers of adjacent complexes forming dimers in solution and even adducts in which the metal center was coordinated to one pyridine moiety and one adjacent complex simultaneously.

2.3.3.4 Crystaline CISCO in a Dinuclear Ni^{II} Complex

An outlier among the complexes highlighted here, this recently reported dinuclear nickel(II) complex [Ni$_2$(hbth)(py)$_6$] which in the solid phase displayed thermally driven CICSCO behavior. Shown in Figure 28, this complex two nickel centers are linked by an N′1,N′4-bis((E)-2-hydroxybenzyli-dene)terephthalohydrazide ligand and each metal center is coordinated by an additional three pyridine ligands each. Crystals of this complex were prepared by slow evaporation giving a red crystalline solid with intercalated methanol molecules incorporated into the structure. These crystals are red but upon heating at 135 °C turn to a pink color as the crystal structure rearranges and two pyridines dissociate form each metal center. This is accompanied by a transition from a high-spin S=1 state to a low-spin S=0 state. Soaking the crystals in pyridine restored the initial high-spin state.[184]

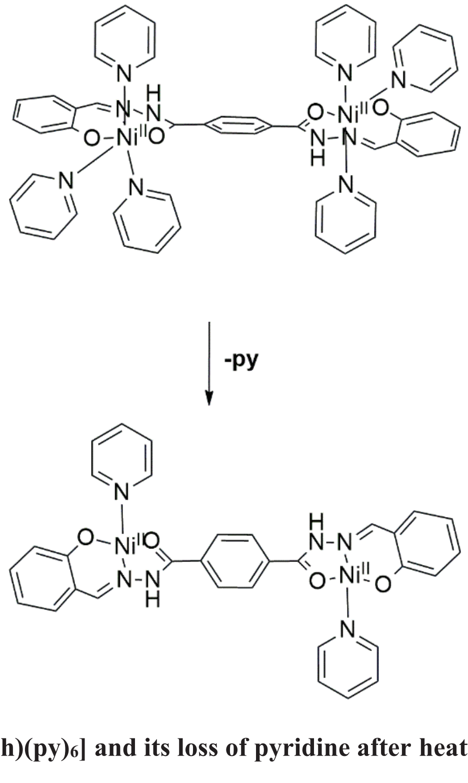

Figure 28: Structure of [Ni$_2$(hbth)(py)$_6$] and its loss of pyridine after heating. Adapted from Zhao et al.[184]

2.3.3.5 Cobaloximes

In looking at the current literature on cobaloximes, one can conclude that further research into the complex could provide interesting insight and a greater understanding of CISCO. Cobaloximes (Figure 29) are compounds in which cobalt is coordinated to two diglyoxime ligands.[185] The molecule can then be further modified by bridging the two diglyoxime ligands with molecules such as BF_2, changing the functional groups on the ligands, or coordinating axial ligands to the cobalt center.[186,187]

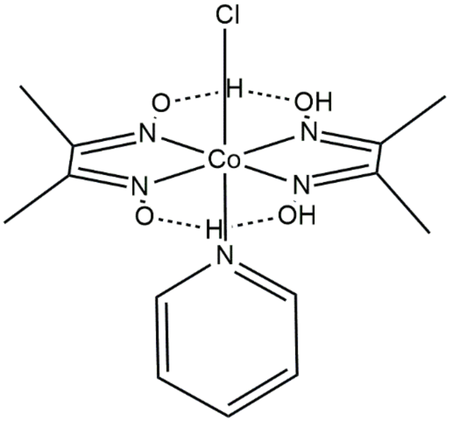

Figure 29: Structure of a typical cobaloxime with pyridine and chloride as axial ligands.

Much of the current research on these complexes focuses on studying the molecule as a vitamin B_{12} model and as a catalyst for hydrogen evolution.[186,188] Axial ligation is an important factor due to the influence they exert on ligand exchange steps in the catalytic cycle.[189–191] While it has been reported that the cobaloxime $[Co(dmgBF_2)_2]$ is low spin (S=1/2) in the Co^{II} state, [192] not much research has gone into evaluating the spin of the metal upon changing the coordinated ligands to the complex. Like cobalt porphyrins, there is a lack of explicit CISCO in the cobaloxime literature but several examples of published electrochemical studies that may indicate underlying CISCO interactions.

One example of this is in the work by Razavet et al where they evaluated cobaloximes as catalysts for water splitting.[193] In particular, interesting data to hint at the possible presence of RCSCO in the complex, is from their evaluation of the electrochemistry of cobaloximes of the form $[Co(dmgH)_2(py)X]$ where dmgH is dimethylglyoxime and X is Cl^-, or I^-. While Razavet and coworkers had an interest in looking at the coordination of the axial ligands upon reducing cobalt from Co^{III} to Co^{I}, it was determined that upon reducing the metal from the +3 to +2 state, one ligand came off, in particular the more labile halide, resulting in the presence of an irreversible $Co^{III/II}$ wave in the CV of the complexes.[193] This resulted in the complexes having $Co^{III/II}$ reduction peaks at different potentials, while the $Co^{III/II}$ oxidation peaks and $Co^{II/I}$ redox waves appeared at the same potentials. This is interesting data, as it indicates the dependence of the coordination to the metal center on the oxidation state of the metal, in addition to the dependence of the potential at which the complex reduces from Co^{III} to Co^{II} on the axial ligand that dissociates. However, while this initial data is promising for the possible presence of RCSCO in these complexes, Razavet and coworkers then went on to explain that the coordination of the halides is slow in the reverse process. This was concluded as once the complex had been oxidized back to the Co^{III} state, a quasi-reversible $Co^{III/II}$ wave was seen in the initial successive CVs in addition to the initial irreversible wave, the presence of this new reduction peak due to the reduction of $[Co(dmgH)_2(py)]^+$.[193] This would make these complexes less favorable for applications in which a quick conversion between the 6-coordinate Co^{III} and 5-coordinate Co^{II} states is desired. Furthermore, more insight into the process is needed, particularly in if this change in coordination and oxidation state is in fact paired with a change in spin to determine if RCSCO is present in these complexes.

While more research is needed to evaluate the presence of RCSCO or CISCO in these complexes, available data further demonstrates the ability to fine tune the electrochemistry of these complexes. In particular, the electrochemistry of the complex is able to be fine-tuned by changing the substituent on the diglyoxime ligands.[187] This was demonstrated in the work by Solis and Hammes-Schiffer, in which they calculated reduction potentials for cobaloximes of the form [Co(dRgBF$_2$)$_2$] where R is CN, CF$_3$, Cl, H, C$_6$H$_5$, CH$_3$, OCH$_3$, OH, or NH$_2$ using DFT.[187] The significance in using these substituents is in the idea that one can study the impact of the functional group on the electrochemistry of the complex using the substituent's Hammett parameter, the chosen substituents providing a range of both positive and negative Hammet parameters.[187] Solis and Hammes-Schiffer found that upon changing the substituent from a more electron withdrawing to a more electron donating group the Co$^{III/II}$ and Co$^{II/I}$ reduction potentials became more negative, the potential difference between these peaks increasing when moving towards more electron donating groups.[187] This demonstrates the ability to fine tune the electrochemistry of the complex based on the substituents of the ligand in addition to the axial ligands bound to the cobalt center, giving scientists the greater ability to functionalize the molecule for their desired applications.

2.4 Conclusion

CISCO is a growing field of research with many opportunities for further progress. There exists a rich variety of both natural and synthetic CISCO systems. Most examples of CISCO research are focused on naturally occurring enzymes, their derivatives, and on synthetic, porphyrin-based analogues of these natural systems. Many of these porphyrin systems have become quite sophisticated in a relatively short time with axial ligands incorporated into the ligand scaffold and molecular machinery capable of inducing spin crossover on demand.

Currently there are numerous paths forward that may prove fruitful. Many complexes have shown promising spin changes upon the coordination of axial ligands but in many instances mechanisms to control these interactions reversibly have yet to be explored. The light- and pH-activated switching mechanisms that have so far been seen in Ni^{II} and Fe^{III} porphyrins warrant more attention and research into how these mechanisms might be incorporated into other ligand scaffolds may prove to be exceptionally fruitful.

Additionally, these proximal ligand mechanisms have not yet been investigated in redox-active systems. Given that CISCO in biochemical systems is often an important control mechanism in electron transport chains it is surprising that there remains so few electrochemical studies of synthetic systems. The examples that do exist of $Co^{II/III}$ redox couples studied in conjunction with exogenous ligands provide an example of how coupling RCSCO and CISCO mechanisms might enable the discovery of novel SCO materials. With these avenues for future research available there are many opportunities for growth in the field of CISCO research which is sure to grow in the comings years as its unique switching mechanisms continue to attract interest.

2.5 Acknowledgements

The cobaloxime section of this chapter was contributed by Andrea Mitchell, whose assistance in conducting literature review process was also invaluable.

3. LIGAND-DEPENDENT REDOX-COUPLED SPIN CROSSOVER OF A FIVE COORDINATE COBALT SALEN COMPLEX

The electrochemical and spectroscopic behavior of a five-coordinate cobalt (III) salen (**Co^{III}Sln^{+}**), where **Sln** is N,N′-bis(3,5-di-tert-butyl-2-hydroxybenzyliden)-1,7-diamino-4-methyl-4-azaheptane, is examined in the presence of a series of exogenous ligands. In non-coordinating solvents, and in the absence of suitable ligands, **Co^{III}Sln^{+}** prefers a high-spin configuration (S = 2/2) and has trigonal bipyramidal geometry. The binding of pyridyl- or imidazole-based ligands generate an octahedral complex that is low-spin (S = 0). X-ray crystallographic structures are reported for **[Co^{III}Sln-ampy]Cl**, **[Co^{III}Sln-ampy](SbF$_6$)**, and **[Co^{III}Sln-cnpy](SbF$_6$)**, all confirming the octahedral coordination environment. In the absence of exogenous ligands, **Co^{III}Sln^{+}** displays an electrochemically reversible redox wave in cyclic voltammograms for the Co$^{II/III}$ couple ($E_{1/2}$ = -0.59 V vs Fc$^{0/+}$). The addition of various ligands (L) to the electrolyte induces a pronounced increase in the anodic-cathodic peak splitting ($E^{o}_{hs} - E^{o}_{ls}$) due to a redox-coupled spin-crossover (RCSCO) mechanism. The reduction potential of **Co^{III}Sln-L^{+}** (E^{o}_{ls}) is highly dependent on the nature and charge of L. To better understand the relationship between ligand properties and the observed electrochemical shift, we performed spectroscopic binding studies of **Co^{III}Sln^{+}** and established a correlation of the observed cathodic peak potentials to well-established thermodynamic parameters, including Hammett parameters of para-substituted pyridines and gas phase basicity (GPB) of all ligands. The broad range of anodic/cathodic peak splitting generated by this series of ligands with **Co^{III}Sln-L^{+}** highlights the ability to tune the RCSCO properties and redox bistability of a complex through coordination

---

Portions of this chapter are in preparation as: McCabe, C. A.; Mitchell, A. L.; Bonitatibus, P. J.; Dinolfo, P. H. Ligand-Dependent Redox-Coupled Spin Crossover of a Five Coordinate Cobalt Salen Complex.

changes with exogenous ligands.

3.1 Introduction

Spin crossover (SCO) is one of the most interesting and widely studied phenomena in transition metal complexes, in part due to the possible technological applications of such species in molecular electronics, memory storage, electrochromics, and display devices.[43,87,194] Spin-crossover has received repeat interest from the inorganic chemistry community ever since the phenomenon was discovered in the early 1930s.[61,195] This interest is primarily due to the ease with which the spin-crossover phenomenon can be observed. These transitions are often accompanied by changes in unit cell volume, bond length, magnetic moment, and color. Because these changes are so readily detectible, spin-crossover materials are potentially useful in any application where control over one or all of those properties is desired.[43,61]

Theoretically, any transition metal complex in octahedral coordination with an electron configuration from d^4–d^7 may exhibit SCO effects, i.e. 2+ and 3+ ions of Cr, Mn, Fe, and Co. The exact conditions needed to induce spin-crossover depend on the strength of the ligand field, in particular the interplay between the octahedral ligand-field splitting parameter (Δ_O) and the ligand pairing energy (Π). If Δ_O is large relative to Π the complex will tend to favor a low-spin configuration. If Π is large and Δ_O is small, then the complex will favor a high-spin electronic arrangement. Spin crossover occurs in complexes where Δ_O and Π are about equal, allowing the d-electrons to assume new configurations in response to external stimuli, such as changes in temperature, pressure, light absorption, and magnetic fields; however, metastable spin states for these complexes often require low temperatures.

Coupling a SCO event to a change in redox state offers a way to increase the room temperature stability of individual spin states through large changes in the ligand field environment around the metal center. Redox-coupled spin-crossover (RCSCO) processes, also referred to as charge transfer induced spin transitions,[196,197] are often utilized in enzymatic reactions to control substrate binding, electron transfer events, and catalytic reactions.[198,199] While more common for Fe species, RCSCO has been observed in a number of Co coordination complexes.[41,79,82,84,200–202]

In these cases, the Co^{II} ions prefers a high-spin configuration ($t_{2g}^5\ e_g^2$, S = 3/2), while the Co^{III} is low-spin (t_{2g}^6, S = 0).[203] There is some debate as to the mechanism for this RCSCO reaction as to whether it is a step-wise or concerted process.[78,204,205] This RCSCO process can be described by a square scheme as shown in Figure 30, with separate spin crossover and electron transfer steps. Here, the horizontal steps are electrochemical reactions for the LS and HS states for the $Co^{III/II}$ couple, with potentials of E^o_{ls} and E^o_{hs} respectively. The vertical processes are low-spin to high-spin conversions in the individual redox states with spin exchange equilibrium constants $K_{se,2+}$ and $K_{se,3+}$ describing the formation of the HS state. In most RCSCO complexes, $K_{se,2+} > K_{se,3+}$ and $E^o_{hs} > E^o_{ls}$ due to the higher ligand field strength of the 3+ metal center. The electrode potentials and spin-equilibrium constants are related by:[66]

$$E_{hs}^0 - E_{ls}^0 = \left(\frac{RT}{nF}\right) ln\left(\frac{K_{se,2+}}{K_{se,3+}}\right) \tag{1}$$

The difference in potential between high-spin and low-spin states ($E^o_{hs} - E^o_{ls}$) will likely be a key parameter in determining the redox bistability of an RCSCO complex in the absence of an applied potential. A large separation in redox potentials will likely provide the hysteresis that is so desired in SCO systems. This redox potential difference is enhanced when the Co^{II} state strongly prefers a HS configuration (large $K_{se,2+}$) and the Co^{III} stabilizes the LS configuration (small $K_{se,3+}$).

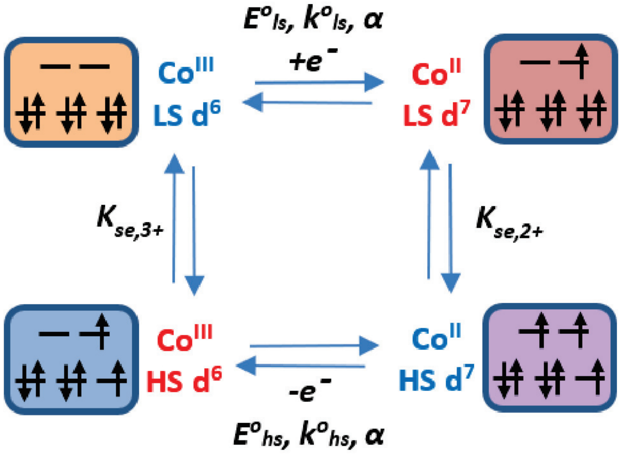

Figure 30: Square scheme for the RCSCO process between Co^{II}/Co^{III} showing individual spin crossover and electron transfer steps. Adapted in part from Turner and Schultz.[66]

We have previously characterized the spin modulation and electrochemical behavior of a five-coordinate Co^{III} Salen complex (**Co^{III}Sln^{+}**, Figure 31) that undergoes RCSCO in the presence of a suitable Lewis base, such as pyridine or acetonitrile, to form **Co^{III}Sln-L^{+}**.[125] We initially prepared this molecule as a model compound to help us understand the electrochemical behavior a dicobalt bis-salen proton reduction catalyst.[178,206] **Co^{III}Sln^{+}** is air-stable with a trigonal bipyramidal geometry and prefers a high-spin triplet ground state. Introduction of an exogenous ligand such as pyridine or acetonitrile yields a six-coordinate complex with low-spin ground state. Notably, the reduced **Co^{II}Sln** has a low binding affinity for pyridine and has a similar trigonal bipyrimidyl geometry as Co^{III}Sln^{+} but with slightly longer bond lengths.[125,207] Cyclic voltammograms (CVs) of **Co^{II}Sln** alone in a non-coordinating solvent, such as dichloromethane (DCM), yield a quasi-reversible wave at -0.59 V versus ferrocene/ferrocenium (Fc$^{0/+}$) that is assigned to the Co$^{III/II}$ couple. Upon addition of pyridine to the electrolyte, the RCSCO properties of this compound are clearly evident from the large separation (~700 mV) of the cathodic and anodic waves for the Co$^{III/II}$ couple.

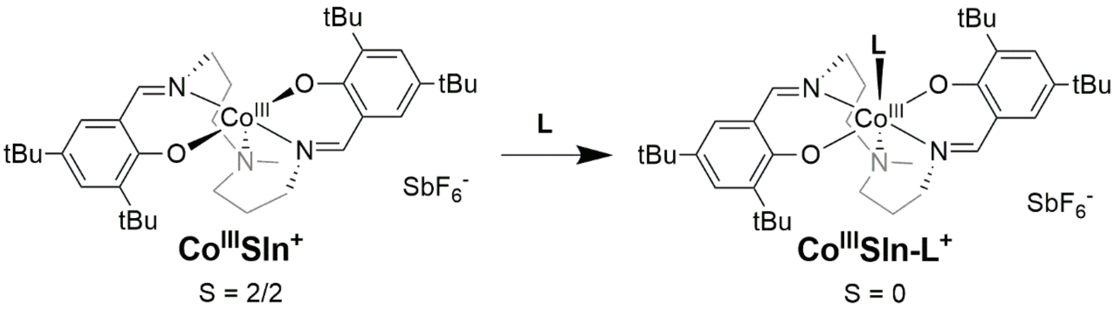

Figure 31: Schematic representation of trigonal bipyramidal Co^{III}Sln$^+$ and the coordination of a suitable ligand (L) to form the octahedrally coordinated Co^{III}Sln-L$^+$.

Though not always explicitly described as RCSCO, there are several examples where coordination of a ligand such as pyridine or imidazole induces a large cathodic-anodic peak splitting for the Co$^{III/II}$ couple due to coordination induced SCO. These include porphyrins,[147] four-coordinate salens,[47] and Schiff base ligands.[208] Several Co salen complexes have been investigated for both ligand- and temperature-dependent SCO.[168] In many instances, the precise nature of the axial ligands bound to the metal center have been shown to have a pronounced effect on spin-state.

In an effort to control the redox bistability of **Co^{III}Sln$^+$** and better understand the factors that control RCSCO in related complexes, we have examined the electrochemical behavior of this complex in the presence of a wider variety of Lewis bases to establish empirical trends based on the structure of the ligands (L). We have established a correlation of the reduction potential of **Co^{III}Sln-L$^+$** with the Hammett parameter for the substituted pyridyl based ligands and the gas phase basicity of all ligands examined. Additionally, we report the structure of three additional **Co^{III}Sln-L$^+$** complexes.

3.2 Methods

3.2.1 Ligand Association Constants

Samples of **Co^{III}Sln$^+$** and **Co^{II}Sln** were prepared in DCM. All ligands were obtained commercially and used as received, except 4,4’-bipyridine and tetrabutylammonium bromide, which were purified via sublimation. Ligand association constants for binding with **Co^{III}Sln^{+}** were determined through absorbance measurements using an Agilent 8453A diode array spectrophotometer running Olisworks software and a quartz cuvette. Guest ligands were titrated into the **Co^{III}Sln^{+}** solution using a microliter syringe and stirred with a magnetic stir bar to ensure the complete mixing of host and guest in the sample.

Global fits applied to these data sets by the open-source browser application “bindfit” generated association constants for all ligands except chloride, hydroxide, and 1,4-bis-((1H-imidazole-1-yl)methyl) benzene (bix). Following these titrations absorbance data was uploaded to the open source bindfit software on www.supramolecular.org Software tools such as this allow a global analysis of titration spectra to be performed while avoiding the errors introduced by linear approximations that might otherwise be employed to determine association constants.[209,210] Links to these fits on bindfits website are listed in Table 4 in APPENDIX A.

3.2.2 X-ray Crystallography

Crystals were secured to a Mitegen mount using Paratone-N oil and single crystal reflection data was collected at 100 K for all compounds (unless noted otherwise) using a Rigaku Oxford Diffraction (ROD) XtaLAB Synergy-S X-ray diffractometer equipped with a HyPix-6000HE hybrid photon counting (HPC) detector and micro-focused Mo Kα radiation (0.71073 Å) or Cu Kα radiation (1.54184 Å). Data collection strategies to ensure completeness and desired redundancy were determined using CrysAlisPro.[211] All data processing was done using CrysAlisPro including absorption corrections applied using the SCALE3 ABSPACK scaling algorithm.[212] All structures were solved by intrinsic phasing methods using ShelXT[213] and refined with ShelXL[214] within the Olex2 graphical user interface.[215] Space groups were unambiguously verified by PLATON.[216] The final structural refinement included anisotropic temperature factors on all constituent non-hydrogen atoms except where noted otherwise (see below). Hydrogen atoms were attached via the riding model at calculated positions using suitable HFIX commands.

Crystals of **[Co^{III}Sln-ampy]Cl** were obtained from a slow diffusion of hexanes into a saturated chloroform solution including a slight excess of **ampy**. Reflection data was collected using Mo Kα radiation. The final R_1 was 0.0498 (8519 reflections) and wR_2 was 0.1323 (9414 reflections). All three aromatic rings in this structure were found to be disordered over two positions, as well as the aliphatic region stemming from the tertiary nitrogen atom of the ligand. In addition, two chloroform molecules would not refine, therefore treated with a solvent mask through Olex2.[215] A solvent mask was calculated, and 96 electrons were found in a volume of 334 Å^3. This is consistent with the presence of two chloroform molecules in the asymmetric unit, therefore 2[$CHCl_3$] were added per formula unit.

Crystals of **[Co^{III}Sln-ampy]SbF$_6$** were obtained from a slow diffusion of hexanes into a saturated chloroform solution including a slight excess of **ampy**. Reflection data was collected using Cu Kα radiation. The final R_1 was 0.0388 (8846 reflections) and wR_2 was 0.0898 (9296 reflections). Like **[Co^{III}Sln-ampy]Cl**, the aliphatic region stemming from the tertiary nitrogen atom of the ligand in this structure was disordered. The aromatic rings were relatively well behaved with disorder found in only one tert-butyl group. The use of excess **ampy** to facilitate crystal growth resulted in **ampy** as solvate in addition to water. Attempts to refine solvate were problematic, therefore a solvent mask was calculated through Olex2[215] with 400 electrons found in a volume of 1282 Å^3 per unit cell. This is consistent with the presence of one molecule of **ampy**, 1[$C_5N_2H_6$], and one-half molecule of water, 0.5[H_2O], per unit cell which accounted for

440 electrons per unit cell.

Crystals of **[Co^{III}Sln-cnpy]SbF$_6$** were obtained from the slow evaporation of a DCM solution containing an excess of **cnpy**. Reflection data was collected using Cu Kα radiation. The final R_1 was 0.0538 (4392 reflections) and wR_2 was 0.1122 (4738 reflections). Due to the extent of disorder, all of the carbons attached to N1 (tertiary amine of the ligand) were left to isotropic refinement. This was noted in the validation response form (VRF). We also modeled the heavily disordered SbF_6 anion which also warranted a response through the VRF.

Angles between phenolate planes were determined using CCDC Mercury software version 2022.2.0.[217,218] Octahedral structure parameters determined using the OctaDist software package (Windows OS version v.2.6.1).[219]

3.2.3 Cyclic Voltammetry

Electrochemical experiments were carried out in dry, degassed dichloromethane with 0.1 M tetrabutylammonium hexafluorophosphate electrolyte (recrystallized from methanol) and 0.05 M **Co^{II}Sln**. Ligands were dissolved in dichloromethane. Scans we performed following each addition using a glassy carbon working electrode, platinum reference electrode, and silver pseudo reference electrode with ferrocene employed as an internal standard following titration. The working electrode was polished with an alumina slurry and dried between additions of the guest ligand. All scans began at -0.4 V vs Fc/Fc$^+$ and were scanned anodically and were performed with either a CH Instruments CHI440 or Pine Wavedriver potentiostat

3.2.4 NMR

^{1}H NMR studies were carried out on a 5003 MHz Agilent spectrometer. Samples were prepared in deuterated chloroform that was filtered through basic alumina prior to use. Samples of **Co^{III}Sln$^+$** were prepared and 1.2 equivalents of guest ligand added. Improvement in resolution of the spectra with the presence of the guest ligands was taken as an indication of the spin change.

3.2.5 GPB Computational Details

Density functional theory calculations to estimate the GPB of **bpy** and **bix** followed established procedures[220] using the PBE1PBE functional[221] and the 6-311+G** basis set. Geometry optimizations were carried out as implemented in Gaussian09, revision D.01.[222] The resulting structures were confirmed as minima by frequency calculations performed at the same level of theory. Calculations were run on the Computational Center for Nanotechnology Innovations at Rensselaer Polytechnic Institute.

3.3 Ligand Binding to Co^{II}Sln and Co^{III}Sln$^+$

The interaction of several different ligands with **Co^{II}Sln** and **Co^{III}Sln$^+$** were examined through spectrophotometric titrations in dichloromethane (DCM). Figure 32 shows some of these ligands including pyridyl based ligands pyridine (**py**), pyrazine (**pyrzn**), 4-cyanopyridine (**cnpy**), 4,4'-bipyridine (**bpy**), 4-picoline (**pic**), 4-aminopyridine (**ampy**), 4-dimethylaminopyridine (**dmapy**), as well as pyrazole (**pyrzl**), imidazole (**im**), 1,4-bis-((1H-imidazole-1-yl)methyl)-benzene (**bix, Scheme 1**), bromide (**Br$^-$**), chloride (**Cl$^-$**), and hydroxide (**OH$^-$**). A schematic showing all ligands is given in Figure 32. The change in absorbance during the titrations of **Co^{III}Sln$^+$** and **Co^{II}Sln** with these different ligands was modeled to provide estimates of the association constants ($K_{a,3+}$ and $K_{a,2+}$), using the relationships shown in Figure 33.

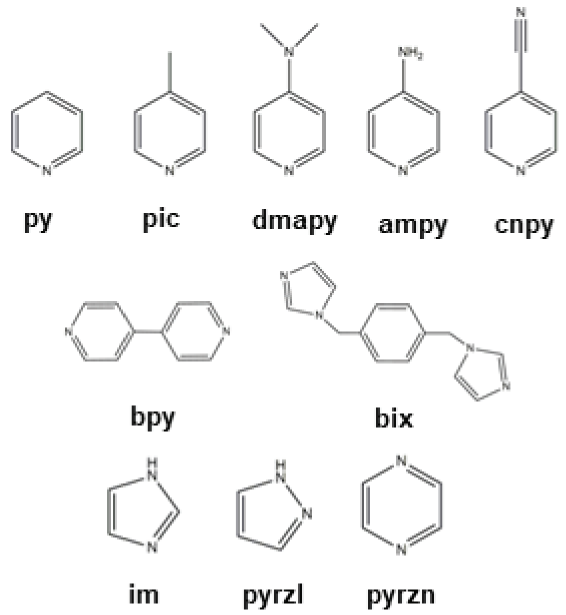

Figure 32: Schematic representation of nitrogen-based heterocycles used to coordinate to $\mathrm{Co^{III}Sln^{+}}$.

$$\mathrm{Co^{III}Sln^{+}} + \mathrm{L} \xrightleftharpoons{K_{a,3+}} \mathrm{Co^{III}Sln\text{-}L^{+}}$$

$$\mathrm{Co^{II}Sln} + \mathrm{L} \xrightleftharpoons{K_{a,2+}} \mathrm{Co^{II}Sln\text{-}L}$$

Figure 33: Ligand binding interactions for $\mathrm{Co^{III}Sln^{+}}$ and $\mathrm{Co^{II}Sln}$ showing the association constants $K_{a,3+}$ and $K_{a,2+}$.

In non-coordinating solvents, such as DCM or chloroform, **$\mathrm{Co^{III}Sln^{+}}$** has a deep green color, with absorption bands at 350 and 484 nm corresponding to π→π* transitions within the salen ligand framework, and 740, seen in Figure 34. The latter two absorption features are ascribed to ligand-to-metal charge-transfer transitions which are characteristic of the high-spin $\mathrm{Co^{III}}$ complex.[47,125] Gradual titration of the five-coordinate high spin complex with guest ligand resulted in a noticeable change in color from green to brown. Figure 34 shows absorption spectra during the titration of **$\mathrm{Co^{III}Sln^{+}}$** with up to 2 equivalents of **im**. Upon coordination, the ligand-to-metal charge-transfer band at 740 nm decreases and there are differences in absorbance around

270 nm which can be partially attributed to the guest ligands and to π-π* transitions in the salen framework. All of this is consistent with previously observed behavior.[125] While the final absorption spectra varied slightly, similar behavior was observed for the other ligands listed above (Figure 35).

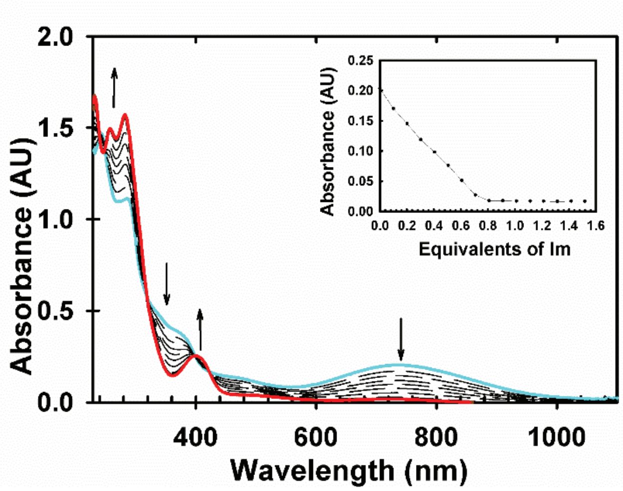

Figure 34: UV-visible-NIR absorption spectra of $\mathrm{Co^{III}Sln^+}$ before (blue) and after (red) titration with im in DCM. The inset shows the change in absorbance at 740 nm versus the number of equivalents of im added to the sample.

Most of the ligands used in these experiments displayed relatively high association constants, resulting in complete conversion to the low-spin **$\mathrm{Co^{III}Sln\text{-}L^+}$** with less than two equivalents added to the solution. These "strong" ligands include **py**, **im**, **pic**, **ampy**, and **dmapy** (Figure 35). Three ligands in particular, **pyrzn**, **cnpy**, and **pryzl** (Figure 36), showed relatively low binding affinity for **$\mathrm{Co^{III}Sln\text{-}L^+}$** and required a large excess to achieve complete conversion. Experimental errors resulting in wide variations in fitting parameters preclude us from definitely stating the association constants of these "strong" ligands but allow us to estimate that they are all on the order of 10^6 M^{-1} with complete conversion seen following the addition of just one equivalent.

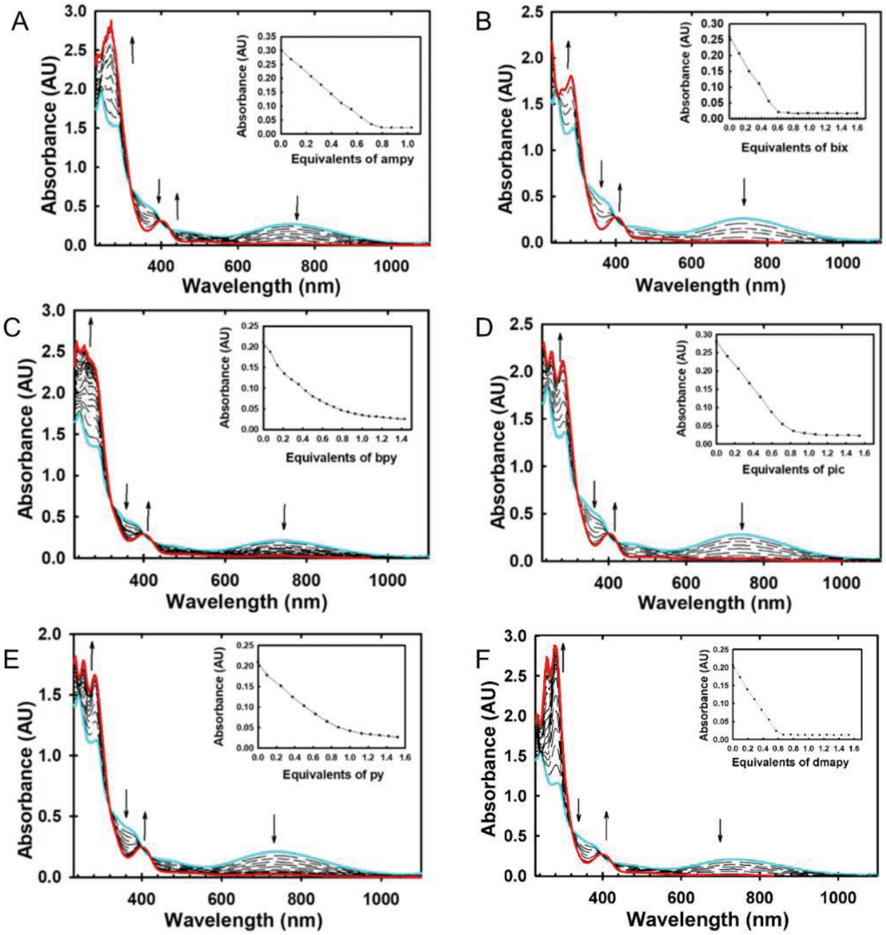

Figure 35: UV-visible absorption spectra of $Co^{III}Sln^+$ before (blue) and after (red) titration with various ligands in DCM. The insert shows the absorbance at 740 nm versus the number of equivalences of ligand. Ligands titrated are as follows: panel (A) ampy (B) bix (C) bpy (D) pic (E) py (F) dmapy.

Three ligands (**pyrzn**, **bpy**, and **bix**) have the potential to bridge two **$Co^{III}Sln\text{-}L^+$**, however only **bix** showed any evidence of this from absorption titrations. **pyrzn** and **bpy**, are both relatively weak ligands and the basicity of the second N atom would be expected to decrease upon initial binding to **$Co^{III}Sln^+$**. Absorption titrations of **$Co^{III}Sln^+$** with **bix** show complete conversion to the bound state at approximately 0.6 eq. Given the high $K_{a,3+}$ for **im**, and the structure of the **bix** ligand featuring two imidazole groups (Scheme 1), this is consistent with the formation of a dimer **$[Co^{III}Sln\text{-}bix\text{-}Co^{III}Sln]^{2+}$**. Similar effects were observed in CVs (vida infra).

Only 4-cyanopyridine required additional equivalents, over ten, to show a similar decrease in absorbance. These differences are shown in the calculated association constants. 4-cyanopyridine had the lowest association constant of the ten ligands for which association constants were calculated and was the weakest of the three weak ligands. The other two weak ligands, **pyrzl** and **pyrzn**, both displayed low binding affinity while also undergoing similar spectroscopic changes with gradual titrations. These three "weak" ligands meanwhile show intermediate association constants on the order of 10^4 M^{-1}.

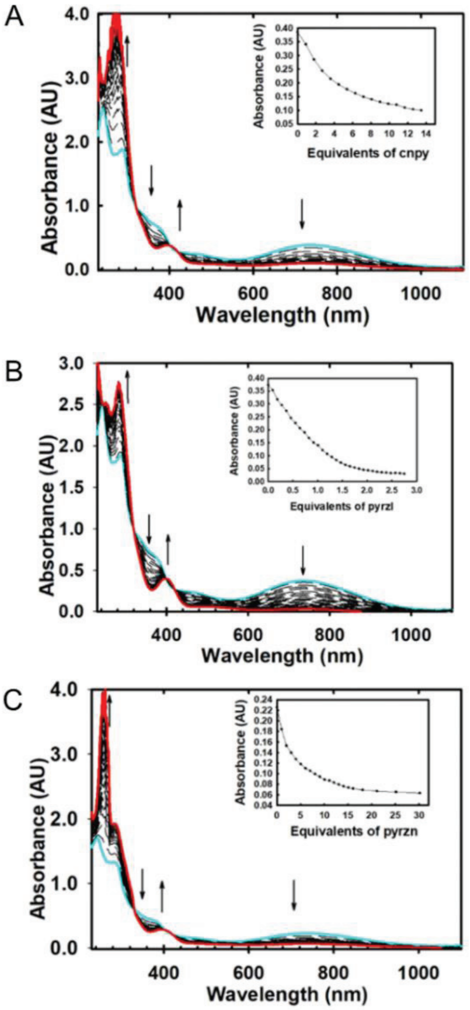

Figure 36: UV-visible absorption spectra of $Co^{III}Sln^+$ before (blue) and after (red) titration with various ligands in DCM. The insert shows the absorbance at 740 nm versus the number of equivalences of ligand added to the sample. Ligands titrated are as follows: panel (A) cnpy (B) pyrzl (C) pyrzn.

Conversion of high-spin **$Co^{III}Sln^+$** (S = 2/2) into low-spin **$Co^{III}Sln\text{-}L^+$** (S = 0) was confirmed by ^{1}H NMR spectroscopy for L = **im**, **pic**, **ampy**, **dmapy**, **bpy**, **pyrzl**, and **bix**. ^{1}H NMR spectra of **Co^{III}Sln$^+$** shows paramagnetically broadened and shifted peaks that are difficult to discern from the base line when viewing the entire spectrum (Figure 37). The majority of the aromatic and aliphatic peaks, shown by arrows in Figure 37, are shifted considerable. The two peaks originating from the imine and aromatic protons are downshifted to 35 and 36.3 ppm while peaks assigned to the amine methyl group, propylamine backbone, and tert-butyl groups are upshifted to -4.4, -12.8, and -1.62 ppm. Only a pair of multiplets at 4.7 and 2.94 ppm, also assigned to protons on the propylamine backbone, can be seen readily in the spectrum. Upon addition of a slight excess of ligands shown above, the ^{1}H NMR signals sharpen and move back into the diamagnetic region. This is shown individually for imidazole in Figure 38 and for all of the above "strong" ligands in Figure 39. This is consistent with the changes in UV-visible-NIR absorbance profiles, in particular the decrease in LMCT bands at 740 nm, and what was observed previously with **py** as a ligand.[47,125]

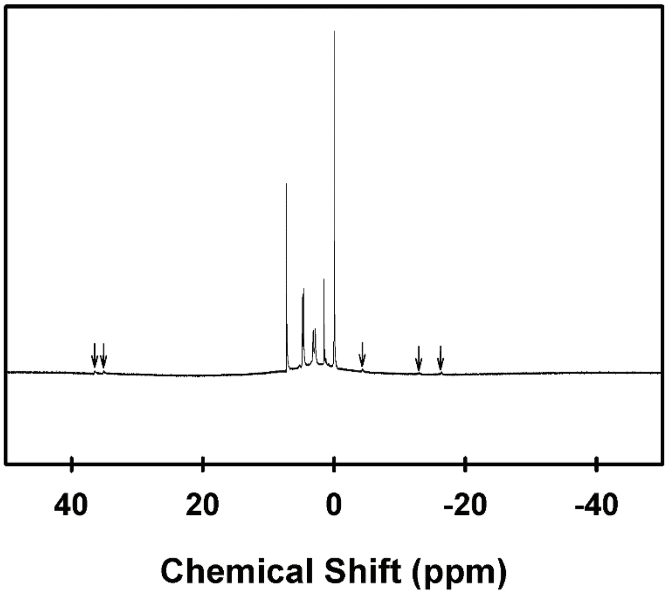

Figure 37: 1H NMR spectra of CoSln$^+$ in deuterated chloroform.

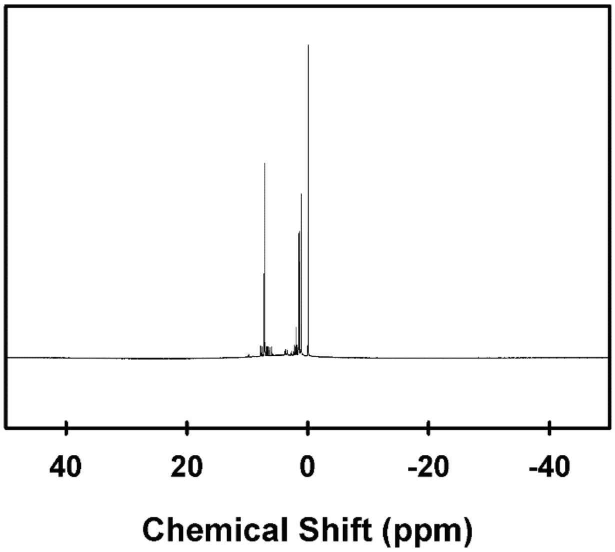

Figure 38: ^{1}H NMR spectrum of CoSln$^+$-Im in deuterated chloroform.

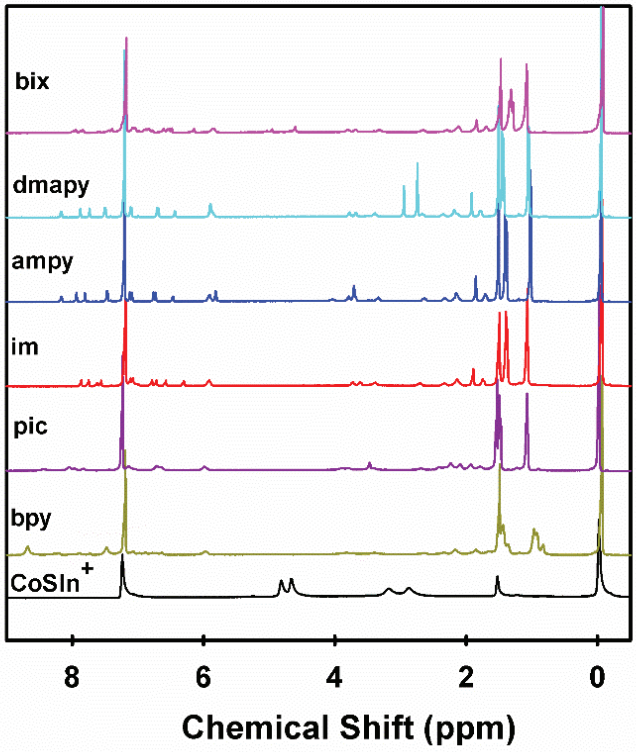

Figure 39: NMR spectra of Co^{III}Sln$^+$ in deuterated chloroform alone (black) with bpy (gold) pic (purple) im (red) amply (blue) dmapy (cyan) and bix (pink).

In titrating **Co^{II}Sln** in DCM with the strongest donor ligands examined herein, it was confirmed that there is very weak binding interactions between these ligands and the Co^{II} metal center (Figure 40). This included **py**, **bpy**, **im**, **pic**, **bix**, **ampy**, and **dmapy**, in which no significant change in the absorbance spectrum at 360 nm upon titrating **Co^{II}Sln** with up to 5000 equivalents of these ligands was seen, aside from the titration with **im** (**Figure 40**). The ligand association constant ($K_{a,2+}$) for the binding of **im** to the Co^{II} metal center was calculated as 30.89 M^{-1}. This is several orders of magnitude less than that calculated for the binding of **im** to the Co^{III} metal center, supporting the favored coordination of these ligands to Co^{III}. Further, no significant changes in the absorption spectrum of **Co^{II}Sln** was observed with up to 5000 eq **cnpy**, so it was assumed that **pyrzn**, **pyrzl**, and **cnpy** display negligible binding to the Co^{II} metal center.

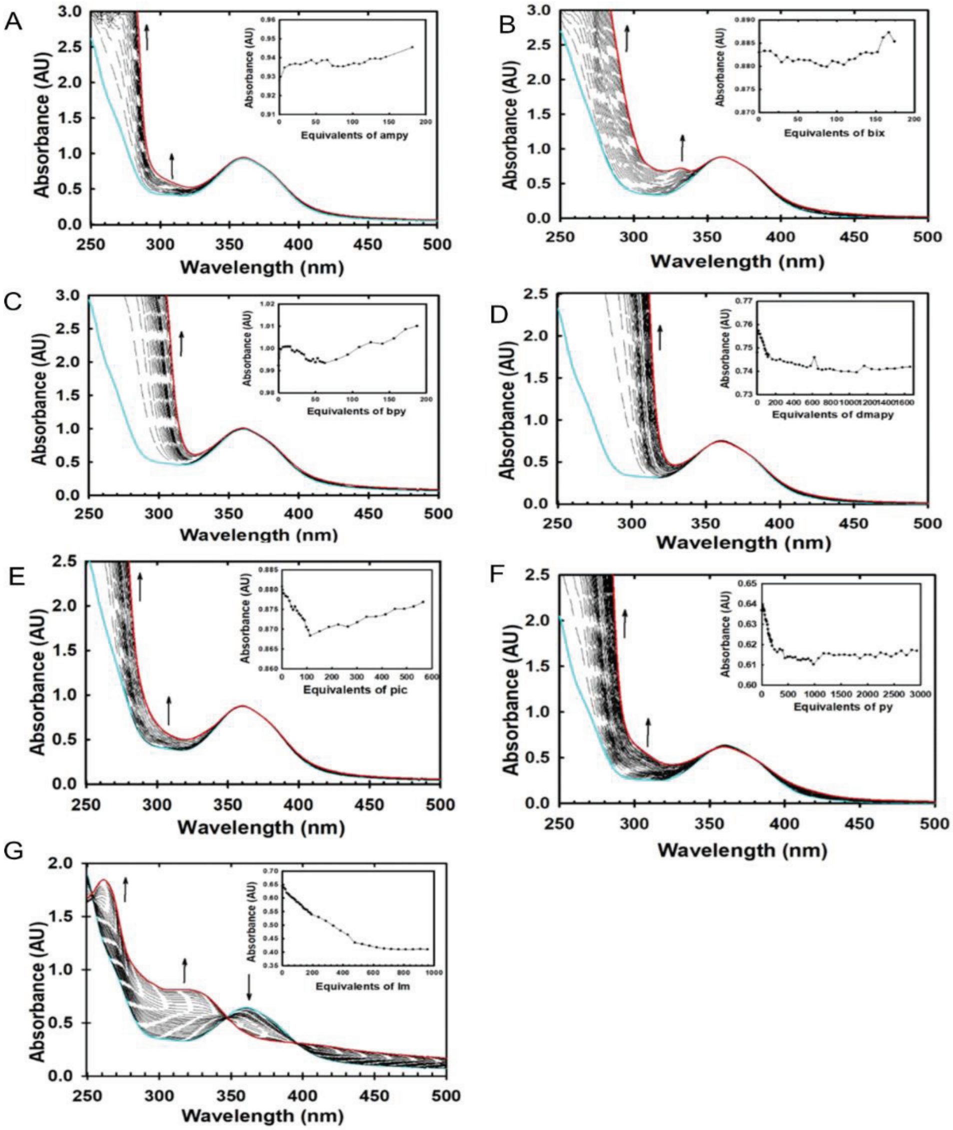

Figure 40: UV-visible absorption spectra of Co^{II}Sln before (blue) and after (red) titration with various ligands in DCM. The insert shows the absorbance at 360 nm versus the number of equivalences of ligand added to the sample. Ligands titrated are as follows: panel (A) ampy (B) bix (C) bpy (D) dmapy (E) pic (F) py (G) im.

3.4 X-ray Crystal Structures

Crystals suitable for X-ray diffraction studies were obtained for **Co^{III}Sln^{+}** bound to two additional ligands, **ampy** and **cnpy**, in order to compare with the previously determined **Co^{III}Sln^{+}** and **Co^{III}Sln-py^{+}**.[125] These ligands span a large range of Hammett parameters for the pyridyl based ligands used in this study. Structures of **Co^{III}Sln-ampy^{+}** were determined with two different counter ions, Cl^{-} and SbF$_6^{-}$. Table 1includes crystallographic data and structural refinement parameters for the three new structures. ORTEP diagrams for the new structures are shown in Figure 41. Bond lengths and angles for the Co coordination sphere, as well as octahedral structural parameters are shown in Table 2.

Table 1: Crystallographic data and dtructural refinement parameters for [Co^{III}Sln-ampy](Cl), [Co^{III}Sln-ampy](SbF6), and [Co^{III}Sln-cnpy](SbF6) after solvent mask applied, and [Co^{III}Sln-cnpy](SbF6). after solvent mask applied, and [Co^{III}Sln-cnpy](SbF$_6$).

	[Co^{III}Sln-ampy](Cl) · (CHCl$_3$)$_2$	**[Co^{III}Sln-ampy](SbF$_6$) · (ampy) · (H$_2$O)$_{0.25}$**	**[Co^{III}Sln-cnpy](SbF$_6$)**
empirical formula	C42 H63 N5 O2 Co Cl	C42 H64 N5 O2.25 Co Sb F6	C43 H59 N5 O2 Co Sb F6
fw	764.35	969.69	972.66
crystal system	monoclinic	monoclinic	orthorhombic
space group	P 21/c	C2/c	Pbcn
a [Å]	14.5332(2)	21.5363(3)	9.8392(1)
b [Å]	17.4832(2)	17.9499(2)	23.1355(3)
c [Å]	20.5973(3)	26.9202(4)	19.9391(2)
α [deg]	90	90	90
β [deg]	100.7680(10)	109.429(2)	90
γ [deg]	90	90	90
V [Å^3]	5141.35(12)	9814.0(3)	4538.83
Z	4	8	4
T [K]	99.98(13)	100.00(10)	100.00(10)
λ [Å]	0.71073	1.54184	1.54184
ρ (calcd, g/cm^3)	0.988	1.449	1.423
μ (mm^{-1})	0.418	7.52	8.132
R1^a [I>2σ(I)]	0.0498	0.0388	0.0538
wR2^b (all data)	0.1323	0.0898	0.1122
GOF^c on F^2	1.031	1.053	1.0356

^{a} $R1 = \sum||F_o| - |F_c|| / \sum|F_o|$
^{b} $R_w(F_o^2) = [\sum [w(F_o^2 - F_c^2)^2] / \sum wF_o^4]^{1/2}$
^{c} $GOF = [\sum[w(F_o^2 - F_c^2)^2] / (N_{obs} - N_{params})]^{1/2}$

[Co^{III}Sln-ampy]Cl crystalized in the monoclinic P2$_1$/c space group with two disordered chloroform molecules. The structure also had some disorder in the **ampy** ligand bound to the Co center and both phenol rings. **[Co^{III}Sln-ampy](SbF$_6$**) crystalized in the monoclinic C2/c space group with an extra disordered **ampy** ligand and water molecule. **[Co^{III}Sln-cnpy](SbF$_6$**) crystalized in the orthorhombic Pbcn space group. All three structures are chiral with respect to the rotation of the salen ligand coordination about the Co center and both isomers are present in the structures. Two additional isomers are also possible with respect to the position of the methyl group on the N-methyldipropylamine backbone, however these are disordered in all three structures. Similar affects were observed for **Co^{III}Sln-py$^+$** previously.[125] Additionally, several of the *t-butyl* groups on the phenolate rings were disordered in the structures.

The N-methyldipropylamine backbone imposes a butterfly-like structure of the salen ligand framework around the Co center. Each *ortho*-imino-phenol comprising the salen ligand coordinates the Co with the phenolic O *trans* to each other. The angle of the phenol rings with respect to each other does not vary significantly from **Co^{III}Sln$^+$** (111.5°) to the pyridyl bound structures (100.9 – 122.0°), suggesting the N-methyldipropylamine backbone dictates the shape of the structure through the imine linkages rather than coordination of ligands. **Co^{III}Sln$^+$** assumes a distorted trigonal bipyramidal geometry around the cobalt center in which the imine nitrogens are held in a *trans*-axial configuration by the N-methyldipropylamine backbone with the phenolate oxygens and the amine nitrogen occupying equatorial positions with respect to the cobalt.[125] Similar coordination was observed for the reduced **Co^{II}Sln**.[207] Upon coordination of the pyridyl ligands, the complex assumes an octahedral geometry in which the relative coordination environment is preserved. The O_{phenol}-Co-O_{phenol} bond angle increases from 129.4° in **Co^{III}Sln$^+$** as expected for trigonal bipyramidal geometry, to 175-177° in the pyridyl bound structures. Additionally, the two N_{amine}-Co-O_{phenol} bond angles decrease from 115° to 91-92° in the octahedral structures. The Co coordinate bond distances in all **Co^{III}Sln-L$^+$** structures are slightly longer, but consistent with other low-spin Co^{III} complexes with traditional four-coordinate salens and two axial ligands.[47,163,223] The slightly longer Co-O$_{phenol}$ (~0.03 Å) and Co-N$_{amine}$ (~0.02 Å) bond lengths in **Co^{III}Sln-L^{+}** is likely the result of the butterfly shape and steric restrictions of the N-methyldipropylamine backbone.

Octahedral distortion parameters are included in Table 1 and are particular useful when describing the structural parameters for octahedral SCO complexes.[219] ***d***$_{mean}$ corresponds to the average metal-ligand distances in the octahedral coordination sphere and ζ is the total deviation, summed over all metal-ligand interactions, from this average bond distance.[224] Δ is the octahedral distortion parameter that quantifies how the coordination differs in bond lengths from ideal structure ($\Delta = 0$).[225] Σ is the total deviation of the twelve cis angles away from 90°,[226] and Θ represents the degree of trigonal distortion of the coordination geometry from an octahedron (O_h, $\Theta = 60$) towards a trigonal prismatic (D_{3h}, $\Theta = 0$).[227,228] The values of ***d***$_{mean}$, ζ, and Δ for the new structures (**Co^{III}Sln-ampy^{+}** and **Co^{III}Sln-cnpy^{+}**) are very similar to **Co^{III}Sln-py^{+}**. This suggests that the donor strength of the pyridyl ligand has little influence on the coordination geometry. Σ and Θ vary a little bit between structures, which may be the result of crystal packing forces and solvents in the structures but are still consistent with octahedral geometry at the Co centers.

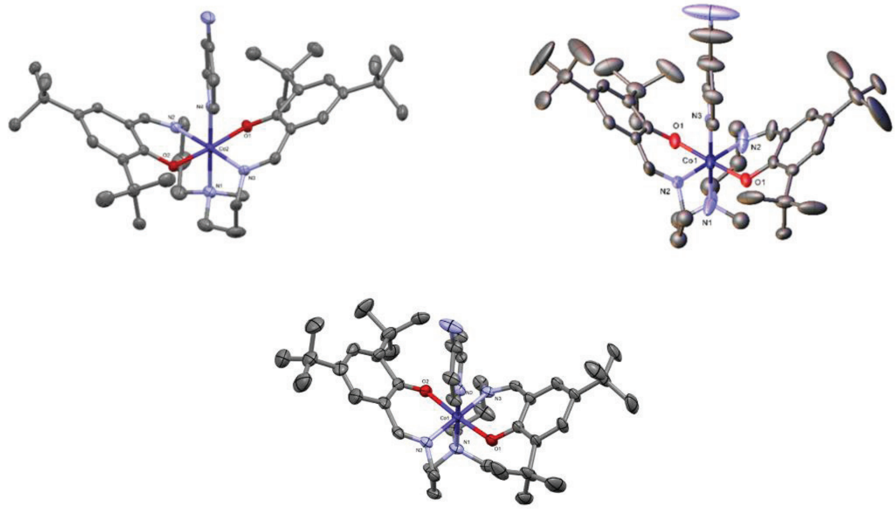

Figure 41: ORTEP diagrams of [CoSln-ampy](SbF_6) (left), [CoSln-cnpy](SbF_6) (right), and [CoSln-ampy](Cl) (bottom center) showing 50% probability thermal ellipsoids. Non-coordinating anions, hydrogens, solvent atoms, and disordered atoms are omitted for clarity.

Table 2: Selected distances and angles, and octahedral structural parameters for [Co^{III}Sln],[a] [Co^{III}Sln](SbF$_6$),[b] [Co^{III}Sln-py](SbF$_6$),[b] [Co^{III}Sln-ampy]Cl, [Co^{III}Sln-ampy](SbF$_6$), and [Co^{III}Sln-cnpy](SbF$_6$) from the X-ray crystallographic analysis.

<table>
<tr><th colspan="7">Bond Distances (Å)</th></tr>
<tr><th></th><th>[Co^{II}Sln] [a]</th><th>[Co^{III}Sln] (SbF$_6$) [b]</th><th>[Co^{III}Sln-py] (SbF$_6$) [b]</th><th>[Co^{III}Sln-ampy] (Cl)</th><th>[Co^{III}Sln-ampy] (SbF$_6$)</th><th>[Co^{III}Sln-cnpy] (SbF$_6$)</th></tr>
<tr><td>Co-O$_{\text{phenol}}$</td><td>1.944(2)</td><td>1.856(2)</td><td>1.919(2)</td><td>1.9299(16)</td><td>1.933(2)</td><td>1.922(3)</td></tr>
<tr><td>Co-O$_{\text{phenol}}$</td><td>1.952(2)</td><td>1.865(2)</td><td>1.920(2)</td><td>1.9120(15)</td><td>1.925(2)</td><td>1.922(3)</td></tr>
<tr><td>Co-N$_{\text{pyridyl}}$</td><td>-</td><td>-</td><td>1.966(2)</td><td>1.974(5)</td><td>1.945(2)</td><td>1.976(4)</td></tr>
<tr><td>Co-N$_{\text{imine}}$</td><td>2.045(2)</td><td>1.906(3)</td><td>1.923(2)</td><td>1.9271(19)</td><td>1.927(2)</td><td>1.904(4)</td></tr>
<tr><td>Co-N$_{\text{imine}}$</td><td>2.054(2)</td><td>1.904(3)</td><td>1.928(3)</td><td>1.9219(19)</td><td>1.921(2)</td><td>1.904(4)</td></tr>
<tr><td>Co-N$_{\text{amine}}$</td><td>2.124(2)</td><td>2.082(3)</td><td>2.065(3)</td><td>2.0589(19)</td><td>2.077(3)</td><td>2.060(6)</td></tr>
<tr><th colspan="7">Bond Angles (deg)</th></tr>
<tr><th></th><th>[Co^{II}Sln] [a]</th><th>[Co^{III}Sln] (SbF$_6$) [b]</th><th>[Co^{III}Sln-py] (SbF$_6$) [b]</th><th>[Co^{III}Sln-ampy] (Cl)</th><th>[Co^{III}Sln-ampy] (SbF$_6$)</th><th>[Co^{III}Sln-cnpy] (SbF$_6$)</th></tr>
<tr><td>O$_{\text{phenol}}$-Co-O$_{\text{phenol}}$</td><td>138.63(8)</td><td>129.39(10)</td><td>177.10(9)</td><td>175.24(7)</td><td>175.62(10)</td><td>176.95(15)</td></tr>
<tr><td>N$_{\text{imine}}$-Co-N$_{\text{imine}}$</td><td>177.11(1)</td><td>178.95(13)</td><td>178.54(11)</td><td>177.11(8)</td><td>176.92(11)</td><td>179.4(2)</td></tr>
<tr><td>N$_{\text{amine}}$-Co-O$_{\text{phenol}}$</td><td>111.71(8)</td><td>115.41(11)</td><td>91.68(9)</td><td>92.75(7)</td><td>92.27(10)</td><td>90.25(13)</td></tr>
<tr><td>N$_{\text{amine}}$-Co-O$_{\text{phenol}}$</td><td>109.67(8)</td><td>115.20(11)</td><td>91.21(9)</td><td>91.05(8)</td><td>92.11(10)</td><td>90.25(13)</td></tr>
<tr><td>N$_{\text{pyridyl}}$-Co-N$_{\text{amine}}$</td><td></td><td></td><td>178.42(11)</td><td>176.1(3)</td><td>179.77(12)</td><td>180</td></tr>
<tr><td>N$_{\text{pyridyl}}$-Co-O$_{\text{phenol}}$</td><td></td><td></td><td>88.87(9)</td><td>86.2(4)</td><td>87.51(9)</td><td>88.47(7)</td></tr>
<tr><td>N$_{\text{pyridyl}}$-Co-O$_{\text{phenol}}$</td><td></td><td></td><td>88.24(9)</td><td>90.1(4)</td><td>88.11(10)</td><td>88.47(7)</td></tr>
<tr><td>N$_{\text{pyridyl}}$-Co-N$_{\text{imine}}$</td><td></td><td></td><td>91.82(11)</td><td>93.3(3)</td><td>91.54(10)</td><td>90.29(12)</td></tr>
<tr><td>N$_{\text{pyridyl}}$-Co-N$_{\text{imine}}$</td><td></td><td></td><td>89.63(11)</td><td>89.1(3)</td><td>91.48(10)</td><td>90.29(12)</td></tr>
<tr><th colspan="7">Octahedral Structural Parameters</th></tr>
<tr><th></th><th>[Co^{II}Sln] [a]</th><th>[Co^{III}Sln] (SbF$_6$) [b]</th><th>[Co^{III}Sln-py] (SbF$_6$) [b]</th><th>[Co^{III}Sln-ampy] (Cl)</th><th>[Co^{III}Sln-ampy] (SbF$_6$)</th><th>[Co^{III}Sln-cnpy] (SbF$_6$)</th></tr>
<tr><td>d_{mean} / Å</td><td></td><td></td><td>1.9536</td><td>1.9538</td><td>1.9545</td><td>1.9484</td></tr>
<tr><td>ζ / Å</td><td></td><td></td><td>0.247366</td><td>0.249301</td><td>0.244452</td><td>0.280594</td></tr>
<tr><td>Δ</td><td></td><td></td><td>0.000719</td><td>0.000673</td><td>0.000798</td><td>0.000821</td></tr>
<tr><td>Σ / °</td><td></td><td></td><td>9.8165</td><td>20.0299</td><td>16.0624</td><td>8.3222</td></tr>
<tr><td>Θ / °</td><td></td><td></td><td>43.8858</td><td>71.6038</td><td>60.7152</td><td>39.1520</td></tr>
<tr><td colspan="7">[a] Data taken from ref [207]. [b] Data taken from ref [125].</td></tr>
</table>

3.5 Electrochemistry

As we have described previously, cyclic voltammograms (CV) of **Co^{II}Sln** in a non-coordinating solvent exhibit a quasi-reversible wave at -0.59 V vs Fc$^{0/+}$ associated with the Co$^{II/III}$ couple. Figure 42 shows the CVs of **Co^{II}Sln** in DCM alone and in the presence of a slight excess of ligands with the highest association constants shown above (**bpy**, **pic**, **ampy**, **im**, **bix**, **ampy**, **dmapy**). Introduction of the exogenous ligands results in a large peak splitting between the anodic and cathodic waves for the Co$^{II/III}$ couple. In general, there is a large negative shift in reduction potential and a slight positive shift of the oxidation potential. For these ligands, addition of 1-1.5 equivalent was sufficient to completely suppress the cathodic wave at -0.6 V for the reversible Co$^{II/III}$ process and produce a new cathodic wave in the range of -0.9 to -1.3 V. The later peak now corresponds to reduction of **Co^{III}Sln-L^{+}**, the potential of which now depends on the nature of the ligand.

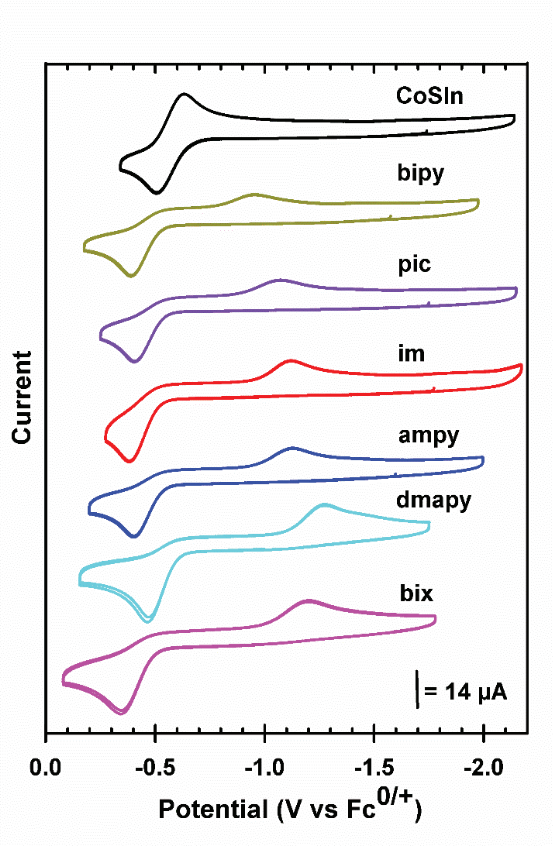

Figure 42: Cyclic voltammograms of CoSln (0.5mM) with 10 equivalents of each ligand, taken at a glassy carbon electrode, with a platinum wire counter, and a silver pseudoreference electrode (referenced to Fc$^{0/+}$ following each titration). All scans began sweeping anodically from -0.7 V at a rate of 500 mV/s. CoSln (black), bpy (gold), pic (purple), im (red), ampy (blue), dmapy (cyan), bix (pink).

The redox properties of **Co^{II}Sln** in the presence of these ligands can be described by the square diagram (ECEC mechanism) shown in Figure 43.[229] The oxidation potential of **Co^{II}Sln** is largely independent of the nature of the L present in solution. Titrations of **Co^{II}Sln** with **dmapy** and **im**, some of the strongest donor ligands examined herein, in DCM confirmed that there is very weak binding interaction between these ligands and the Co^{II} metal center ($K_{a,2+} < 90$ M^{-1}). At the concentrations used in the CVs, the ligands should be largely dissociated from **Co^{II}Sln**, however the slight shift in the Co^{II} oxidation potential (E^o_{hs}) indicates a weak interaction. Upon oxidation to **Co^{III}Sln$^+$**, the large association constants for these ligands ensures almost complete conversion to **Co^{III}Sln-L$^+$**. The reduction potential of **Co^{III}Sln-L$^+$** (E^o_{ls}) is now dependent on the nature of ligand. Complete binding of the ligands to **Co^{III}Sln^{+}** is evident from the suppression of the cathodic wave at -0.59 V, and appearance of a new wave at much more negative potentials.

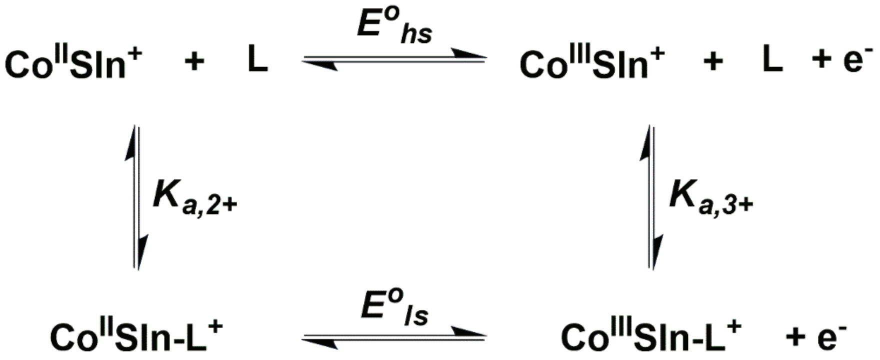

Figure 43: Square scheme of the ligand-dependent RCSCO of this CoSln^{+}.

Figure 44 shows CVs of **Co^{II}Sln** in the presence of three ligands that showed relatively weak association with **Co^{III}Sln^{+}**, **cnpy**, **pyrz**, and **pyrl**, at varying concentrations. In all three of these cases, the weak $K_{a,3+}$ values necessitate addition of a slightly larger excess of ligand to the solution to completely suppress the reduction at -0.59V and shift the cathodic peak to more negative potentials. Additionally, the reduction waves corresponding to **Co^{III}Sln-L^{+}** are much more positive than those shown above in Figure 44. A second quasi-reversible wave appears at -1.7 V which may be due to **cnpy**.

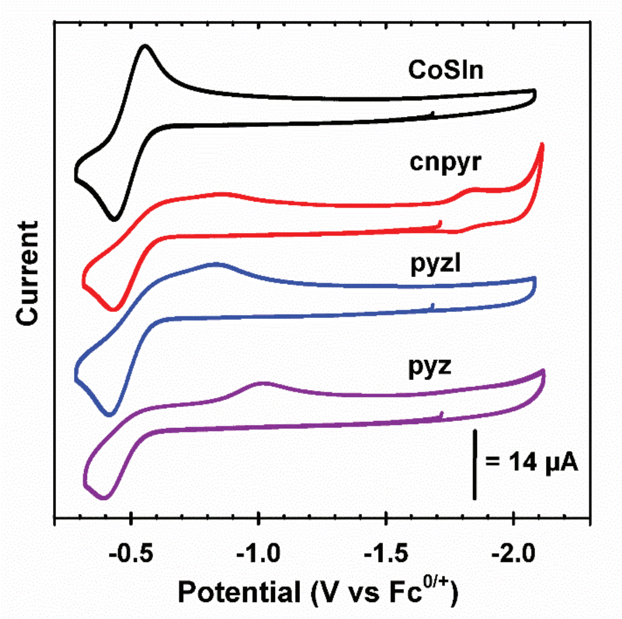

Figure 44: Cyclic voltammograms of CoSln (0.5mM) with different equivalents of each ligand, taken at a glassy carbon electrode, with a platinum wire counter, and a silver pseudoreference electrode (referenced to Fc$^{0/+}$ following each titration). All scans began sweeping anodically from -0.7 V at a rate of 500 mV/s. CoSln (black), cnpyr (red), pyzl (blue), and pyz (purple).

CVs of **Co^{II}Sln** in the presence of **bpy** show some evidence of dimerization (Figure 45). Between 0.5-1 equivalents, the reduction peak for **Co^{III}Sln^{+}** is suppressed due to coordination to the **bpy**, and a new quasi-reversible cathodic wave is observed at -1.5 V. This can be assigned to the reduction of the bridging **bpy** ligand to form **[Co^{III}Sln-(bpy$^{-\cdot}$)-Co^{III}Sln]$^{+}$** based on comparison reduction potential of **bpy** in similar macrocycles where it is bridging two cationic metal centers.[230] Upon addition of excess **bpy** to the electrolyte solution, the ligand acts in a monodentate fashion and only a single reduction is observed for **Co^{III}Sln-bpy^{+}**.

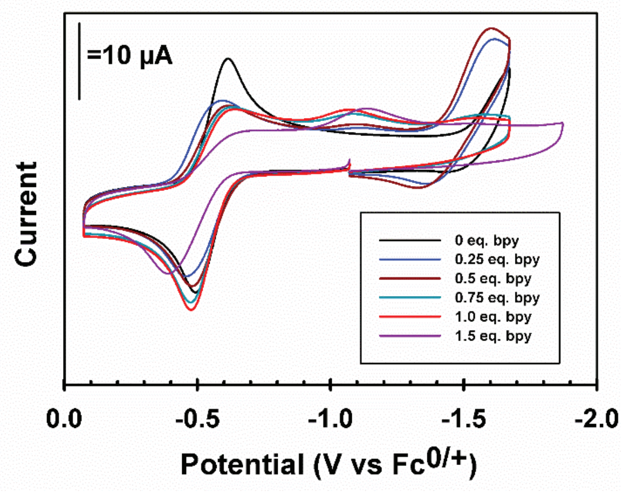

Figure 45: Cyclic voltammograms of CoSln (0.5mM) with a range of concentrations of bpy, taken at a glassy carbon electrode, with a platinum wire counter, and a silver pseudoreference electrode (referenced to Fc$^{0/+}$ following each titration). All scans began sweeping anodically from -1.0 V at a rate of 500 mV/s.

The electrochemistry of **Co^{II}Sln** in the presence of anions, including **OH$^-$**, **Cl$^-$**, and **Br$^-$**, all exhibited interesting behavior as well (Figure 46).The reduction potentials of all three bound complexes, **Co^{III}Sln-L$^+$**, were significantly more negative compared to the complexes formed from the neutral ligands. This is no doubt the result of the influence of the negative charge that is not present in the case of neutral ligands. The electrostatic repulsion of this negative charge required a larger applied bias to regenerate the initial five-coordinate **Co^{II}Sln**.

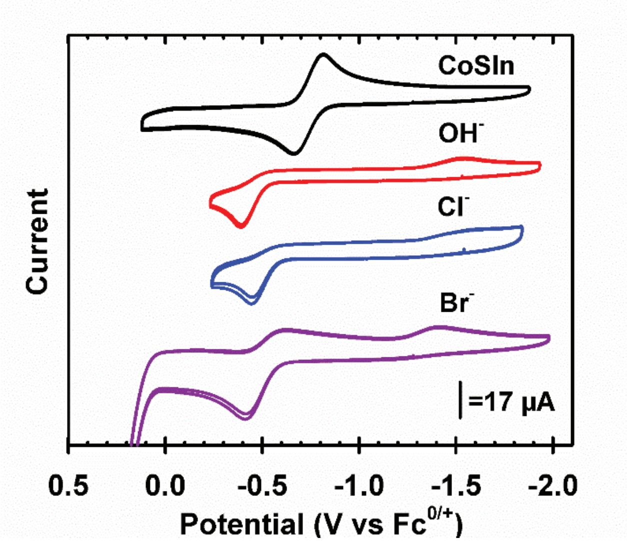

Figure 46: Cyclic voltammograms of CoSln (0.5mM) with ten equivalents of each anion, taken at a glassy carbon electrode, with a platinum wire counter, and a silver pseudoreference electrode (referenced to $Fc^{0/+}$ following each titration). All scans began sweeping anodically from -1.0 V at a rate of 500 mV/s. CoSln (black), OH- (red), Cl- (blue), and Br- (purple).

3.6 Discussion

RCSCO provides a mechanism to design complexes with redox bistability, which could be beneficial for a range of applications. Complexes such as **Co^{II}Sln** provide a platform to tune the RCSCO properties through the choice of exogenous ligands. Scheme 2 shows the square diagram that describes the redox properties of **Co^{II}Sln** in the presence of these different ligands. Given the relatively low ligand association constants of **im** and **dmapy** with **Co^{II}Sln**, it is expected that the oxidation potential of **Co^{II}Sln** will not change significantly in the presence of stoichiometric amount of ligands. However, the reduction potential of **Co^{III}Sln-L^+** does show a significant dependence on the nature of the ligand. It is possible that this shift in the reduction potential is due to ligand interactions with the electrode shifting the half-potential of the $Fc^{0/+}$ reference. For this reason, we have chosen to report both the measured redox potentials and the observed cathodic-anodic peak separation. These values and other data collected in the course of this study are in Table 3.

Table 3: Summary of ligand association constants, Co$^{II/III}$ redox potentials, cathodic-anodic peak splitting, spin exchange constant ratios, Hammett parameters for pyridyl based ligands, and gas phase basicity of ligands (L) bound to CoSln^{+}.

L =	$E^{o}_{red,ls}$ / V [c]	$E^{o}_{ox,hs}$ / V [c]	ΔE V	K_{se}^{2+} / K_{se}^{3+}	σ [d]	GPB (kJ/mol) [e]
pyrzn	-0.83	-0.42	0.41	4.94		847.0
pyrzl	-1.02	-0.40	0.62	11.2		860.5
cnpy	-0.86	-0.43	0.43	5.34	0.66	880.6
py	-1.10	-0.42	0.68	14.1	0.00	898.1
Bpy	-0.95	-0.39	0.56	8.85	0.44	*908.1* [f]
im	-1.12	-0.38	0.74	17.8		909.2
pic	-1.07	-0.40	0.67	13.6	-0.17	915.3
bix	-1.19	-0.34	0.85	27.4		*941.9* [f]
ampy	-1.13	-0.40	0.73	17.2	-0.66	947.8
dmapy	-1.26	-0.47	0.79	21.7	-0.83	971.1
Br-	-1.42	-0.41	1.01	51.1		1331.3
Cl-	-1.62	-0.39	1.23	120		1373.6
OH-	-1.59	-0.44	1.15	88.1		1605.4

Overall, the association constant for a given ligand appears to correlate only weakly with the observed electrochemical properties for the reduction of **Co^{III}Sln-L**$^{+}$. The ligands with the highest association constants (**py**, **pic**, **ampy**, **im**, **bix**, **ampy**, and **dmapy**) generally displayed the most negative reduction potentials with the largest splitting between cathodic and anodic peaks (Table 3), while the weaker ligands led to more positive reduction potentials for **Co^{III}Sln-L**$^{+}$ (Figure 44). This trio of weak ligands were found to require a large excess guest ligand to induce a cathodic shift.

Having observed a range of peak shifts for each ligand, we sought a parameter that would help establish an intuitive framework for understanding the observed behavior and crafting a synthetic guide to serve as a basis for future applied studies. We began by comparing observed reduction potentials to the corresponding Hammett parameters of the para-substituted pyridines. Hammett parameters are readily available in the literature and represent an approximation of the electronic contribution of the *para*-substituent on the aromatic ring.[231] A large positive Hammett parameter denotes a strongly electron withdrawing substituent while a large negative Hammett parameter similarly indicates a strongly electron donating substituent.[232]

Figure 47 shows the cathodic-anodic peak separations **Co^{III}Sln-L^{+}** compared to the Hammett parameters for the *para*-substituted pyridine-based ligand. A linear correlation between the reduction potential of **Co^{III}Sln-L^{+}** and the Hammett parameter of the respective para substituent is seen ($R^2 = 0.87$), indicating that electron donating ability of the ligands has a noticeable impact on the redox properties. **dmapy**, with a strongly electron donating dimethylamine group ($\sigma_p = -0.83$) adds significantly to the electron density towards the Co^{III} metal center, thus inducing a cathodic shift of the **Co^{III}Sln-L^{+}** reduction potential and the largest degree of peak splitting. Conversely, the strongly electron withdrawing group on **cnpy** ($\sigma_p = 0.66$) results in the most positive reduction potential. The pyridyl based ligands examined here allowed for the tuning of the anodic-cathodic peak separation for the **Co^{III}Sln-L^{+}** system, and thus the redox bistability, over ~300 mV. However, despite the attractiveness of using these Hammett parameters to understand the redox properties of **Co^{III}Sln-L^{+}**, they can only be applied to this homologous series of pyridyl-based ligands.

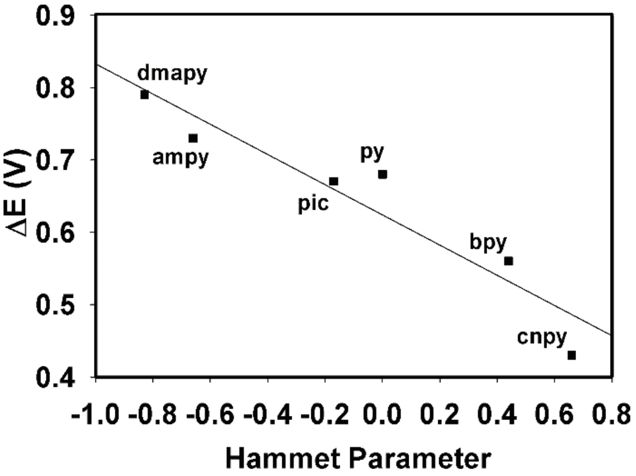

Figure 47: Anodic-Cathodic peak splitting in Co^{III}Sln-L^{+} compared to the Hammett parameters for the para-substituted pyridine derivative.

The sheer quantity of non-pyridine-based ligands available makes it clear that another more universal metric would be better suited to this analysis. Guest ligand basicity has been used to compare the effects of pyridine and cyanopyridine on the SCO properties of a group of nickel (II) complexes.[183] The primary advantage of using basicity to compare guest ligands is that the ligands under investigation do not need to be homologous. We chose to utilize gas phase basicity (GPB), which measures the Gibbs free energy change associated with protonation, as the ligand thermodynamic parameter to evaluate the **Co^{III}Sln-L^{+}** reduction potentials. These values are readily available via NIST databases[233] or other literature sources. Experimental GPB values for all the ligands examined here, except **bix** and **bpy**, are included in

Table 3. The reported GPB for **bpy** of 900 ± 10 kJ/mol was an estimate, suggesting the value was similar to **py**.[234] Following established density functional theory (DFT) methods (PBE1PBE/6-311+G**), which have been shown to yield reasonable estimates for GPB,[220] we have calculated values of 941.9 and 908.1 kJ/mol for **bix** and **bpy** respectively.

Figure 48 shows the anodic-cathodic peak separations of **Co^{III}Sln-L^{+}** compared to the GPB of the different ligands examined. Overall, an increase in the GPB of **L** yields a more cathodic reduction potential for **Co^{III}Sln-L^{+}**. There is a clear correlation for the neutral ligands as indicated by the linear regression (solid black line). This trend indicates that GPB values represent a good metric for the donor strength of the nitrogen-based heterocycles. The three anionic ligands (red points) produce the largest cathodic shift in the **Co^{III}Sln-L^{+}** reduction potential and are noticeably different from the other nitrogen-based heterocycles likely due to their negative charge.

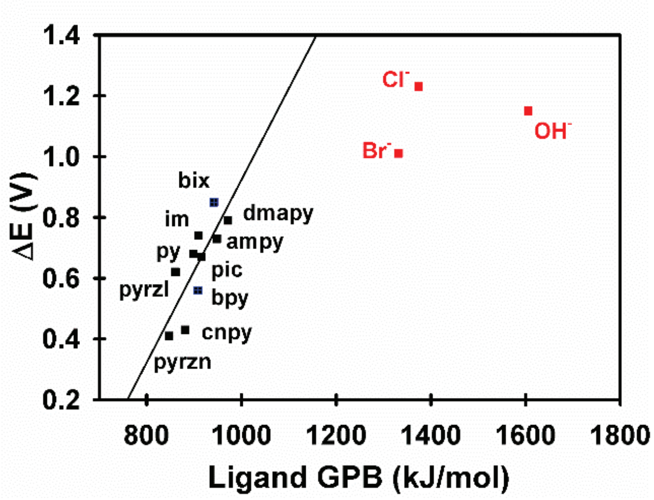

Figure 48: Cathodic-anodic peak splitting in $Co^{III}Sln\text{-}L^+$ compared to the GPB (kJ/mol) of the free ligand (L). Black (neutral ligands) and red (anionic) GPB sourced from NIST database,[233] while the blue (bix and bpy) were estimated from DFT methods (PBE1PBE/6-311+G).[220]**

The selection of neutral ligands examined here are able to modulate the cathodic redox potential of **$Co^{III}Sln\text{-}L^+$** (E^o_{ls}) by ~300mV. When the anionic ligands are included, this potential range is increased to ~800 mV. This in turn provides a mechanism to tune the redox bistability for **$Co^{III}Sln\text{-}L^+$**. The difference in potential between the anodic and cathodic redox waves for the $Co^{III/II}$ process ($E^o_{hs} – E^o_{ls}$) can be used to estimate the ratio of spin equilibrium constants for the two redox states, $K_{se,2+}$ / $K_{se,3+}$. These equilibrium constants define the formation of the hs form for the respective redox states. $K_{se,2+}$ for **$Co^{II}Sln$** should be largely independent of the L present in solution due to the weak interactions. However, $K_{se,3+}$ will strongly depend on the nature of the ligand for **$Co^{III}Sln\text{-}L^+$** and will contain contributions from K_a for each L. The ratio, $K_{se,2+}$ / $K_{se,3+}$, will provide another measure of the bistability of this complex. The estimated values are included in

Table 3 and range from 4.94 (**pyrzn**) to 21.7 (**dmapy**) for the neutral ligands, and up to 120 for **Cl⁻**. The broad range of $K_{se,2+}$ / $K_{se,3+}$ ratios generated by this series of ligands with **$Co^{III}Sln\text{-}L^+$** highlights the ability to tune the RCSCO properties of a complex through coordination changes with exogenous ligands.

3.7 Conclusion

Spin-crossover behavior in coordination compounds has attracted a great deal of interest from researchers for its potential applications in electronic and electrooptical applications, including electrochromics, displays, sensors, data storage devices, and computer processing, among others. One way to enhance the bistability of spin-crossover systems is to couple the spin-transition to redox changes in a coordination complex. We have successfully demonstrated that the RCSCO properties of $\mathbf{Co^{III}Sln^{+}}$ can be reliably and predictably tuned via titration with a range of ligands. Reversible ligand binding as a method to inducing spin-crossover is an uncommon stimulus in the field of spin-crossover research. Cyclic voltammograms of $\mathbf{Co^{III}Sln^{+}}$ in the presence of suitable ligands lead to significant anodic-cathodic peak splitting of the $Co^{III/II}$ redox transition due to the coupled ligand binding and SCO steps. This quasi-reversible electrochemistry results in a range of redox bistability for the complex. We have shown that there is a strong correlation between the reduction potential of the low-spin $\mathbf{Co^{III}Sln\text{-}L^{+}}$ (E^{o}_{ls}) with the Hammett parameter for para-substituted pyridyl ligands and the GPB for a wider variety of ligand types. This allows us to predictably tune the RCSCO properties of the complex and is an important step towards a priori design of SCO materials using uncommon stimuli.

3.8 Acknowledgements

This work was supported by the National Science Foundation under contract CHE-1905064. C.A.M. acknowledge a Slezak Memorial Fellowship from Rensselaer Polytechnic Institute. The National Science Foundation is also acknowledged for support of the acquisition of an X-ray diffractometer (Award Number 2117596) through the Major Research Instrumentation program, as well as Dr. Peter J. Bonitatibus who obtained the X-ray structures included in this chapter. Dr. Peter H. Dinolfo contributed edits, conceptualization, and DFT calculations. Andrea

Mitchell performed solution titrations of **Co^{II}Sln** and contributed parts of the relevant results section.

4. REDOX-COUPLED SPIN CROSSOVER IN A PAIR OF COBALT β-DIKETONATE COMPLEXES AND THEIR POTENTIAL UTILITY IN ELECTROCHROMIC MULTILAYERS

4.1 Spin States of Cobalt β-diketonate Complexes

If there is a classic ligand in inorganic coordination complexes, β-diketonates may well be it. The most common example of which is acetyleacetone, a molecule found in introductory organic and inorganic courses alike. This interest is due to the unique ketol-enol tautomerism that has been observed in these molecules and is depicted in Figure 49. This tautomerism is solvent-dependent and the enol form can be favored replacing the R groups with more electron-withdrawing substituents. The extensive electron delocalization results in multiple coordinative bonding modes. The most commonly depicted is the O,O' bidentate arrangement but others are possible including coordination to just one enolate oxygen or coordination through delocalized carbon double bonds, or even with the β-diketonate serving as a bridge between two metal centers.[235]

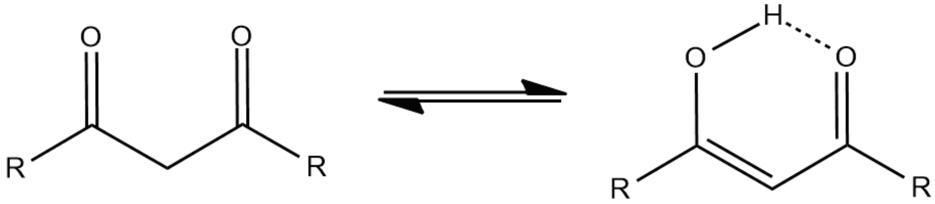

Figure 49: Ketol-enol tautomerism in a β-diketonate.

The electrochemical properties of β-diketonate complexes have likewise long been studied. Irreversible electrochemistry which may be indicative of RCSCO has been observed in transition metal β-diketonate complexes,[236] and tris(β-diketonate)cobalt(III) complexes have shown evidence of RCSCO switching between S=0 state in the cobalt(III) and S=3/2 in the case of the cobalt(II) complex.[237]

A recent interesting example of this are the β-diketonate cobalt(II) complexes reported by Harding in 2012. These cobalt(II) complexes, shown in Figure 50, feature mixed coordination environments consisting of either 2,2'-bipyridine or 1,10-phenanthroline coordinated to the cobalt center opposite a pair of β-diketonate derivatives featuring tert-butyl, benzyl, and trifluro substituents.

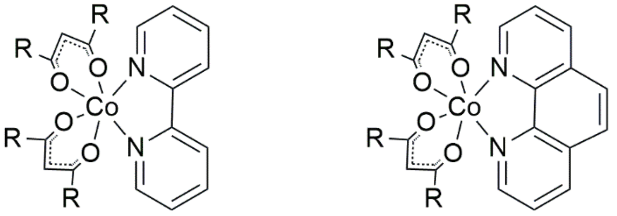

R = $-C(CH_3)_3$, $-CF_3$, $-C_6H_5$,

Figure 50: β-diketonates reported by Harding and co-workers. Generic structures adapted from the original publication.[79]

All six of these chelated tris-bidentate complexes displayed RCSCO as signified by irreversible cyclic voltammograms. Large structural differences were observed between the high-spin (S=3/2) cobalt(II) and low-spin (S=0) cobalt(III) forms of these β-diketonates. X-ray crystal structures of one complex (Figure 51) indicated that large structural changes accompany the RCSCO rearrangement especially in the orientation of the 2,2'-bipyridine ligand, which is notable twisted in the cobalt(II) complex, but assumes a planar arrangement following oxidation of the cobalt(II) metal center to cobalt(III). This was quantified through the Σ parameter which measured the sum of deviations in cis bond angles from idealized geometries. This is a common metric by which SCO complexes are evaluated. A Σ of 0 corresponds to an ideal octahedral geometry in which each bond forms a 90° angle. High-spin complexes typically have a higher Σ value than their low-spin counterparts.[48] By this metric the cobalt(II) high-spin complex was assigned a Σ value of 86, and the oxidized low-spin variant of the same complex was given a Σ value of 34 with an overall Δ Σ of 52. The metal-ligand bonds also shorten by 0.18-0.22 Å following oxidation.

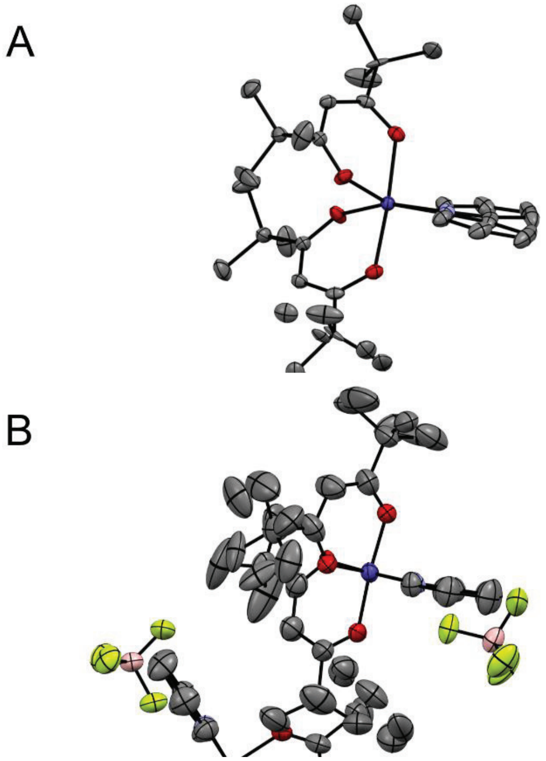

Figure 51: X-ray Structures of two diketonates reported by Harding (A) [Co(tmhd)2(2,2'-bpy)] (B) [Co(tmhd)2(2,2'-bpy)][BF_4]. Hydrogens have been omitted for clarity. Figure generated from published crystallographic data.[238,239]

The complexes showed differences in oxidation and reduction potentials which were attributed to the different β-diketonate ligands used in these complexes. DFT calculations explained these results, showing that the singularly occupied molecular orbital originated from the combination of β-diketonate oxygen p-orbitals and the cobalt d_z^2 orbital resulting in significant electron density on the β-diketonate oxygens. This high electron density on the β-diketonate ligands explains the ligand-dependent electrochemistry and provides a useful "handle" for modulating electrochemical properties. Moreover, significant spectral differences were observed between the cobalt(II) and cobalt(III) states. Generally, the high-spin cobalt(II) complexes were all shades of red or orange and underwent a bathochromic shift following oxidation to the low-spin cobalt(III) state in which most of the complexes were various shades of green.[79]

The electrochemical irreversibility of these complexes and the noted spectral changes that accompany their redox reactions make them interesting candidates for molecular electrochromics. From these observations a hypothesis was formed that these molecules could be used to construct functional electrochromic multilayers using the CuAAC LbL methods our laboratory has employed in this past. In order to test this ethynyl-functionalized bipyridyl ligands were first synthesized and used to assemble two cobalt(II) complexes, one with acetylacetonate ligands and the other with 1,2-diphenylpropane-1,3-dione. These complexes were then characterized through spectroscopic and electrochemical studies. Attempts were then made to construct electrochromic multilayers using both of these complexes.

4.2 Synthesis of Complexes and Precursor Ligands

4.2.1 Synthesis of 5,5’-dibromo-2,2’-bipyrdine

The synthesis of starting material 5,5’-dibromo-2,2’-bipyridine was synthesized according to literature methods[240] and is depicted in Figure 52. The exception to this is that in cases where mono-brominated 2,2’-bipyridine appeared to be the major product the material was reacted for an additional three days to achieve the dibromoniated product in acceptable yields. This was done by first stirring 5 g (0.032 mol) of 2,2’-bipyridine in methanol with 10.8 mL (0.095 mol) of 48% v/v hydrobromic acid for two hours to yield the protonated intermediate. Protonated 2,2’-bipyridine was then added to a pressure flask together with 2.15 mL (0.083 mol) bromine and was stirred at 185°C for three days.

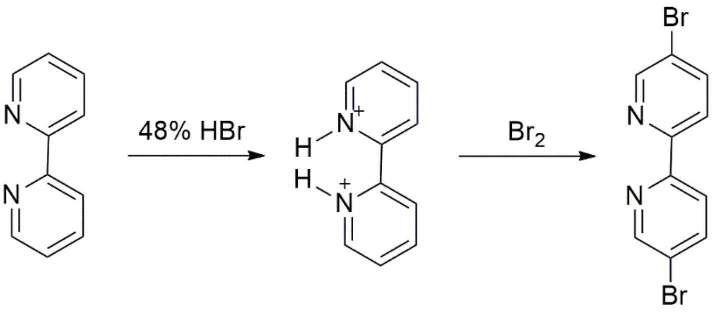

Figure 52: Synthetic scheme for 5,5'-dibromo-2,2'-bipyridine.

This crude mixture was then dissolved in hot dichloromethane and recrystallized, filtered, washed with an aqueous sodium hydroxide solution, and then with water. Mass spectrometry of the product (Figure 53) showed the expected pseudomolecular ion peak at m/z=314.8934 as well as a peak at m/z=417.8417 which appears to contain the protonated product clustered with water and dichloromethane. The peak at m/z=432.2388 does not match the expected tribromo side-product which would have appeared at m/z=375.7972. It is possible that these impurities were introduced during sample handling. A fourth large peak is visible at m/z= 690.7065, which appears to be heavily halogenated and may be a cluster or bromine and solvent molecules. After examining this mass spectrum, the solid was recrystallized once again from dichloromethane giving an overall yield of 16%. Proton NMR (Figure 54) of the recrystallized product showed the expected spectrum for 5,5'-dibromo-2,2'-bipyridine without any contaminants except for the presence of a water peak at 1.56 ppm. ^{1}H NMR Spectrum (500 MHz, $CDCl_3$), ppm: 7.94 (dd, J = 8.95, 2.12 Hz, 2H), 8.28 (d, J = 9.0 Hz, 2H), 8.7 (s, 2H). ESI LR-MS: m/z $C_{10}H_6Br_2N_2$ 313.89, found $[MH]^+$ 314.8934; $[HBr_2bpy, H_2O, CH_2Cl_2]^+$ = 417.8417 , m/z = 432.2383, m/z = 690.7065.

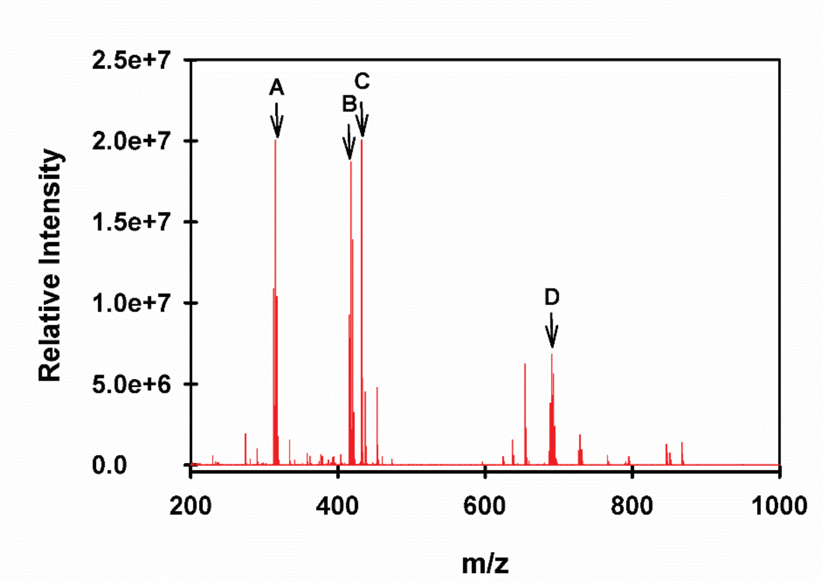

Figure 53: ESI mass spectrum of crude product consisting of 5,5'-dibromo-2,2'-bipyridine (A), 5,5'-dibromo-2,2'-bipyridinewith clustered water and dichloromethane (B), unspecified contaminant (C), halogenated contaminant (D) .

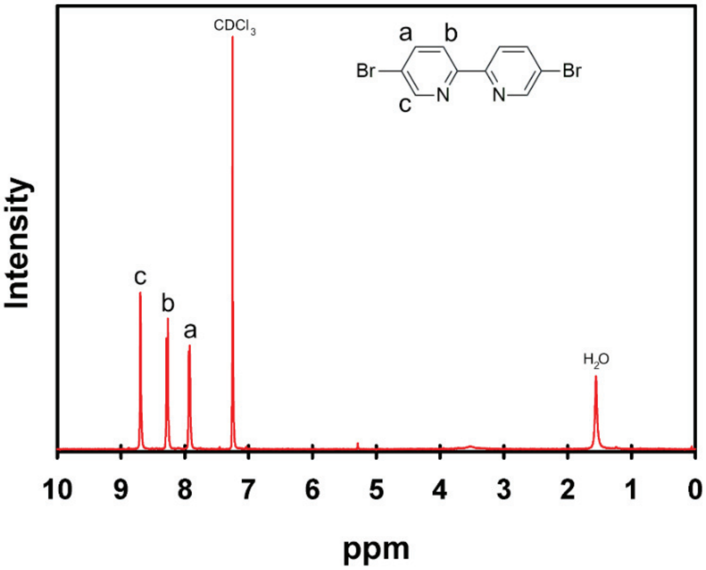

Figure 54: Proton NMR of 5,5'-dibromo-2,2'-bipyridine in deuterated chloroform.

4.2.2 Synthesis of 5,5’-((bistrimethylsilyl)ethynyl)-2,2’-bipyrdine

The synthesis of 5,5'-((bistrimethylsilyl)ethynyl)-2,2'-bipyridine is depicted in Figure 55. 1.6 g (0.005 mol) of 5,5’-dibromo-2,2’-bipyridine was dissolved in dry degassed tetrahydrofuran under a nitrogen atmosphere. 179 mg of $PdCl_3(PPh_3)$ (0.00026 mol), 67 mg (0.00026 mol) of PPh_3, 1.5 mL (0.011 mol) of ethynyltrimethysilane, and 1.5 mL of (0.011 mol)triethylamine was then added and the mixture was stirred for twenty minutes at room temperature before the addition of 50 mg (0.00026 mol) of CuI. The mixture was then left to stir at room temperature for one week.

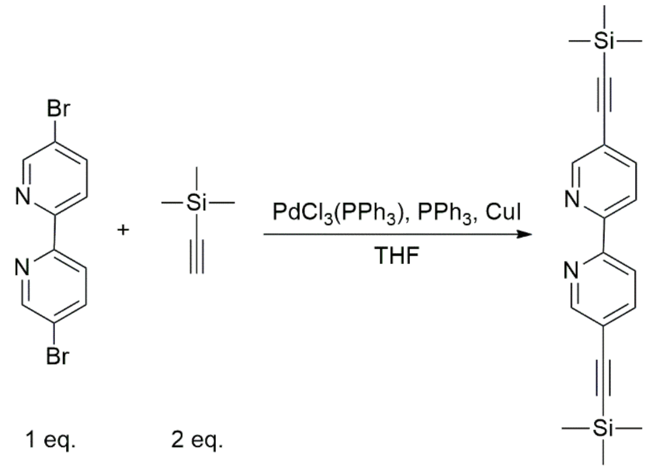

Figure 55: Synthetic scheme for 5,5'-((bistrimethylsilyl)ethynyl)-2,2'-bipyridine.

This mixture was then removed from the nitrogen atmosphere and filtered through celite and the celite was then rinsed with additional solvent. THF was removed via rotary evaporation to give a red solid presumed to be a palladium complex of 5,5’-((bistrimethylsilyl)ethynyl)-2,2’-bipyridine. Palladium was then removed from the complex by stirring overnight in a solution of 0.8 g (0.016 mol) of sodium cyanide dissolved in ethanol. This sample was then purified using dry column vacuum chromatography[241] using successive solvent mixtures dichloromethane and hexane combined in ratios of 40:60, 50:50, 60:40 and poured through in a series of five fractions each followed by final fraction of pure dichloromethane. The proton NMR spectrum (Figure 56) indicates possible contamination with the n-hexane used in the purification process at 0.88 and 1.26 ppm,[242] but the presence of the tetramethyl silane protons without the presence of a peak attributable to the ethynyl proton in ethynyltrimethylsilane around 2.8 ppm confirms that the silane peak is from the product and not residual starting material. Lack of ethynyl carbon peaks near 90 ppm in the ^{13}C NMR spectrum (Figure 57) further confirms the lack of starting material.[243] The yield of this reaction was 25%. ^{1}H NMR spectrum (500MHz, $CDCl_3$), ppm: 0.28 (s, 9H), 7.91 (d, J= 8.5, 2H), 8.44 (d, J=7.6, 2H), 8.75 (s, 2H). ^{13}C NMR spectrum ($CDCl_3$), ppm: 0.19 (s, 6C), 99.5 (s, 2C), 102 (s, 2C), 120 (s, 2C), 120.5 (s, 2C), 140 (s, 2C), 152 (s, 2C), 154 (s, 2C).

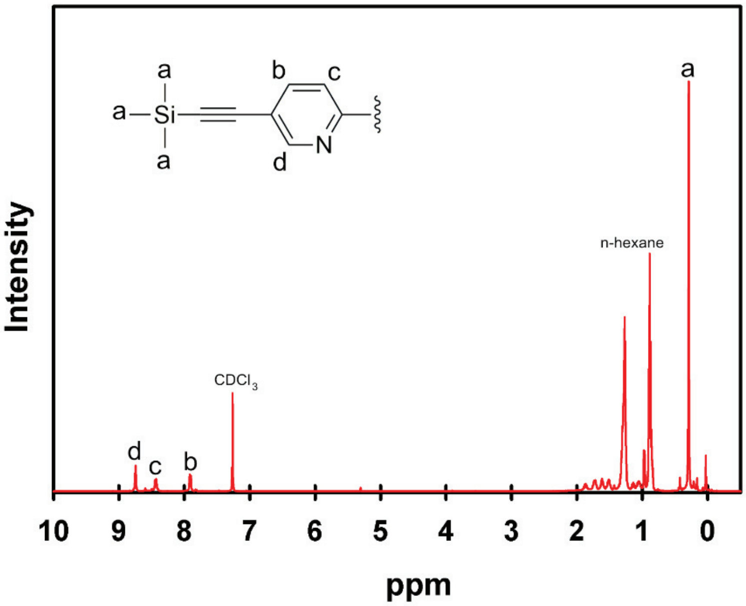

Figure 56: ^{1}H NMR of 5,5’-((bistrimethylsilyl)ethynyl)-2,2’-bipyridine in deuterated chloroform.

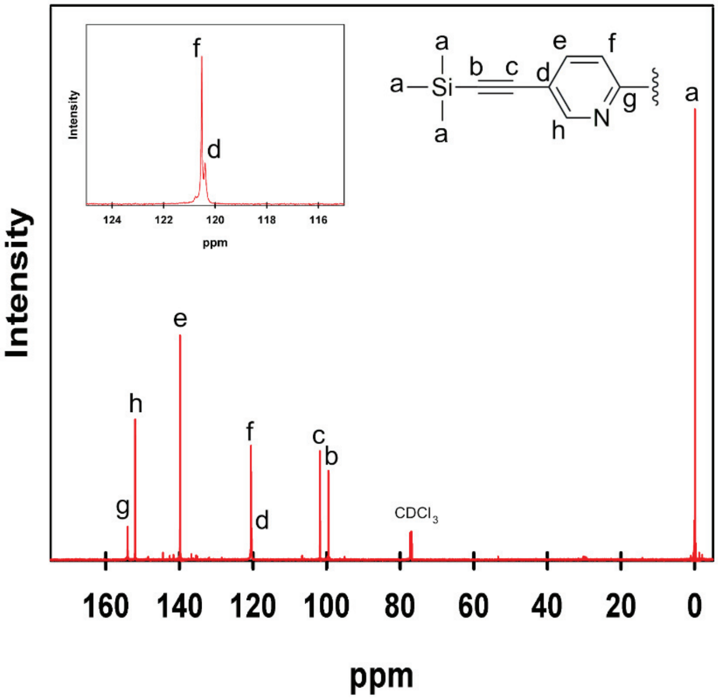

Figure 57: ^{13}C NMR of 5,5'-((bistrimethylsilyl)ethynyl)-2,2'-bipyridine in deuterated chloroform.

4.2.3 Synthesis of Co(acac)$_2$(5,5'-ethynyl-2,2'-bipyridine) complex

The precursor complex [Co(acac)$_2$(OH$_2$)] was first prepared by deprotonating two equivalents of aceytylacetone (acac) using sodium hydroxide in methanol and adding the solution to dissolved solution of cobalt(II)chloride heptahydrate. The resulting pink complex was collected as it precipitated out of solution. 84.7 mg (0.00029 mol) of complex was then combined with 100 mg (0.00029 mol) of 5,5'-((bistrimethylsilyl)ethynyl)-2,2'-bipyridine in methanol and stirred for four hours to give **[Co(acac)$_2$((CC)$_2$bpy)]** as depicted in Figure 58.

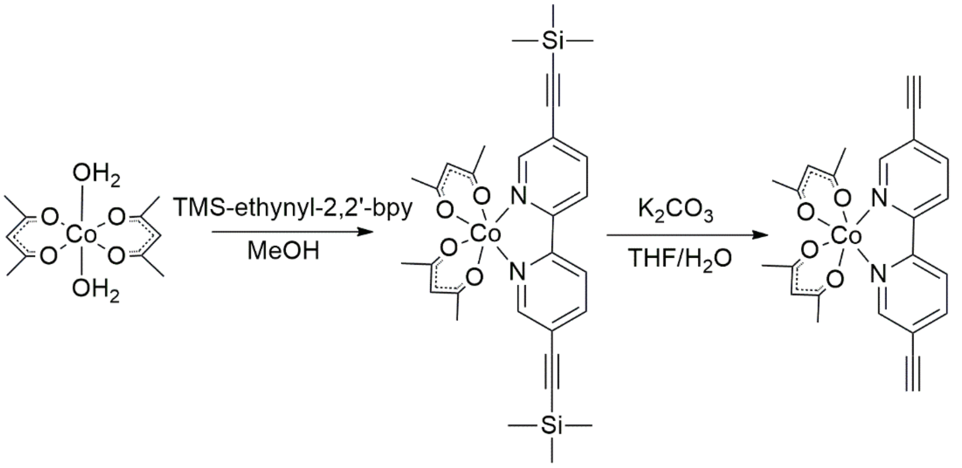

Figure 58: Synthesis of Co(acac)2(5,5'-ethynyl-2,2'-bipyrdine).

The solid was then isolated by filtration and combined with 2.5 equivalents of potassium carbonate in a THF water mixture and stirred overnight to remove the trimethylsilyl protecting groups. The reddish pink solid was then washed on a vacuum filter with ethanol and water, then recrystallized from methylene chloride and hexane in the freezer overnight to give a yield of 47%. ESI LR-MS: m/z $[(CC)_2\text{-bpy}]^+$ calculated 204.07, found $[MH]^+$ 205.0766; m/z $[Co(acac)((CC)_2bpy)]^+$ calculated 362.05, found 362.0354; m/z $[Co(acac)_2((CC)_2bpy)]^+$ calculated 461.09, found 462.0915. UV-Vis spectrum (C_2H_3N), nm: 190, 269, 286, 311, 324.

4.2.4 Synthesis of Co(dbm)$_2$(5,5'-ethynyl-2,2'-bipyridine)

The precursor complex $[Co(dbm)_2(OH_2)]$ was prepared by deprotonating 500 mg (0.002 mol) of 1,2-diphenylpropane-1,3-dione (dbm) using 89 mg (0.002 mol) sodium hydroxide in methanol. 265.3 mg (0.001 mol) of cobalt(II) chloride heptahydrate was then dissolved in methanol and added to solution. The resulting complex, cobalt(II)bisacetylacetonate dihydrate, was collected as it precipitated out of solution. 155 mg (0.00029 mol) of cobalt(II)bisacetylacetonate dihydrate was then combined with 100 mg (0.00029 mol) of 5,5'-((bistrimethylsilyl)ethynyl)-2,2'-bipyridine in methanol and stirred for four hours to give

[Co(dbm)$_2$((CC)$_2$bpy)] as depicted in Figure 59.

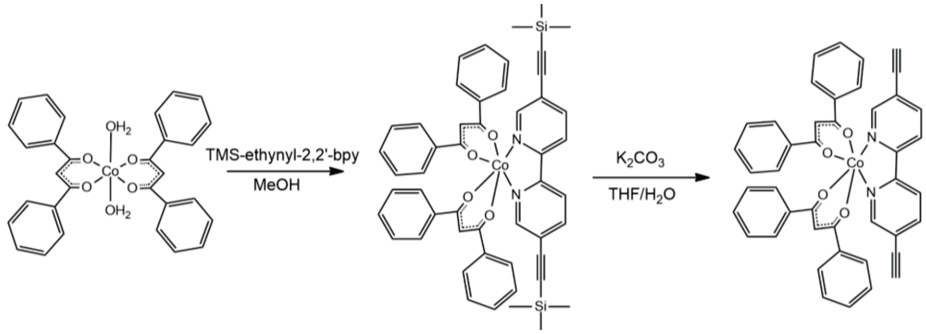

Figure 59: Synthesis of Co(dbm)$_2$(5,5-ethynyl-2,2'-bipyridine).

The solid was then isolated and combined with 2.5 equivalents of potassium carbonate in a THF water mixture and stirred overnight to remove the trimethylsilyl protecting groups. The reddish pink solid was then washed on a vacuum filter with ethanol and water, then recrystallized from methylene chloride and cyclohexane in the freezer overnight to give a yield of 54%. ESI LR-MS: m/z [(CC)$_2$-bpy]$^+$ calculated 204.07, found [MH]$^+$ 205.0766; m/z [Co(dbm)((CC)$_2$bpy]$^+$ calculated 486.08, found 486.0782; m/z [Co(dbm)$_2$((CC)$_2$bpy]$^+$calculated 709.15, found 709.1516. UV-Vis spectrum (C_2H_3N), nm: 190, 275, 337.

4.2.5 Electrochemistry

Solution electrochemistry was carried out using acetonitrile or methylene chloride as a solvent in a three-electrode cell. Solvents were dried over molecular sieves and degassed with nitrogen prior to use and tetrabutylammonium hexaflurophosphate was added to the solvents as an electrolyte at a concentration of 0.1 M. All electrochemistry was carried out with a constant stream of nitrogen to maintain an inert atmosphere. In all cases the working electrode was glassy carbon, the counter electrode was a platinum wire, and a silver wire was used as a pseudo-reference electrode. All scans were then reference to the ferrocene/ferrocenium (Fc$^{0/+}$) redox couple.[244]

4.2.6 Chemical Oxidations

Chemical oxidations were carried out in dry degassed acetonitrile using nitrosonium hexaflurophosphate. Nitrosonium hexfluorophosphate stock solution was prepared in an inert nitrogen atmosphere with a concentration of approximately 14.8 mM. Additions of 100 uL were then made to cuvettes containing **[Co(dbm)$_2$((CC)$_2$bpy)]** (0.2 mM) and **[Co(acac)$_2$((CC)$_2$bpy)]** (0.064 mM) until the samples were completely oxidized as evidenced by the UV-Vis spectra.

4.3 Characterization of β-diketonate complexes

4.3.1 Mass Spectrometry of Complexes

Mass spectrometry of both complexes are as expected and consistent with the results reported by Harding. The β-diketonate ligands appear to be fairly labile and, in both complexes, significant dissociation appears to take place during the ionization process.

In the case of **[Co(acac)$_2$((CC)$_2$bpy)]**(Figure 60) specifically there are three peaks of immediate importance in the mass spectrum corresponding to protonated free bipyridine ligand at m/z = 205.0766, the complex minus one acac ligand at m/z = 362.0454, and a comparitively smaller peak attributed to the intact complex at m/z = 461.0915.

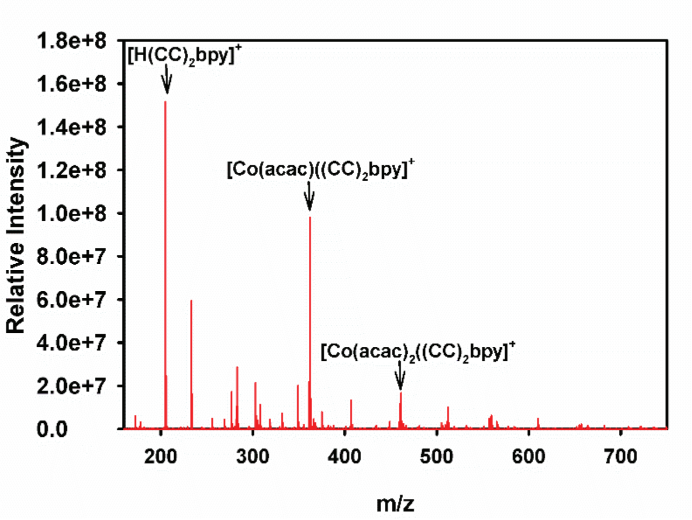

Figure 60: ESI mass spectrum of Co(acac)$_2$((CC)$_2$bpy).

In the mass spectrum of **[Co(dbm)$_2$((CC)$_2$bpy)]** (Figure 61) there is evidence for a protonated CC$_2$-bipyrdine ligand at m/z=205.0761 and another peak corresponding to the loss of a β-diketonate ligand [Co(acac)((CC)2bpy)]$^+$ at m/z = 486.0782. The expected major peak for the molecular ion [Co(dbm)$_2$((CC)$_2$bpy)]$^+$ at m/z = 709.1516 corresponding to the molecular ion is present but is minor compared to the other peaks.

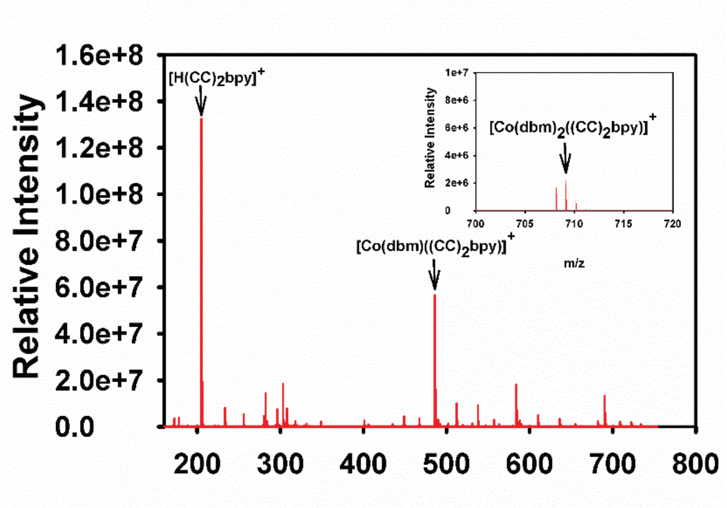

Figure 61: ESI mass spectrum of Co(dbm)$_2$((CC)$_2$bpy).

4.3.2 Electronic Absorption Spectra of [Co(acac)$_2$((CC)$_2$bpy)] and [Co(dbm)$_2$((CC)$_2$bpy)]

The electronic spectra of the two complexes appears to be heavily dependent on the nature of the β-diketonate ligands. The spectrum of [**Co(acac)$_2$((CC)$_2$bpy)]** complex in Figure 62 shows a strong absorbance at 311 nm with buried smaller peaks at 269 nm, 286 nm, and 324 nm that result in a broad absorbance around 300 nm. Strong absorbance is also seen in the far-UV at 200 nm and below. Upon oxidation the spectrum changes drastically and splits into two major peaks in the near-UV at 273 nm and 336 nm. Absorbance of the complex at 244 nm and below also increased drastically. This is similar to a related complex [Co(tmhd)$_2$(bpy)] reported by Harding which featured β-diketonate ligands with trimethyl groups at the R positions and showed a major peak at 284 nm which converted to three major peaks at 236 nm, 298 nm, and 342 nm after oxidation.

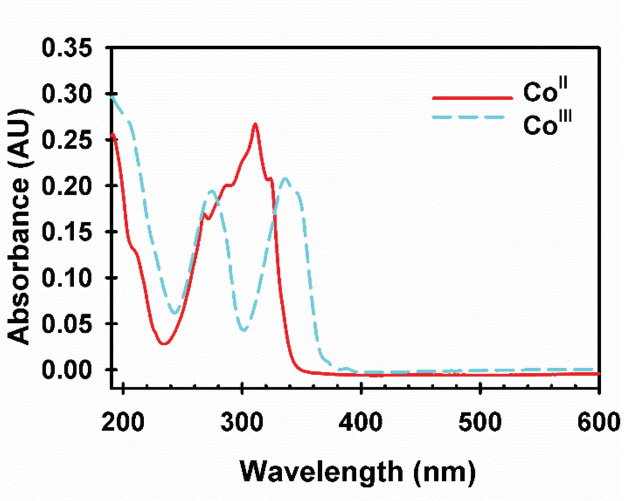

Figure 62: Absorbance spectra of 0.064 mM [Co(acac)$_2$((CC)$_2$bpy)] in acetonitrile in reduced (solid red) and oxidized (dotted blue) states.

The spectrum of **[Co(dbm)$_2$((CC)$_2$bpy)]**, seen in Figure 63, is considerably different with major peaks at 251 nm and 322 nm with a broad shoulder around 350 nm. Like **[Co(acac)$_2$((CC)$_2$bpy)]** there is an intense absorbance in the far UV near 200 nm but unlike

[Co(acac)$_2$((CC)$_2$bpy)] the sharp increase in absorbance upon oxidation is not seen in this region. Upon oxidation the peaks at 251 nm and 322 nm shift with new major peaks seen at 275 nm and 337 nm. Notably, the intensity of the 337 nm is much greater than that of the 322 nm peak. This behavior is promising for an electrochromic requiring a high degree of contrast been the transmission intensities of the on and off states. Strong absorbance is seen in the far-UV here as well but the changes in absorbance of this region following oxidation are less notable. Again, the spectra changes caused by oxidation are similar to the analogous dbm-containing complex reported by Harding with initial peaks at 247 nm and 350 nm and peaks at 230 nm, 292 nm, and 388 nm.

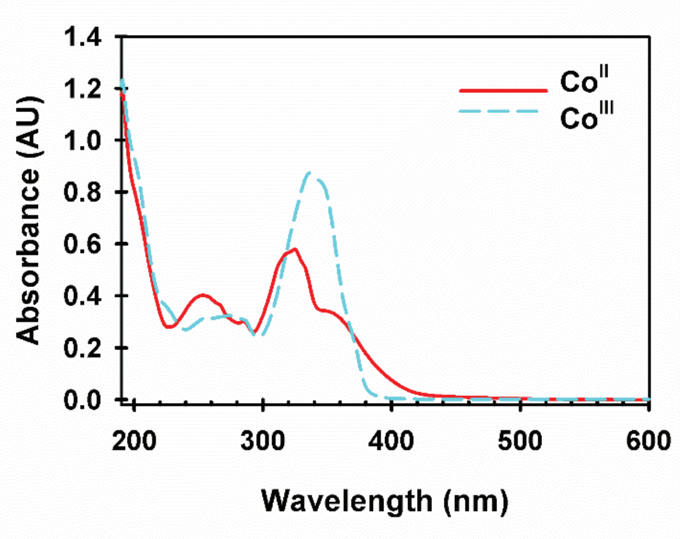

Figure 63: Absorbance spectra of 0.2 mM [Co(dbm)$_2$((CC)$_2$bpy)] in acetonitrile in reduced (solid red) and oxidized (dotted blue) states.

4.3.3 Electrochemistry of [Co(acac)$_2$((CC)$_2$bpy)] and [Co(dbm)$_2$((CC)$_2$bpy)]

Both β-diketonates display irreversible electrochemistry in both acetonitrile and dichloromethane consistent with the results previously reported by Harding. This electrochemistry shows a clear dependence on the nature of the β-diketonate ligand and peak separation is much larger in the case of the dbm complex.

A cyclic voltammogram of **[Co(acac)$_2$((CC)$_2$bpy)]** taken in acetonitrile at a scan rate of 100 mV/s is shown in Figure 64. This voltammogram displays an oxidation wave at 0.14V vs Fc$^{0/+}$ and a reduction wave at -0.34 V vs Fc$^{0/+}$ with a peak splitting of 346 mV when examined at a scan rate of 100 mV/s. Minor waves can be seen at 0.03 V and -0.15 V vs Fc$^{0/+}$. Scan rate dependence (Figure 65) shows a linear relationship between peak current and the square root of the scan rate for the peaks at 0.14V vs Fc$^{0/+}$, -0.34 V vs Fc$^{0/+}$, and -0.15 V vs Fc$^{0/+}$ are linear (Figure 66), consistent with a solution phase species.[65]

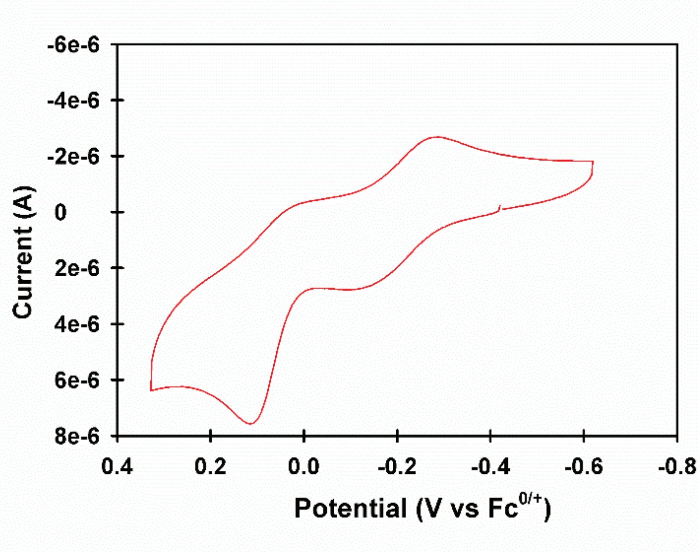

Figure 64: Cyclic voltammogram of Co(acac)$_2$(bpy) in acetonitrile with 0.1M concentration of supporting electrolyte taken at a glassy carbon electrode with a scan rate of 100 mV/s.

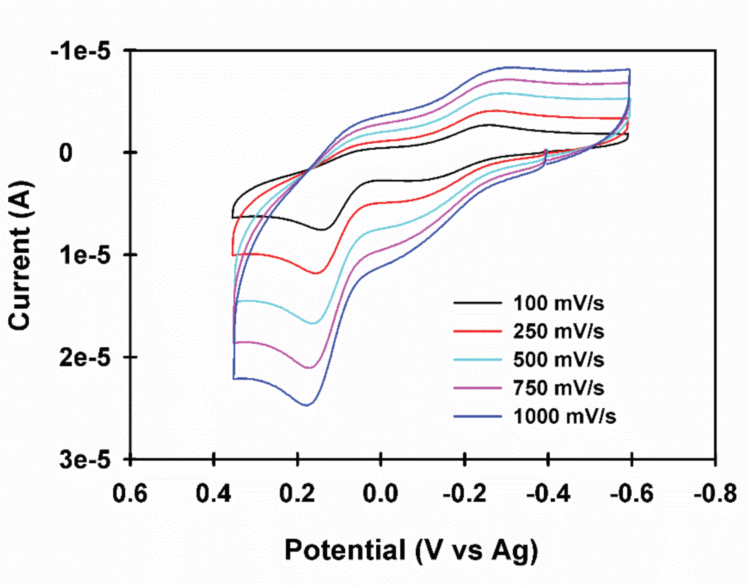

Figure 65: Cyclic voltammograms of [Co(acac)$_2$((CC)$_2$bpy)] taken at multiple scan rates in acetonitrile with a 0.1 M concentration of supporting electrolyte.

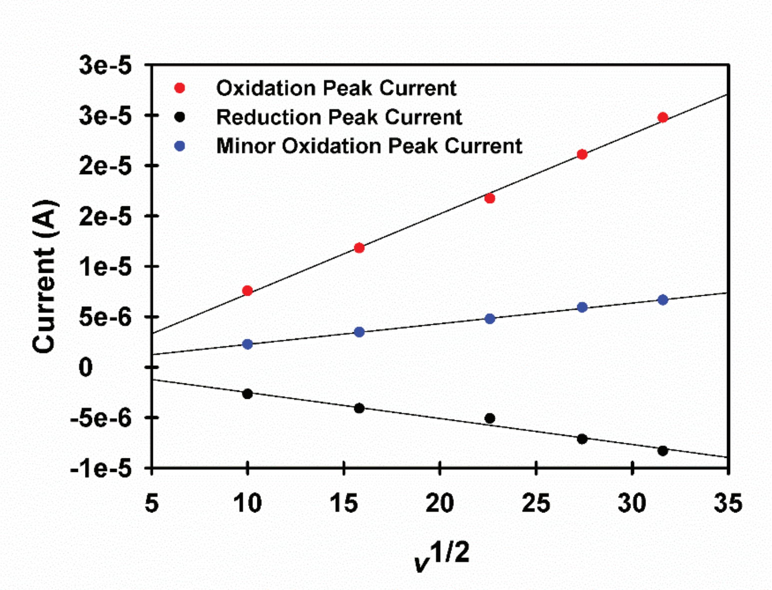

Figure 66: Linear relationship of measured peak currents of [Co(acac)$_2$((CC)$_2$bpy)] compared to the square root of the scan rate.

Similar behavior is shown by **[Co(dbm)$_2$((CC)$_2$bpy)]** and is shown in Figure 67. There is an oxidation peak at 0.10 V vs Fc$^{0/+}$, a reduction peak at -0.64 V vs Fc$^{0/+}$ and a peak separation of 740 mV when examined at a scan rate of 100 mV/s. Unlike **[Co(acac)$_2$((CC)$_2$bpy)]** there are no minor peaks present. Voltammograms takes at varying scan rates (Figure 68) also show a linear relationship between the square root of the scan rate and the measured peak current (Figure 69) indicated that this is also a species in solution. Additionally, both redox events are clearly dependent on the other as shown by the decrease in measured peak current with repeated scans when the potential window is restricted to just one peak (Figure 70).

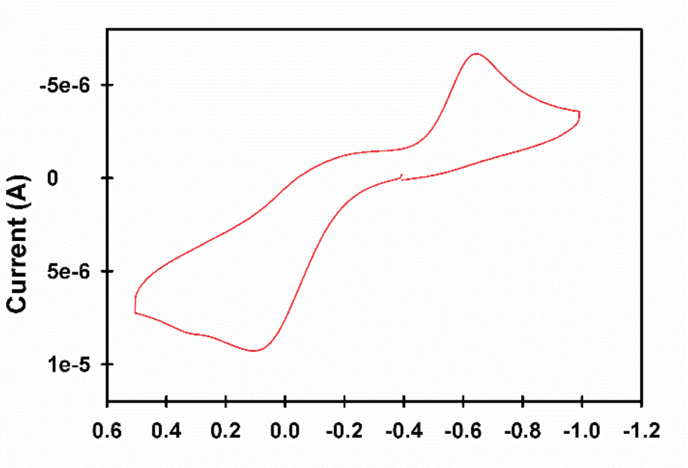

Figure 67: Solution electrochemistry of Co(dbm)$_2$(bpy) in methylene chloride with 0.1 M concentration of supporting electrolyte taken at a glassy carbon electrode with a scan rate of 100 mV/s. The small peak visible at 0.3 V is due to a contaminant present in the background.

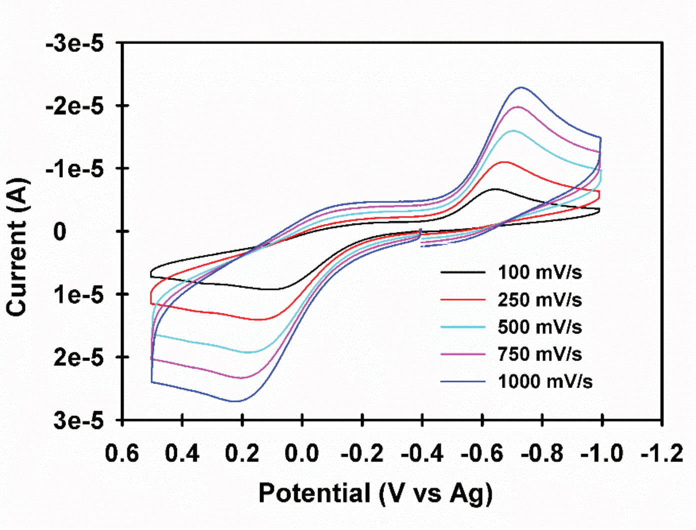

Figure 68: Cyclic voltammograms of [Co(dbm)$_2$((CC)$_2$bpy)] taken at multiple scan rates in acetonitrile with a 0.1 M concentration of supporting electrolyte.

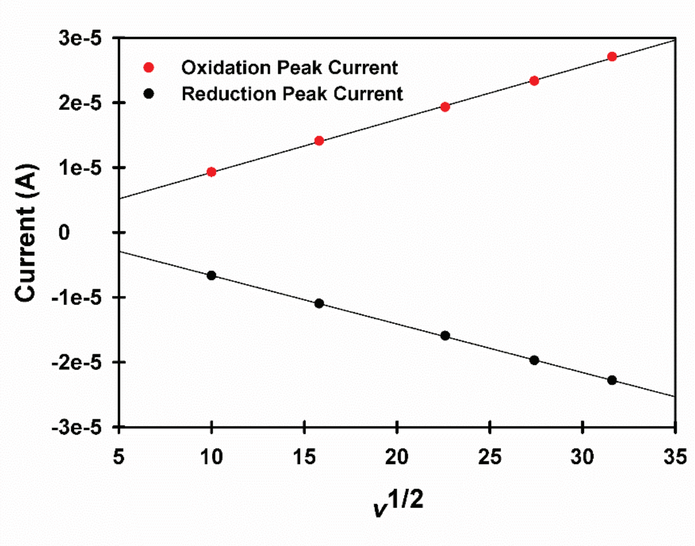

Figure 69: Linear relationship of measured peak currents of [Co(dbm)$_2$((CC)$_2$bpy)] compared to the square root of the scan rate.

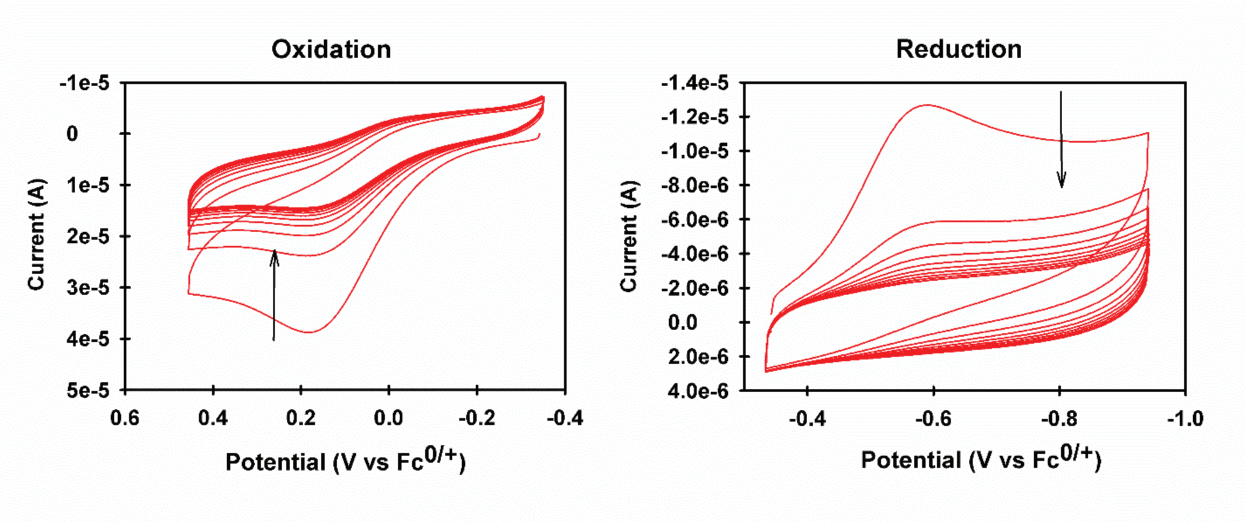

Figure 70: Repeat scans of [Co(dbm)$_2$((CC)$_2$bpy)] taken in acetonitrile at 500 mV/s.

Peak currents observed in both cases exhibit a linear relationship to the square root of the scan rate consistent with the behavior of a species in solution. The large difference in peak separation makes sense considering the much larger diketonate ligands present in **[Co(dbm)$_2$((CC)$_2$bpy)]** that likely contribute to a larger reorganization energy. Curiously, in both cases the profiles of the oxidation and reduction peaks are markedly different in shape and appearance with larger peak currents observed for the oxidation.

Voltammograms of both complexes are similar to those obtained by Harding although only **[Co(dbm)$_2$((CC)$_2$bpy)]** has an analogue in Harding's work. Curiously, Harding noted three peaks for the analoguous complex, and oxidation peak at -0.07 V and a pair of reduction peaks at -0.38 V and -0.61 V vs Fc$^{0/+}$. The peak at -0.38 V was considerably smaller and attributed to a high-spin cobalt(III) intermediate formed immediately upon oxidation, the bulk of which rapidly converts to a low-spin cobalt(III) that is more stable than the high-spin intermediate and more difficult to reduce.[79] This is a consequence of the electronic rearrangement that are represented as steps B and C in the RCSCO square scheme. Electrochemical irreversibility in RCSCO reactions comes not just from the initial change transfer event but also from the electronic restructuring represented by the spin exchange constant.[66] Appearance of a minor reduction peak would indicate that the spin exchange constant for Harding's analogous [Co(dbm)$_2$(bpy)] complex is relatively small leading to a mixture of high-spin and low-spin configurations at room temperature.

The lack of minor peaks in cyclic voltammograms of **[Co(dbm)$_2$((CC)$_2$bpy)]** electrochemistry likely signifies that $K_{ese,3+}$ equilibrium constant is small and thus overwhelmingly favors the formation of the low-spin state at room temperature. This may be due to the influence of the ethynyl groups on bipyridyl basicity. Ring substituents are known to change the basicity of the 2,2'-bipyridine ligand.[245–247] It is not unreasonable to speculate that an electron-donating functional group might increase the basicity of the bipyridyl nitrogens and therefore increase the ligand field splitting energy of the complex result in a greater stabilization of the low-spin cobalt(III) that leaves no high-spin intermediate available to reduce under experimental conditions. However, ethynyl groups are electron withdrawing,[231] not donating, and their influence on the electronic properties of the ligand should reduce the basicity of the two bipyridyl nitrogens. Therefore, the lack of a high-spin cobalt(III) intermediate cannot be explained by increased ligand field caused by increased sigma bonding from the bipyridine ligand. However, the reduced electron density in the bipyridyl aromatic system caused by the ethynyl group could lead to comparatively less electron density around the newly formed cobalt(III) and make that metal center more acidic.[248–250] This increased Lewis acidity could increase the affinity of the metal center for the β-diketonate ligands and play a role in shifting the spin exchange equilibrium to overwhelmingly favor the low-spin cobalt(III) complex.

[Co(acac)$_2$((CC)$_2$bpy)] appears to have minor reduction and oxidation peaks at 0.03 V vs Fc$^{0/+}$ and -0.146 V vs Fc$^{0/+}$ respectively. These might also be ascribed to intermediates like those reported by Harding with a high-spin cobalt(III) intermediate responsible for the early reduction at -0.146 V vs Fc$^{0/+}$ and a low-spin (S=1/2) cobalt(II) intermediate that rapidly converts to the high-spin S=3/2 state could be the cause of the oxidation seen at 0.03 V vs Fc$^{0/+}$.

The presence of high- and low-spin intermediates in the voltammograms of the voltammograms of **[Co(acac)$_2$((CC)$_2$bpy)]** that are not seen in **[Co(dbm)$_2$((CC)$_2$bpy)]** indicates that factors other than substituents on the bipyridine ligand can influence the stability of these intermediates. Clearly, the β-diketonate ligands play a role as well. This difference is likely due to the R-groups on the acac and dbm ligands. The phenyl groups of 1,2-diphenylpropane-1,3-dione are much larger than the methyl groups on acetylacetone, and from Harding's X-ray studies it is known that the diketonate ligands bind to the cobalt(II) center at an angle and reorient themselves upon oxidation of the complex to cobalt(III). In this angled arrangement the phenyl groups of the dbm ligand likely experience unfavorable steric interactions with the adjacent bipyridyl ligand that favor the more octahedral conformation assumed by the complex upon oxidation. The acac ligands with only methyl groups probably experience less steric interactions with neighboring ligands and can thus accommodate a wide array of coordination geometries required by the various spin state intermediates.

4.4 LbL Growth Attempts

4.4.1 Methods

4.4.1.1 Surface Preparation

Sections of ITO coated glass were cleaned by sonication in ethanol or methanol followed by sonication in a 2:1 solution of ethanol or methanol and water saturated with potassium carbonate. These slides were then rinsed with water, dried under a stream of nitrogen, and placed in a solution of 1.5 mM 11-azidoundecylophosphonic acid in THF. Slides were left in this solution for at least 24 hours to allow self-assembly of the phosphonate monolayers to take place. Once ready, the slides were removed from solution and rinsed with THF before drying under a stream of nitrogen. Slides were then annealed for at least one hour at 75°C before use.

4.4.1.2 Layer Growth Solutions

2mM solutions of complex and 2.5 mM solutions of ethynyl ferrocene were prepared in dimethylformamide and stored for use as needed. Copper ligand solutions to catalyze the click reactions were prepared ahead of time as well in a 50:50 mixture of distilled water and dimethyl sulfoxide containing copper sulfate and tris((1-benzyl-4-triazolyl)methyl)amine (TBTA) ligand were added to achieve concentrations of 38.5mM and 45.5 mM respectively. Reductant solutions of 2,5-diterbutylhydroquinone were prepared in dimethylsulfoxide fresh at a concentration of 39.6 mM. 20 mM solutions of the 1,3,5-tris(azidomethyl)benzene (mestylene) linker was prepared in dimethylformamide and stored for use as needed.

4.4.1.3 Layer Growth Procedure.

Layer click solutions were made by combining aliquots of copper ligand solution, reductant, and complex to achieve final concentrations of 5.5 mM and 6.5 mM, 11.3 mM, and 1.14 mM respectively. Linker reaction solutions were prepared in an identical fashion to achieve a linker concentration of 5.7 mM. ITO slides were placed face-down on glass microscope slides with glass spacers and the reaction solutions were dispensed beneath the slide. The slide was then left for at least ten minutes before rinsing with dichloromethane, a 6.5 mM solution of disodium EDTA in a 1:1 water ethanol solution, ethanol, and finally distilled water and dried under a stream of nitrogen. Layer growth was followed spectroscopically using an Agilent 8453 diode array.

4.4.1.4 Electrochemistry

Surface electrochemistry was carried out in a three-electrode cell with the ITO substrate serving as a working electrode. The electrolyte solution of 0.1 M tetrabutylammonium hexaflurophosphate (TBAPF$_6$) in acetonitrile contained in a Teflon cone above the working electrode. This cone also contained the platinum wire counter electrode and silver pseudo-reference electrode. All scans were referenced to the ferrocene/ferrocenium redox couple measured in a separate three electrode cell with the same psudeo-reference and counter electrodes and a glassy carbon working electrode and performed using Pine Wavedriver potentiostat.

4.4.2 Verification of SAM Formation

4.4.2.1 Electrochemical Response of an Ethynyl Ferrocene Monolayer

SAM formation was verified by test CuAAC reactions of ethynyl ferrocene onto azide-functionalized ITO glass. Cyclic voltammograms, shown in Figure 71, of this surface taken in acetonitrile 0.1 M tetrabutylammonium hexafluorophophate electrolyte display gaussian waves with a peak width of 272 mV at 100 mV/s. This gaussian behavior together with the linear relationship displayed between peak current respect to scan rate (Figure 72), is consistent with a surface bound species. This confirms that the phosphonate SAM formed as expected.

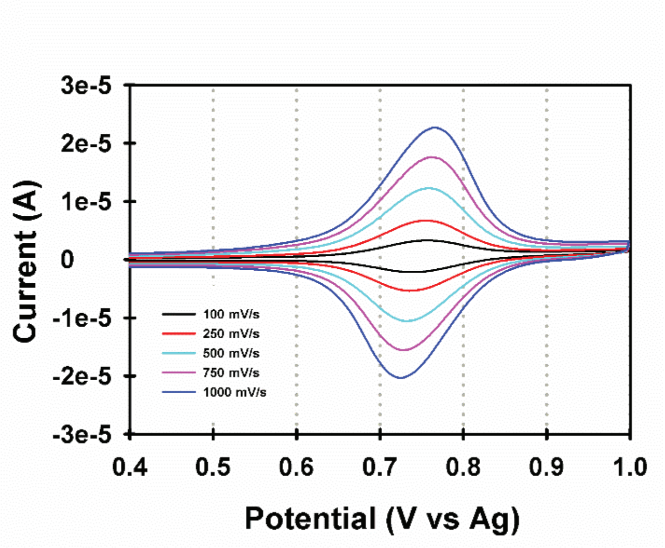

Figure 71: Cyclic voltammogram of ethynyl ferrocene bound to a phosphonate SAM on ITO glass in acetonitrile with 0.1M TBAPF$_6$ electrolyte.

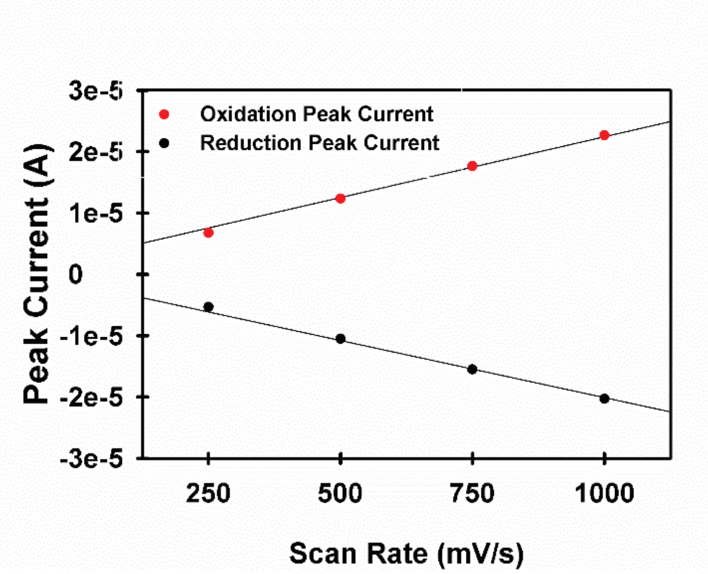

Figure 72: Relationship of measured peak currents and scan rate.

Integration of the oxidation and reduction waves taken at a scan rate of 100 mV/s allows for the determination of the amount of charge passed. These values may be used to calculate the surface coverages in terms of molecules per square centimeter using the following relationship.

$$\Gamma = \frac{Q}{nFA} \tag{2}$$

Where A is the area of the electrode surface in centimeters, n is the number of electrons, F is Faraday's constant in coulombs per mole., Q is the amount of charge passed in coulombs, and Γ is the surface coverage measured in molecules/cm^2. Using this relationship of surface coverage of 1.17 ×10^{14} molecules/cm^2 was determined. This coverage is consistent with monolayer formation[28] and serves to further confirm that surface functionalization was indeed successful.

4.4.2.2 Layer Growth Of Zinc Tetraphenylethynylporphyrin

As an additional test of phosphonate SAM formation three layers were grown on ITO using a zinc tetraphenylporphyrin (ZnTPEP) that was previously studied in our lab.[30] This was done because reliable layers have been grown with consistent success in the past. Identical layer growth procedures as those used with both β-diketonates with the exception that the ZnTPEP solution had a concentration of 2.85 mM instead of 1.14 mM. This multilayer was green when viewed with the human eye. The UV/Vis spectra seen in Figure 73 of ZnTPEP are difference spectra with the absorbance of the bare SAM on ITO subtracted from the absorbance of each layer. With each layer added absorbance increased linearly across the spectrum. The spectra show a large peak at 442 nm, and three smaller peaks at 310, 568, and 613 nm.

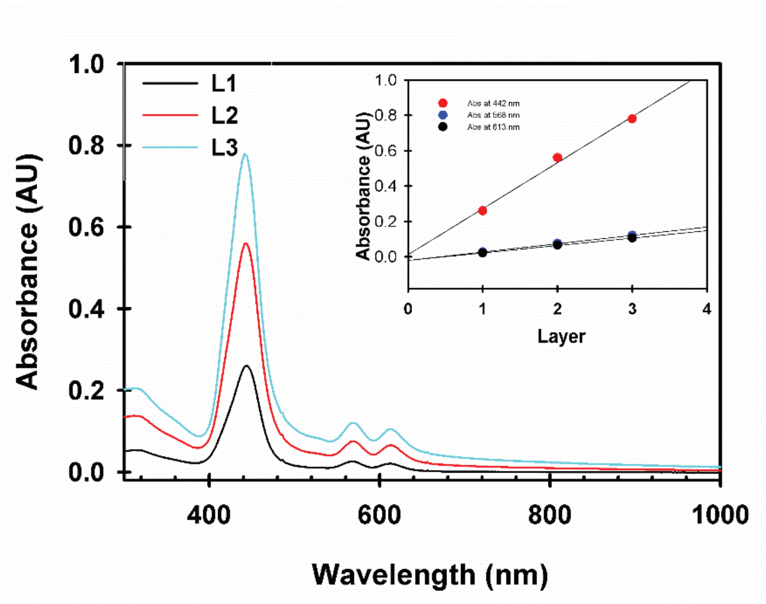

Figure 73: Spectroscopic response of three layers of ZnTPEP deposited on an ITO SAM using mestylene linker molecules.

4.4.3 Layer Growth Attempts With [Co(dbm)$_2$((CC)$_2$bpy)] and [Co(acac)$_2$((CC)$_2$bpy)]

Layer growth using phosphonate SAMS on ITO glass (Figure 74) was attempted for both **[Co(acac)$_2$((CC)$_2$bpy)]** and **[Co(dbm)$_2$((CC)$_2$bpy)]** using CuAAC LbL techniques. For each attempted layer UV-Vis spectra were taken of the coated ITO slides to measure layer growth spectroscopically.

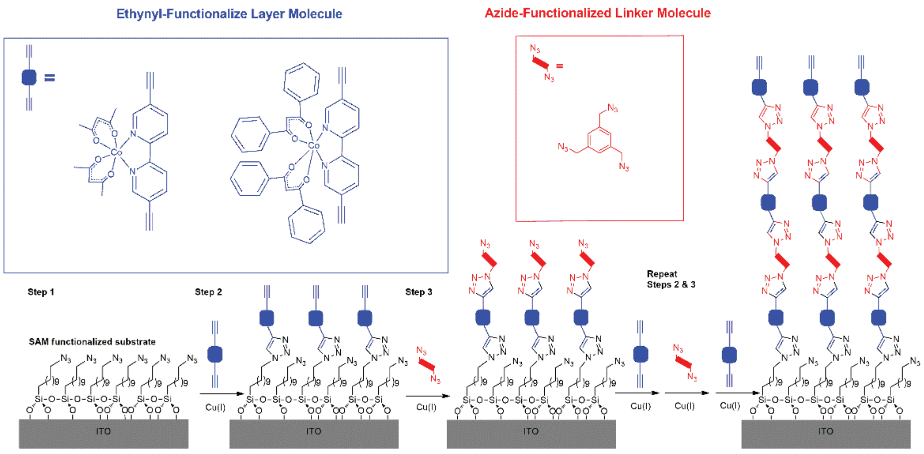

Figure 74: Multilayer growth scheme incorporating [Co(acac)$_2$((CC)$_2$bpy)]and [Co(dbm)$_2$((CC)$_2$bpy)].

Initial layer growth experiments conducted in this manner were not encouraging. At first, only a single layer seemed to be forming according to absorbance measurements. This was soon attributed to the differences in solubility between the β-diketonates and the mesitylene linker. The copper TBTA ligand solution requires water and dimethyl sulfoxide as solvents combined in a 1:1 volume ratio, the reductant is dissolved in DMSO, while the chromophore and linkers require solvents that are miscible with these other cosolvents. This severely limits solvent options and poses some challenges. During initial layer growth attempts the β-diketonates were dissolved in DMF and the mesitylene linker was dissolved in DMSO according to previous layer growth procedures with tetraphenyl porphyrins. Using these solvents only one layer was consistently observed in UV-Vis spectra and attempts at growing additional layers were inconclusive. Once this issue was identified it was hypothesized that the low solubility of the β-diketonates in DMSO was preventing the mesitylene from reacting with surface-bound β-diketonates in good yield and a new methylene linker solution was prepared in DMF. Once this change was made the spectra like those shown in Figure 75 and Figure 76 were collected which indicated consistent layer growth with each deposition step.

ITO coated glass absorbs strongly in the near-UV which requires that difference spectra be taken to adequately visualize layer growth. Other artifacts are also present in the spectrum due to the absorbance of the ITO substrate including sharp spurious peaks which sometimes appear between 500 and 700 nm and an occasional decrease in absorbance in the region above 400 nm which may occur in some spectra as a result of a changing index of refraction as layers are deposited causing an apparent decrease in absorbance as light is refracted away from the detector. The changes in the spectra caused by layer deposition are small but compelling. Because of the influence of ITO on the spectra an exact match to the solution spectra cannot be expected but the growth of peaks in the 300 to 400 nm range are expected and consist with the measured solution spectra for both complexes. Encouragingly, the changes in absorbance with each layer of **[Co(dbm)$_2$((CC)$_2$bpy)]** (Figure 75) and **[Co(acac)$_2$((CC)$_2$bpy)] (**Figure 76**)** are both linear.

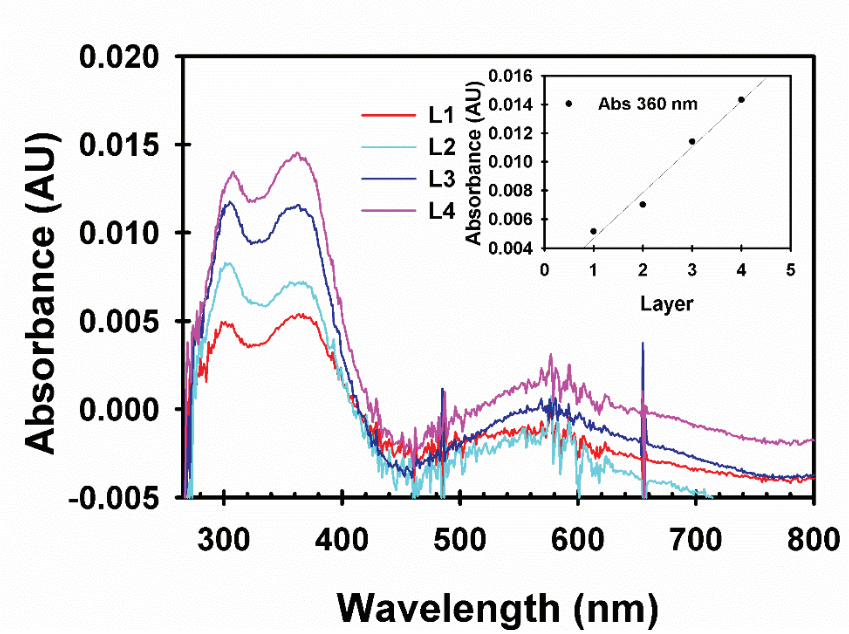

Figure 75: Layer growth spectra of [Co(dbm)$_2$((CC)$_2$bpy)] the inset in the top right shows the increase in absorbance at 360 nm for each added layer.

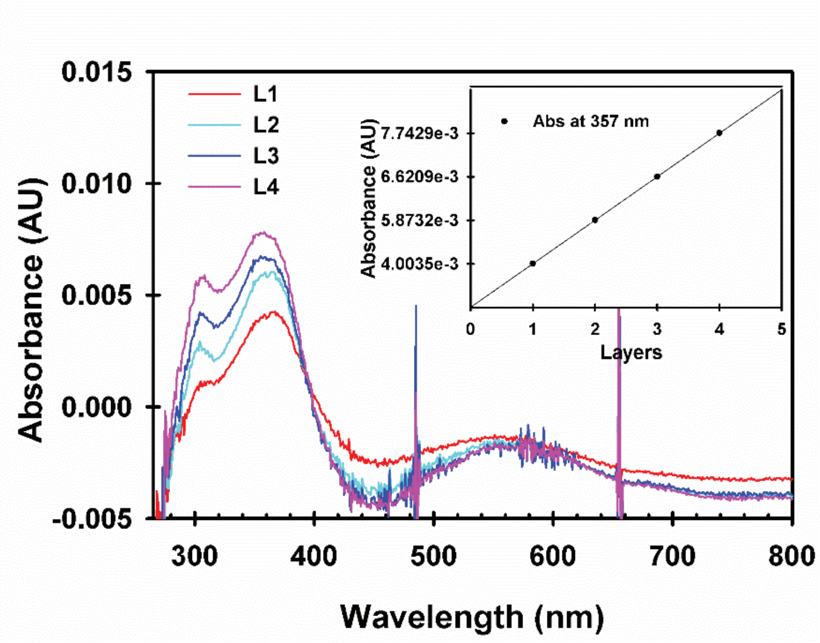

Figure 76: Layer growth spectra of [Co(acac)$_2$((CC)$_2$bpy)]. The inset in the top right shows in the increase in absorbance with each layer at 357 nm.

Layers of **[Co(dbm)$_2$((CC)$_2$bpy)]** show a broad absorption between 300 and 400 nm with peaks at 307 and 360 nm. The absorbance of even four layers is small with a maximum of 0.014. Attempted multilayer growth experiments of **[Co(acac)$_2$((CC)$_2$bpy)]** resulted in similar spectra with peaks visible at 305 nm and 357 nm but with a smaller maximum absorbances of just 0.0077.

Using a modified Beer's Law for self-assembled monolayers, together with the electrochemically determined surface coverage for a ferrocene monolayer, the spectroscopic response of a monolayer of both complexes can be calculated using estimated molar absorptivity coefficients derived from solution studies using the following equation:

$$A = 1000\varepsilon\Gamma \tag{3}$$

Where ε is a molar absorptivity coefficient in units of L·mol^{-1}·cm^{-1} and Γ is surface coverage in mol·cm^{-2}.[251] Using a molar absorptivity corresponding to the major peaks seen in the layer growth experiments at 322 nm for **[Co(acac)$_2$((CC)$_2$bpy)]** and 311 nm for

[Co(dbm)$_2$((CC)$_2$bpy)] of 2855 L·mol^{-1}·cm^{-1} and 4177 L·mol^{-1}·cm^{-1} respectively. Using these values together with an assumed surface coverage of 1.94 × 10^{-10} mols/cm^2 gives expected absorbances for a single monolayer of complex of 0.0006 for **[Co(acac)$_2$((CC)$_2$bpy)]** and 0.0008 for **[Co(dbm)$_2$((CC)$_2$bpy)]**.

The actual measured absorbances for monolayers of both complexes are larger than are predicted by Beer's law. The monolayer of **[Co(dbm)$_2$((CC)$_2$bpy)]** shows an absorbance of 0.0041 at 311 nm and the monolayer of **[Co(acac)$_2$((CC)$_2$bpy)]** has an absorbance of 0.0012 at 322 nm. This combined with the linear absorbance increase with each layer deposited is encouraging and suggests that multilayers are forming with good coverage. However, these absorbances are much less than what was achieved with ZnTPEP which had a monolayer absorbance of 0.2589 at 442 nm. Furthermore, multilayers of ZnTPEP are visibly green to the human eye while multilayers constructed of both **[Co(dbm)$_2$((CC)$_2$bpy)]** and **[Co(acac)$_2$((CC)$_2$bpy)]** on ITO have no visible color at all.

Taken all together these observations would seem to indicate that these β-diketonates may not be suitable for electrochromics in their current form. The linear changes in the absorbance do suggest that multilayers are forming. Differences between the predicted and measured absorbances would also seem to indicate that monolayer formation with these β-diketonates was more successful than the test monolayers formed by ethynyl ferrocene. However, the overlap of ITO's absorbance spectrum with the absorbances observed for both β-diketonates as well as the differences in spectral features make it difficult to claim success with any degree of confidence.

4.4.4 Cyclic Voltammetry of Co(dbm)$_2$((CC)$_2$2,2'-bpy) Monolayers

Electrochemistry of presumed monolayers of **[Co(dbm)$_2$((CC)$_2$bpy)],** shown in Figure

77, fails to display the oxidation and reduction waves that would have been expected based on the solution electrochemistry. However, two irreversible electrochemical waves are visible with an oxidation wave at 1.28 V vs $Fc^{0/+}$ and a reduction wave at –0.64 V vs $Fc^{0/+}$ and an overall peak splitting of 1.92 V although some drift in these potentials was observed over repeated experiments. While the peak splitting is much larger than what was observed in solution at first glance this high degree of peak splitting is not unreasonable. Furthermore, these two peaks are clearly linked. Repeated scanning in both the anodic (Figure 78) and cathodic (Figure 79) directions show a clear decrease in measured currents indicating that the reduction process requires the oxidation process to take place first.

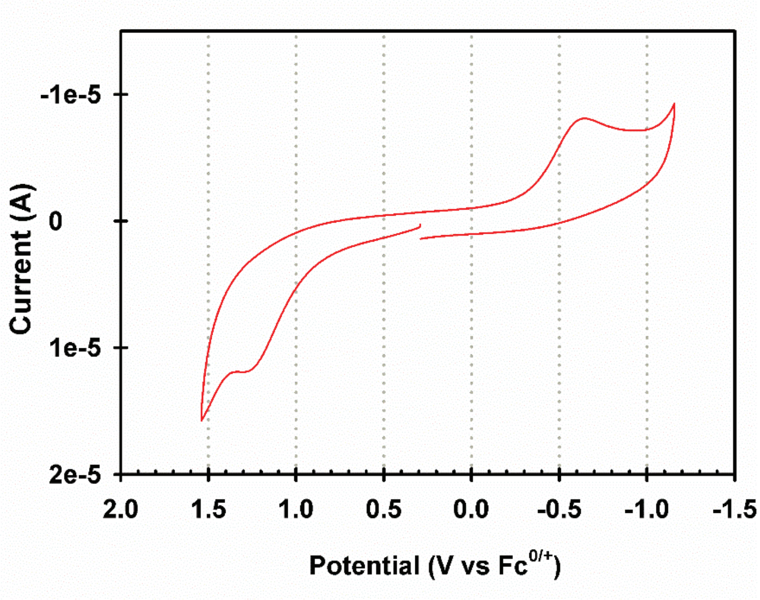

Figure 77: Electrochemistry of a presumed monolayer of $[Co(dbm)_2((CC)_2bpy)]$taken at 250 mV/s beginning at 0.3 V vs $Fc^{0/+}$ an scanning anodically.

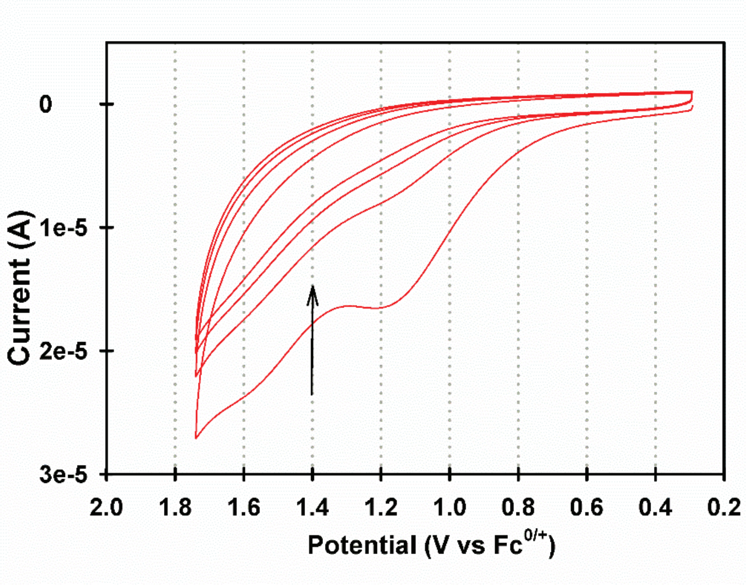

Figure 78: Repeat scans of the oxidation peak of a presumed monolayer of [Co(dbm)$_2$((CC)$_2$bpy)] taken at 500 mV/s.

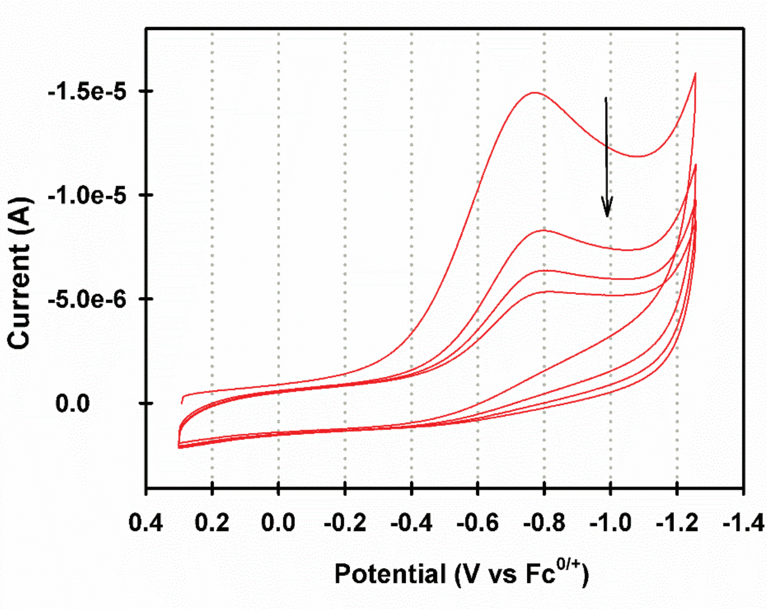

Figure 79: Repeat scans of the reduction peak of a presumed monolayer of [Co(dbm)$_2$((CC)$_2$bpy)] taken at 500 mV/s.

ITO has a relatively high resistance and surface anchoring may inhibit some of the geometric rearrangements that accompany SCO. With these two factors in mind a shift to higher potentials in both the anodic and cathodic directions is not an unreasonable expectation. These peaks are clearly linked as shown by repeated scans of each peak taken at 500 mV/s. Both peaks diminish with repeated incomplete cycles showing that that the oxidation is clearly required for the reduction to take place and vice versa. Analysis of the scan rate dependence and peak currents here shows a linear relationship when compared to the square root of the scan rate, indicating that this reaction involves a species in solution and not on the surface.

4.4.5 Cyclic Voltammetry of [Co(acac)$_2$((CC)$_2$bpy)] Monolayers

Electrochemistry of presumed monolayers of **[Co(acac)$_2$((CC)$_2$bpy)]**, shown in Figure 80, displays similarly irreversibly electrochemistry with an oxidation peak at 1.5 V vs Fc$^{0/+}$, a reduction wave at -0.85 V vs Fc$^{0/+}$ and a peak separation of 2.35 V.

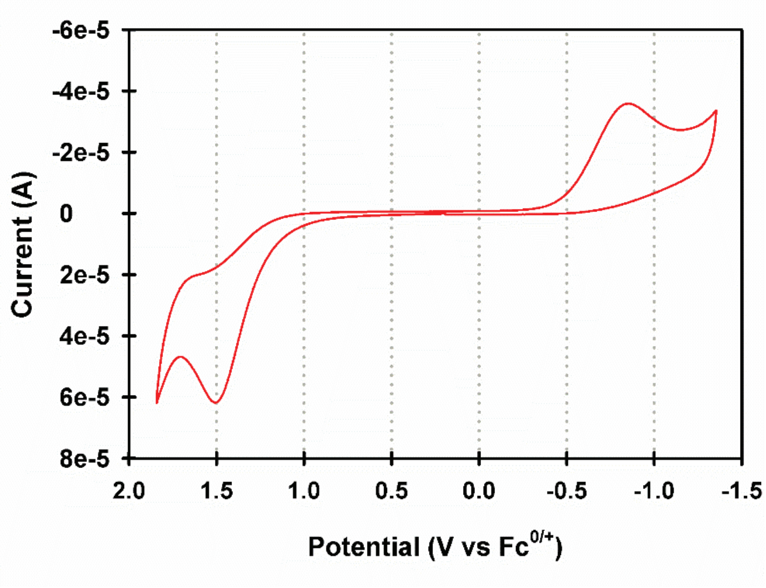

Figure 80: Electrochemistry of a presumed monolayer of [Co(acac)$_2$((CC)$_2$bpy)] taken at 250 mV/s.

4.4.6 Background Solution Electrochemistry of an Azidophosphonate SAM on ITO

Electrochemistry performed using an untreated phosphonate SAM on an ITO electrode in acetonitrile with 0.1M TBAPF$_6$, shown in Figure 81, displays electrochemistry very similar to that observed with both **[Co(acac)$_2$((CC)$_2$bpy)]** and **[Co(dbm)$_2$((CC)$_2$bpy)]** indicated that the observed electrochemistry is indeed due to reactions with the solvent and not with a bound species. At this scan rate the oxidation event occurs at 1.14 V vs ferrocene and the reduction peak is at -0.9 V vs ferrocene, with a total peak separation of 2.04 V.

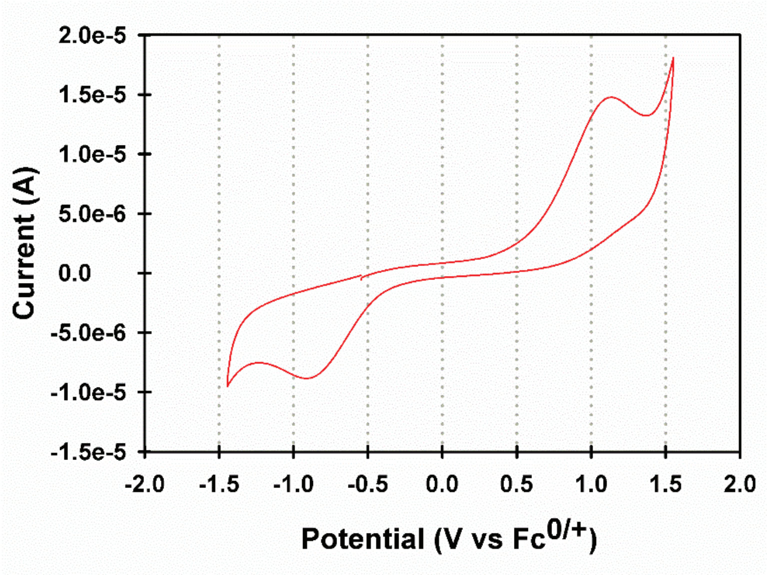

Figure 81: Cyclic voltammogram of an ITO SAM in acetonitrile at 250 mV/s.

When measured peak currents, shown in Figure 82, are compared to scan rate the relationship is clearly non-linear ruling out the presence of a surface-bound species. The peaks currents do however increase linearly with respect to the square root of the scan rate, a clear indication that this process involves a species in solution.

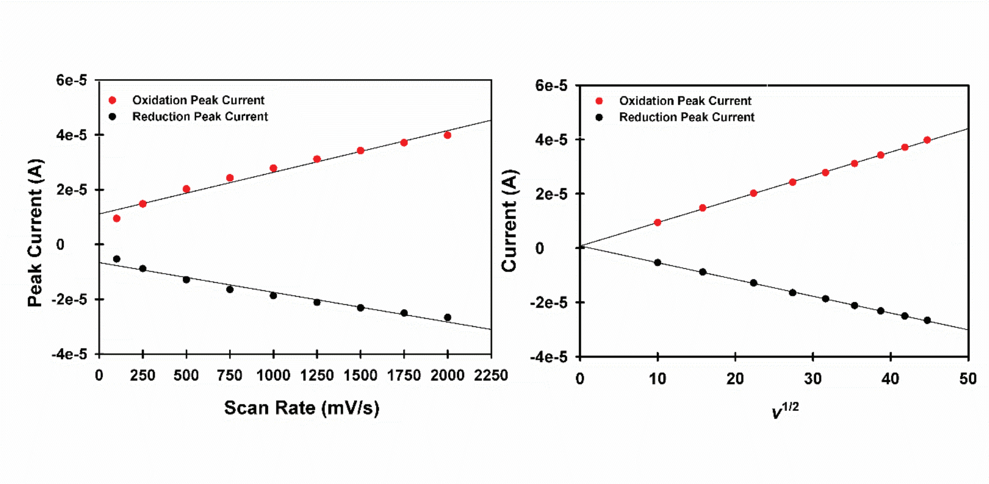

Figure 82: Scan rate dependence for background electrochemistry observed in acetonitrile using an untreated phosphonate SAM on ITO.

4.4.7 Speculations on the Nature of the Observed Electrochemistry

Scan rate dependence data indicates that the observed redox reactions are not due to surface-bound species but rather to a species in solution. Since the observed behavior is inconsistent with what would be expected of either β-diketonate complex in solution the obvious conclusion would seem to be that this is instead some kind of reaction with the acetonitrile solvent. The exact nature of this reaction is unclear, but the data could indicate the buildup of acetonitrile-derived polymers on the electrode surface. This is supported by the observed decreased in peak currents seen during repeated cycling of monolayers and by the observation of the formation of a yellow precipitate when oxidation potentials were held constant during attempted spectroelectrochemical experiments. It has been reported that acetonitrile forms graphene-like polymers under extreme temperature and pressure conditions to form graphene-like networks.[252] While electrochemically catalyzed versions of this reaction have not been reported it is plausible that oxidized or reduced acetonitrile species may undergo polymerization reactions during cycling experiments. If a polymer network is indeed forming from reactions of acetonitrile, it may be depositing a film on the ITO surface. This could explain the decrease in peak current seen in the cyclic voltammograms after repeated cycling at 500 mV/s in Figure 83 and Figure 84.

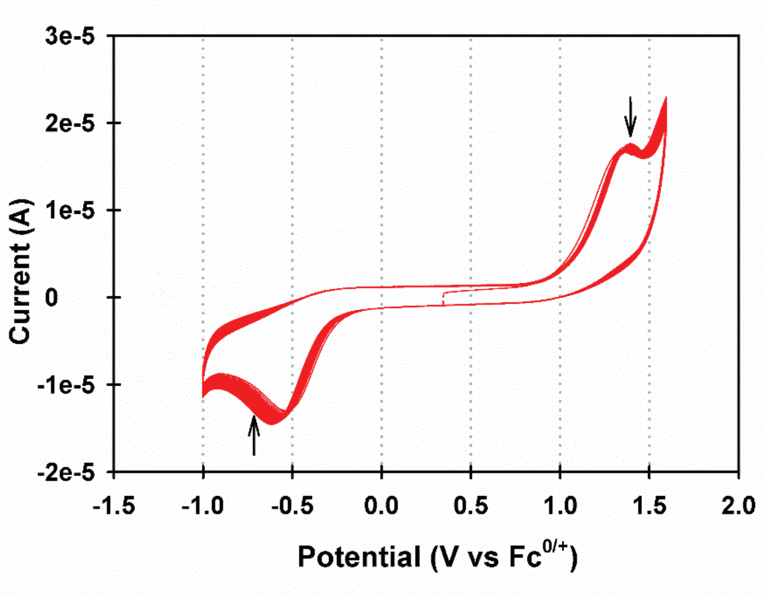

Figure 83: Repeat scans performed with two presumed layers of [Co(dbm)$_2$((CC)$_2$bpy)] at 500 mV/s.

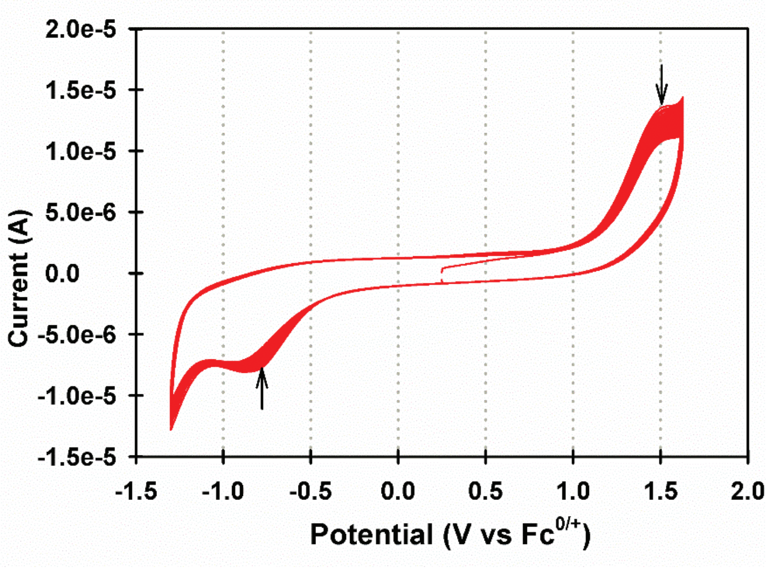

Figure 84: Repeat scans performed with two presumed layers of [Co(acac)$_2$((CC)$_2$bpy)] at 500 mV/s.

4.5 Some Explanations for the Apparent Lack of Multilayer Electrochemistry

Spectroscopic evidence for multilayer growth was obtained for both **[Co(dbm)$_2$((CC)$_2$bpy)]** and **[Co(acac)$_2$((CC)$_2$bpy)]**. The measured absorbances of these multilayers are small and difficult to distinguish from the ITO background but there is reason to believe that layer growth did occur. The following subsections will discuss several factors which could influence both multilayer growth and electrochemistry.

4.5.1 The Complexes are Unstable in Experimental Conditions

It is possible that the complexes are somewhat unstable in click conditions. The 2,5—di-tert-butylhydroquinine used as a reductant in the CuAAC solutions is slightly acidic. The pH of the click solution is approximately 4.5. It is possible that these conditions were sufficient to cause some degradation of the complexes by protonating the β-diketonates. This is possible and future work should explore the stability of these complexes under acidic conditions and in the presence of different reducing agents. It is possible that more success would be had using sodium ascorbate as a reductant instead of hydroquinone since the ascorbate salt would not introduce additional protons into the click solutions. Alternatively, a buffered CuAAC solution may correct this issue. However, because some surface changes were observed during the course of multilayer experiments it may be more productive to consider the influence of ligand structure on LbL fabrication methods.

4.5.2 Confinement in the Multilayers Inhibit RCSCO

One factor which could explain the lack of RCSCO is the triazole linkages formed during the CuAAC reaction. The effect of functional groups bound to the bipyridyl rings can be profound. Differences in electrochemistry between **Co(dbm)$_2$((CC)$_2$bpy)** and the analogous complex studied by Harding demonstrated the effect of the ethynyl groups on the electronic properties of the bipyridyl ligand. It follows that triazole rings could also influence the electronics of these complexes, but another cause for concern is the geometric confinement that the triazole linkages and the entire multilayer might impose on these complexes. Large geometric rearrangements are known to accompany SCO in transition metal complexes. In their X-ray crystallographic studies Harding noted a $\Delta\Sigma$ of 52 and noted that the β-diketonate ligands shifted from an angled to planar coordination geometry. The bonding angles of the bipyridine ligand also change upon oxidation. If the triazole linkages are restricting the movement of these complexes that could explain that lack of observed RCSCO.

Steric interactions between polymer chains in the multilayer could also be at fault. As stated already, there are significant geometric rearrangements that accompany RCSCO and if the ligands of adjacent complexes in the multilayers experience steric interactions this could also result in the lack of observed RCSCO.

4.5.3 Steric Hindrance is Preventing the Click Reactions

Another possible explanation for the lack of multilayer growth is that the steric hindrance is preventing the click reaction from proceeding with a good yield. A proposed mechanism for the copper(I) catalyzed azide-alkyne cycloaddition (Figure 85) involves multiple intermediates which undergo multiple rearrangements form the triazole ring beginning with the formation of a σ,π-di(copper) acetylide which comes together with the terminal azide group on the second molecule to form a cyclic intermediate as part of a larger catalytic cycle leading to the formation of the triazole heterocycle.[253]

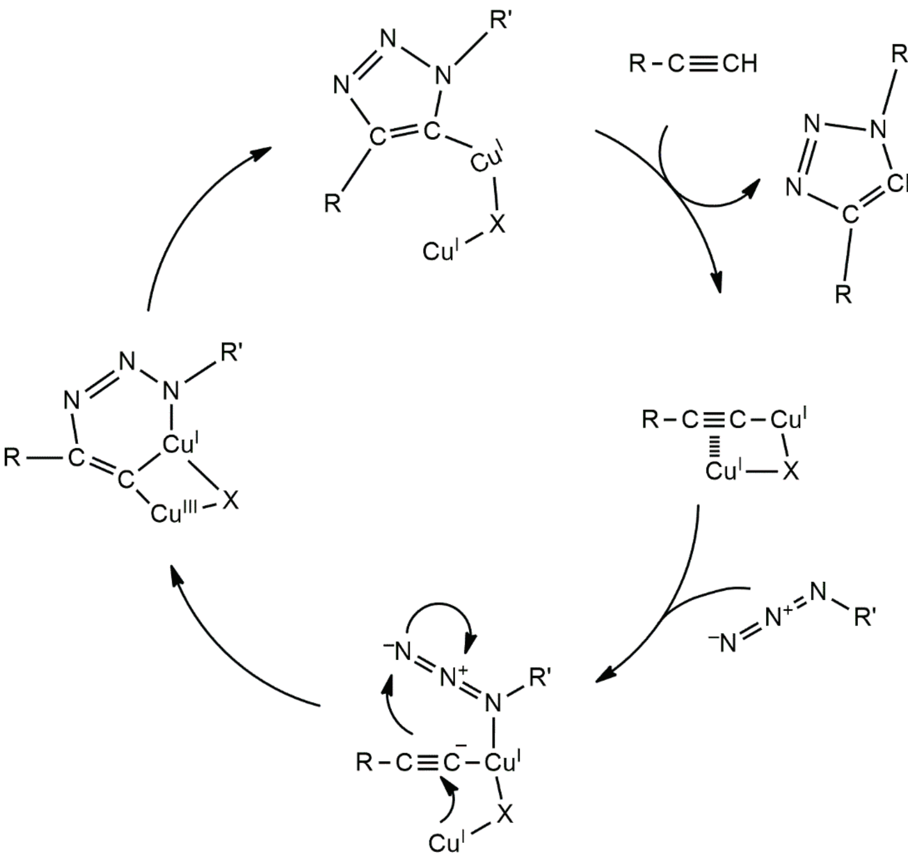

Figure 85: Mechanism of the copper(I) catalyzed azide-alkyne cycloaddition reaction. Adapted from the mechanism proposed by Zhu and coworkers.[253]

While the triazole ring formation has been said to mostly ignore steric bulk there are instances where the steric bulk of nearby functional groups has been identified as a possible limiting factor in CuAAC reactions of esters,[254] and high-weight polymers.[255] Another steric concern could arise due to the shepherding ligands used to guide the copper(I) catalyst. Many of these ligands, including the tris(benzyltriazolylmethyl)amine ligand used here, are large and sterically bulky. Ligand-free versions of this reaction are possible,[256–258] however, eliminating this ligand from the reaction or using a smaller ligand may introduce new issues since the shepherding ligands are vital to ensure that the reaction takes place quickly with good yields.[259] With this in mind, it is probably better to consider how the structures of the complexes may influence reaction intermediates and how synthetic modifications may help to alleviate steric obstacles to multilayer formation.

In the past our group has had success in growing multilayers of zinc complexes of ethynyl-functionalized tetraphenylporphyrins and functionalized perylenedimides.[29–31,260] In both cases the ethynyl group is attached to an intermediate phenyl ring which is in turn attached to the central structure of the molecule. One explanation for why those multilayers could be built reliability is the presence of these spacers. This arrangement likely grants additional flexibility to ethynyl group which could be more amendable to the intermediates formed during the formation of the triazole moiety. The idea that the ethynyl group attached directly to the bipyridyl ring lacks the flexibility needed to form the cyclic intermediates is compelling, however, reactions of similar ethynyl groups on an aromatic ring without spacers have been reported with yields as high as 85% on an azide-functionalized surface.[261] Adding spacers between the bipyridyl ring and the ethynyl group might still solve the apparent reactivity problem but not because the spacers would confer greater flexibility but because the increased size would move the ethnyl groups away from the sterically bulky β-diketonate ligands.

Many β-diketonate derivatives are sterically bulky due to the structures of their R-groups. In the complexes synthesized for this research these R-groups are close in proximity to the ethynyl functional groups intended to take part in the CuAAC reaction. The proximity of these groups can be clearly seen in geometry optimized structures of **[Co(acac)$_2$((CC)$_2$bpy)]** and **[Co(dbm)$_2$((CC)$_2$bpy)]** modeled in Avogadro (Figure 86).[262,263] In Harding's complexes, X-ray studies revealed that structures of the cobalt(II) and cobalt(III) oxidations states of these complexes assume very different conformations. It might then be worth considering whether attempting the click reaction with the oxidized versions of **[Co(dbm)$_2$((CC)$_2$bpy)]** and **[Co(acac)$_2$((CC)$_2$bpy)]** but measurements obtained from Harding's X-ray structures of

$Co(tmhd)_2(bpy)$ of the distance between the central R-group carbon in the β-diketonate tertbutyl groups and the 5-carbon of the bipyridyl ring show differences on the scale of just one tenth of an angstrom. Thus, while the geometry of the cobalt(II) and cobalt(III) complexes might be very different overall, in this one aspect the geometry is not different enough to hypothesize that multilayer growth might be more successful with the oxidized cobalt(III) complex. Synthetic alterations that move the ethynyl group away from the influence of the β-diketonate R-groups are therefore the only realistic alternatives.

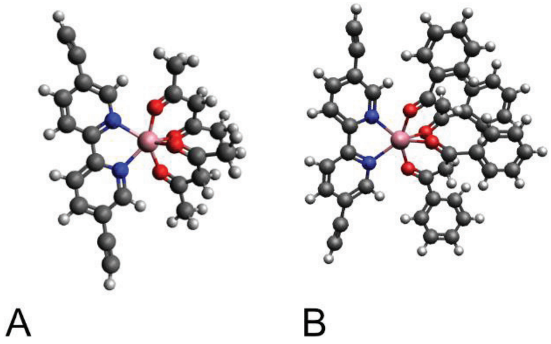

Figure 86: Geometry optimized structures of (A) $Co(acac)_2((CC)_2bpy)$ and (B) $Co(dbm)_2((CC)_2bpy)$.

4.6 Future Directions for β-diketonate Multilayers

The primary appeal of molecular electrochromics and the multilayer assembly approach used in this research are how easy the two are to customize. This customizability can be exploited in the future to design new β-diketonate complexes more suitable for use in electrochromic multilayers. The two main approaches for this are both synthetic and involve the design and synthesis of alternative bipyridyl ligands intended to add spacer atoms between the bipyridyl ring and the ethynyl groups to remove the steric hindrance that may have been preventing layer growth. The third approach does not directly address the issues that have been identified so far, but instead seeks to address some of the anticipated issues that might arise as a result of geometric confinement caused by packing of multilayer structures that could influence RCSCO behavior.

4.6.1 Adding Spacers to the Bipyridyl Ligand

There are two main paths forward concerning the addition of spacers between the bipyridyl rings and the ethynyl groups that are essential for CuAAC reactions. One option is to insert a phenyl ring between the bipyridyl and the ethynyl group. This approach is inspired by the tetrapheynylethynylporphyrins and perylenediimimdes used by our laboratory in the past. The other option is to use carbon chains of various lengths as our spacers. Both of these approaches have their merits and if they successfully enable layer growth in the future, they will also introduce additional variables to control multilayer formation and behavior.

4.6.1.1 Addition of Phenyl Ring Spacers to the 2,2-Bipyridyl Ligand

The first of these proposed solutions includes a phenyl spacer similar to that found on the tetraphenylethynylporphyrins our group has used in the past. This approach, shown in Figure 87, uses a procedure published by Nitschke[264] beginning with the synthesis of 5,5'-bis(4-(trimethylsilyl)phenyl)-2,2'-bipyridine from trimethyl[4-(trimethylsilyl)phenyl]stannane and 5,5’-((bistrimethylsilyl)ethynyl)-2,2’-bipyrdine in dimethylformide treated with lithium chloride and dichlorobis(triphenylarsine)palladium. Treatment of this intermediate with iodine monochloride would then remove the trimethylsilane groups and introduce halogen leaving groups in preparation for the Sonogashira coupling that follows. The resulting diyne 5,5′-bis[4-(tri-methylsilylethynyl)phenyl]-2,2′-bipyridine can then be used in place of 5,5’-((bistrimethylsilyl)ethynyl)-2,2’-bipyridine in the synthesis of both β-diketonate complexes and deprotected using calcium carbonate after the complex has been synthesized.

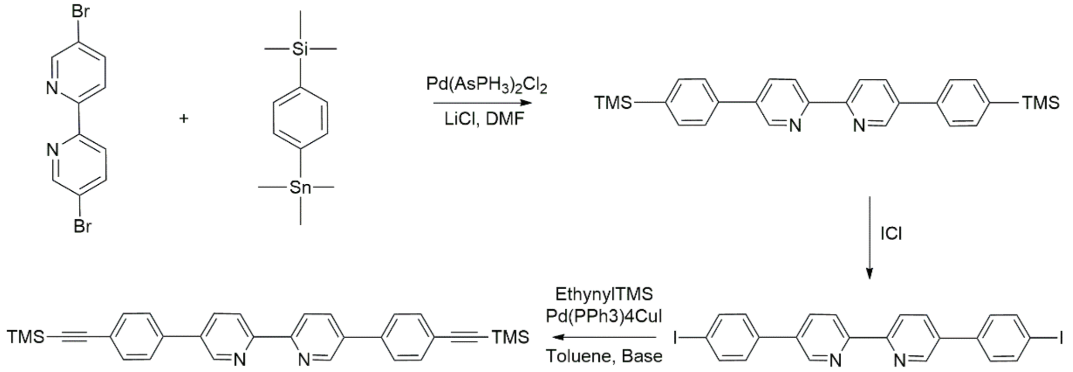

Figure 87: Reaction scheme for the synthesis of ethynyl-functionalized bipyridine ligands incorporating phenyl spacers.

An advantage of this approach is that the phenyl spacers might be amenable to further synthetic modification. For example, the addition of a charged functional group might improve ion conductivity through the multilayers. Intercalation of electrolyte is essential for facilitating charge transfer reactions in films and polymers.[265,266] It follows then that control over ion conductivity could be an important parameter in designing electrochromic multilayers.

The simplest way to synthesize this spacer (Figure 88) is to start from 2,5-dibromobenzenesulfonic acid and replace the bromine leaving groups with trimethylsilane. There are two possible synthetic routes that can accomplish this. One involved a palladium-catalyzed reaction of 2,5-dibromobenzenesulfonic acid with hexamethyldisilane.[267] Given that the synthesis of the proposed bipyridyl ligand already includes two palladium-catalyzed reactions this route is not unfeasible but would likely introduce additional time-consuming purification protocols and the value of using an expensive catalyst to make this precursor is questionable when palladium-free mechanisms are also possible. These less-expensive methods involve the reaction of 2,5-dibromobenzensulfonic acid with two equivalents of chlorotrimethylsilane catalyzed by the presence of magnesium in diethyl ether.[268] Deprotonation of the sulfonic acid could be done at the end of this synthesis or after the bipyridyl ligand has been fully synthesized but should be done before complexation to avoid protonating the β-diketonates. Phenyl spacers with other charged functional groups could be synthesized through similar routes starting from the relevant precursor including 2,5-dibromonitrobenzene and 2,5-dibromobenzoic acid. There are some downsides to this approach, namely that the proximity of the charged functional group to one of the silane leaving groups could interfere with the coupling reactions needed to attach this spacer to the bipyridyl ligand, but if the addition of spacers leads to successful multilayer assembly this could be an additional avenue to explore.

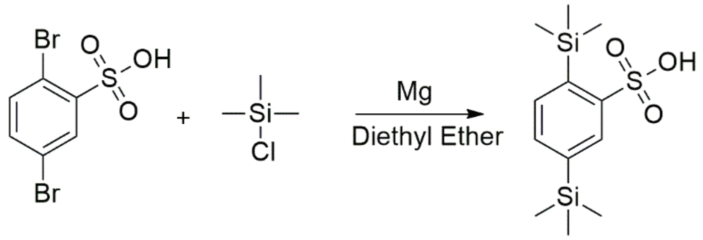

Figure 88: Proposed silation of 2,5-diebrombenzenesulfonic acid.

4.6.1.2 Addition of Alkyl Spacers to the 2,2-Bipyridyl Ligand

Another option involves the addition of an alkyl spacer between the ethynyl group and the pyridine rings. The appeal of this approach is that the length of the alkyl spacer can be varied. If complexes made from this ligand can be synthesized and clicked to the onto an azide-functionalized surface and those complexes exhibit RCSCO as expected, or if they do not, other complexes can be readily synthesized with different chain length until successful attachment and RCSCO is observed or to investigate the effects of spacer length on click reaction yields or on charge transport through the multilayers. A generic structure of these modified bipyridyl ligands is shown in Figure 89.

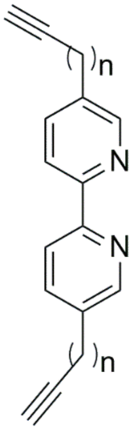

Figure 89: Generic structure of a ethynyl-functionalized bipyridine ligand with alkyl spacers of variable length.

The alkylboranes used in this reaction are commonly available in a variety of chain lengths. Presumably, longer spacers will slow charge transfer and thus there is likely a practical limit to how long these spacers can be. For this reason, spacers of 2-4 carbons should be attempted first. This is depicted in Figure 90 and would first involve the synthesis of alkyl-functionalized bipyridine ligands beginning with a Suzuki-Miyaura coupling reaction using an alkylborane featuring alkyl chains of the desire length. This could then be followed up by a reaction with 3-bromoprop-(1-yn-1-yl)trimethylsilane to add the needed ethynyl groups which could then be deprotected with potassium carbonate once the complexes have been assembled.[269]

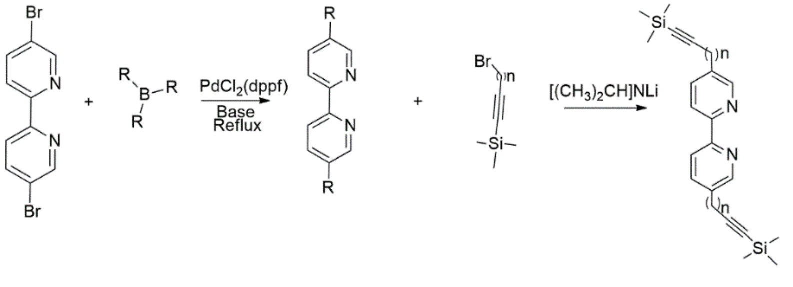

Figure 90: Reaction scheme for incorporating alkyl spacers into the bipyridne ligand.

In much the same way as the phenyl spacers making possible additional synthetic modifications, this approach offers other options as well. The inclusion of one or two double bonds in these carbon chains could confer greater rigidity to the spacer. This could be used to control multilayer packing and to maintain proper orientation of the alkyne groups if the spacers turn out to be too flexible for CuAAC reactions to take place.

4.6.2 Changes to Azide Surface Density

Packing of layer-linker strands within a multilayer may turn out to affect RCSCO behavior. This is related to the possible challenges that may be posed by the triazole linkages enforcing some kind of geometric confinement on the complexes. Steric interactions between adjacent strands could have a similar effect on RCSCO behavior. Some steric hindrance may not be entirely undesirable if it has the effect of increasing the bistability of the two spin states. This packing may be controlled by changing the density of available azide groups on the surface for complexes to reach with. SAM azide density can be easily controlled by dilution of the azide-functionalized SAM molecules with SAM-forming alkyl chains show Figure 91.

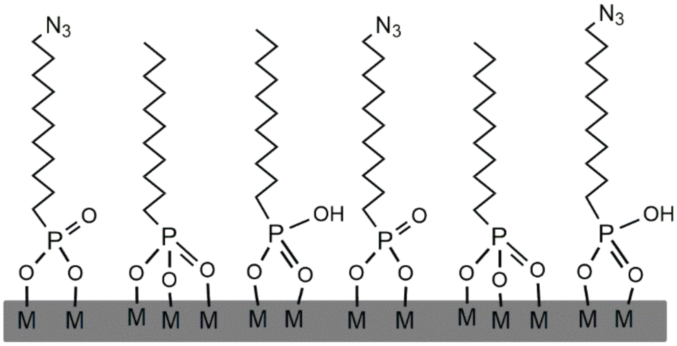

Figure 91: General schematic of 11-azdoundecylphosphonate monolayer assembled using diluent alkyl chains.

This has been done frequently in the case of thiol-based SAMs on gold,[28] and in principle there is nothing stopping this approach from being used with phosphonic acid SAMs as well. Here the 11-azidoundecylphosphonic acid would be diluted with alkyl phosphonates. These are easily available commercially owing to their use as surfactants with multiple chain lengths available. This approach would primarily address the potential problem of steric hindrance between chains of β-diketonate that might act to inhibit geometric rearrangements around the metal center. Multiple ratios of alkyl and azide chains could be tried to determine the ideal ratio. On the surface this would result in separation between azide functional groups that allow more space for the click cyclization to take place and more room for the geometric rearrangements required for RCSCO to take place. This approach may be useful if adding spacers to the bipyridyl ligand fails to produce the desired results although it is possible that a combination of approaches will be required to successfully assemble functional RCSCO multilayers. If steric interactions between adjacent strands does indeed affect redox bistability then this could also become an easy route to tuning bistability by controlling the packing of the RCSCO electrochromophores.

5. CONCLUSION

Spin crossover is a versatile phenomenon and one of the most interesting topics currently studied by inorganic and physical chemists. SCO had broad applications in computing and display technologies should scientists manage to synthesize functional molecules that can be reliably controlled at room temperature using acceptable stimulus. To date, most efforts have focused on temperature, pressure, or light-induced spin crossover. While the data from these experiments is interesting and these variations of SCO are worthy of study they suffer from several limitations. Nearly all envisioned applications for SCO materials require that the low-spin and high-spin states both exhibit stability and this behavior is typically conferred by interactions between molecules in a crystal lattice or with intercalated solvent molecules. This limitation means that SCO in the liquid phase or at an interface are rare. Furthermore, some more common spin crossover behavior like light-induced excited spin state trapping (LIESST) are only seen at very low temperatures. These factors limit the applications of current SCO materials. Less well studied varieties of spin crossover, RCSCO and CISCO, have many parallels with natural systems and allow for functionalities not seen in more conventional SCO systems.

Chapter two summarized the current state of CISCO research and sought to identify gaps that currently exist in the literature while providing a resource to scientists who want to know the current state of the field. CISCO takes advantage of differences in ligand field strength induced by different ligands to control metal spin states through reversible coordination reactions. In cobalt(III) or iron(III), coordination of a ligand induces a high-spin to low-spin transition as a result of increased field splitting induced by the new ligand. In the case of nickel(II) centers the change in coordination geometry causes a low-spin to high-spin transition. CISCO offers a route toward bistable SCO systems with much relevance to catalysis, and inorganic biochemistry.

CISCO has not garnered a much interest historically, but there is a growing body of work showcasing the efforts of scientists to design molecular machinery capable of regulating ligand binding.

The third chapter of this thesis concerned a five-coordinate cobalt salen that exhibits ligand-dependent redox-coupled spin crossover. This combined two varieties of spin crossover that are often closely linked in biological systems. In cytochrome P450 a bound water molecule keeps the heme active site locked in a low spin resting state. The bound axial water enforces a relatively large ligand field splitting energy that keeps the e_g^* orbitals out of reach of easy reduction. Once displaced, those orbitals lower in energy enough to be easily reduced by P450's redox partner allowing the catalytic cycle to go forward. We exploited a similar effect in our studies of this cobalt salen. Cobalt(II) is commonly seen in SCO research but there are few examples of CISCO. This is because cobalt(II) is a d^7 transition metal and as such will always have at least one unpaired electron no matter its coordination environment. Coupling RCSCO to CISCO here opens up an entirely new subfield of cobalt-based CISCO that has yet to be studied in detail. The high-spin cobalt(II) prefers a five-coordinate environment, but once oxidized to a high-spin d^6 the metal center will readily bind an additional ligand which enforces a low spin configuration on the metal center. Furthermore, our work shows that we can easily control the reduction potentials of the bound complex in much the same way that water and other ligands control the reduction potential of cytochromes heme group. Using a series of ligands consisting of nitrogen-containing heterocycles and a trio of anions we showed that the electrochemical irreversibility of the $Co^{II/III}$ can be easily modified by the addition of Lewis bases of increasing strength. In the case of pyridine derivatives this is easily correlated to the electron donating or withdrawing ability of the para substituent and can be readily predicted by referencing the substituent’s Hammett parameter. A more universal predictor of the reduction potential of the bound cobalt(III) is the gas phase basicity of the ligand. Like Hammett parameters this value can be easily found in literature and in cases where GPB is not already available the value can be calculated using well-established DFT methods. The largest deviations from this trend were the observed anions hydroxide, bromide, and chloride, which had significant peak splitting and did not correlate linearly with the gas phase basicity of the other ligands. This is easily explainable as all three of these anions possessed negative charges that the other ligands lacked. This negative charge introduces additional electrostatic considerations that explain the increased reduction potentials. This research represents an important first step in harnessing the CISCO and RCSCO phenomenon to create tunable spin switches from cobalt coordination complexes.

Future directions of research concerning related salens may consist first of constructing multilayer films on ITO coated glass or a suitable gold substrate. Preliminary attempts at multilayer growth using a salen functionalized with ethynyl groups at the R_2 position were unsuccessful. Difficulties finding a suitable solvent in which these complexes were soluble was a challenge, although it is possible that impurities in the sample were to blame. Reattempting this synthesis to confirm if solubility was indeed the main problem is probably worthwhile. If solubility was indeed the issue it may be addressed by further synthetic modifications at the R_1 or R_2 positions. However, it is possible that further modification of these positions will change the complex’s electrochemistry.

Incorporation into multilayers offers several challenges as well. The structural rearrangements involved in **CoSln**$^{+}$’s RCSCO process may be hindered by confinement in the multilayer structure, in which case synthetic modifications similar to those described for the β-diketonates in Chapter 4 might be considered. Another challenge could arise from interactions between bound **CoSln**$^+$ and unreacted azides on the surface. Observations of preliminary monolayer electrochemistry would seem to indicate that this is a possibility as well as literature data from similar interactions involving cobalt porphyrins attached to an electrode surface.[149] This could be addressed by a decrease in azide surface density. This approach is elaborated on in Chapter 4 in the context of β-diketonate multilayers.

An alternate route to further exploration of ligand-dependent RCSCO in **CoSln**$^+$ involves additional solution studies using salen ligands modified at the R_1 position to incorporate proximal ligands. This approach is common in the CISCO literature, examples of which can be found in Chapter 2. This would offer an interesting way to design electrochemically controlled molecular switches and motors. It would also remove the need to have free ligand present in solution. This could be an advantage in constructing multilayers if ligand penetration of the multilayers proves difficult.

Finally, chapter four detailed our attempts to grow multilayers of RCSCO active cobalt diektonate complexes. This research was informed by our group's past success with building functional multilayers of azide-functionalized gold and ITO glass substrates. Ultimately these efforts were unsuccessful but the results we obtained give us several paths forward for future work. The RCSCO that these complexes showed in solution and the drastic spectral changes observed upon oxidation made these complexes promising candidates for electrochromic multilayers assembled using CuAAC cycloadditions. However, evidence of layer growth on ITO was dubious and surface RCSCO was not observed. The reasons for this are likely due to steric hindrance caused by the proximity of R-groups on the β-diketonate ligands interfering with the CuAAC cyclization intermediates. Fortunately, there are multiple synthetic routes and procedural changes that may address this problem in the future. These include extra synthetic steps in the synthesis of the bipyridyl ligands to introduce more flexible spacers expected to better accommodate the click reaction's intermediates and changes to the SAM procedure to allow more space chains to electrophores to remove the steric influence of adjacent molecules.

There are multiple paths forward concerning both the five-coordinate cobalt salen and the cobalt β-diketonates presented here. Both of these complexes offer numerous paths forward ranging from fundamental solution electrochemical studies to proof-of-concept functional electromic multilayers and molecular machines. Interest in SCO materials is growing with many new examples of CISCO published in the last decade. There are still many gaps in the literature and new angles to explore. Both RCSCO and CISCO receive less attention than other SCO mechanisms and any work done in this area has the potential to shape the development of these growing fields.

Numerous synthetic pathways are likewise possible for the β-diketonate complexes. Most of these involve synthetic modifications to impart additional flexibility to the bipyridyl ethynyl group to facilitate multilayer formation. That said, there are still ample room for solution studies. While Harding et al. have already studied the electrochemistry and crystal structures of a series of related β-diketonate complexes they did not establish a firm relationship between the nature of the β-diketonate R-groups and the RCSCO behavior of the related complexes. Failure to detect a high-spin cobalt(III) intermediate in the case of $Co(dbm)_2((CC)_2bpy)$ natural inspires questions about the nature of this intermediate and how bipyridyl structure influences its lifetimes. Solution electrochemical studies of a series of related complexes with different bipyridyl ligands could uncover interesting trends here. The apparent dependence on β-diketonate R-groups in these interactions could also be worthy of further study.

REFERENCES

1. Allouhi, A.; Fouih, Y. El; Kousksou, T.; Jamil, A.; Zeraouli, Y.; Mourad, Y. Energy Consumption and Efficiency in Buildings: Current Status and Future Trends. *J. Clean. Prod.* **2015**, *109*, 118–130. DOI: 10.1016/j.jclepro.2015.05.139
2. Pérez-Lombard, L.; Ortiz, J.; Pout, C. A Review on Buildings Energy Consumption Information. *Energy Build.* **2008**, *40*, 394–398. DOI: 10.1016/j.enbuild.2007.03.007
3. Lee, E. S.; Yazdanian, M.; Selkowitz, S. E. *The Energy-Savings Potential of Electrochromic Windows in the US Commercial Buildings Sector*; LBNL-54966; Lawrence Berkeley National Laboratory: Berkeley, 2004; 1-42.
4. Mardare, C. C.; Hassel, A. W. Review on the Versatility of Tungsten Oxide Coatings. *Phys. Stat. Sol. A* **2019**, *216* (12). DOI: 10.1002/PSSA.201900047
5. *OnePlus Concept One at CES 2020: Cameras "disappear" with special glass* - CNET. https://www.cnet.com/news/oneplus-concept-ones-disappearing-camera-is-mostly-a-gimmick/ (accessed 2020-01-09).
6. Gu, C.; Jia, A. B.; Zhang, Y. M.; Zhang, S. X. A. Emerging Electrochromic Materials and Devices for Future Displays. *Chem. Rev.* **2022**, *122* (18), 14679–14721. DOI: 10.1021/ACS.CHEMREV.1C01055
7. Azens, A.; Granqvist, C. G. Electrochromic Smart Windows: Energy Efficiency and Device Aspects. *J. Solid State Electr.* **2003**, *7* (2), 64–68. DOI: 10.1007/s10008-002-0313-4
8. Mortimer, R. J. Electrochromic Materials. *Annu. Rev. Mater Res.* **2011**, *41*, 241–268. DOI: 10.1146/annurev-matsci-062910-100344
9. Rosseinsky, D. R.; Mortimer, R. J. Electrochromic Systems and the Prospects for Devices. *Adv. Mater.* **2001**, *13* (11), 783–793. DOI: 10.1002/1521-4095(200106)13:11<783::AID-ADMA783>3.0.CO;2-D
10. Madasamy, K.; Velayutham, D.; Suryanarayanan, V.; Kathiresan, M.; Ho, K.-C. Viologen-Based Electrochromic Materials and Devices. *J. Mater. Chem. C* **2019**, *7*, 4622–4637. DOI: 10.1039/c9tc00416e
11. Nadeau, J. M.; Swager, T. M. New β-Linked Pyrrole Monomers: Approaches to Highly Stable and Conductive Electrochromic Polymers. *Tetrahedron* **2004**, *60*, 7141–7146. DOI: 10.1016/j.tet.2004.06.016
12. Gül, E.; Ergun, C.; Carbas, B. B. Electrochromic Copolymers of 2,5-Dithienyl-N-Substituted-Pyrrole (SNS) Derivatives with EDOT: Properties and Electrochromic Device Applications. *Mater. Today Comm.* **2022**, *32*, 103888. DOI: 10.1016/j.mtcomm.2022.103888
13. Halder, S.; Roy, S.; Chakraborty, C. Multicolored and Durable Electrochromism in Water Soluble Naphthalene and Perylene Based Diimides. *Sol. Energy Mater. Sol. Cells* **2021**, *234*, 111429. DOI: 10.1016/j.solmat.2021.111429
14. Lv, X.; Zha, L.; Qian, L.; Xu, X.; Bi, Q.; Xu, Z.; Wright, D. S.; Zhang, C. Controllable Fabrication of Perylene Bisimide Self-Assembled Film and Patterned All-Solid-State Electrochromic Device. *Chem. Eng. J.* **2019**, *386*, 123939. DOI: 10.1016/j.cej.2019.123939
15. Shankar, S.; Lahav, M.; van der Boom, M. E. Coordination-Based Molecular Assemblies as Electrochromic Materials: Ultra-High Switching Stability and Coloration Efficiencies. *J. Am. Chem. Soc.* **2015**, *137* (12), 4050–4053. DOI: 10.1021/jacs.5b00429

16. Richardson, J. J.; Cui, J.; Björnmalm, M.; Braunger, J. A.; Ejima, H.; Caruso, F. Innovation in Layer-by-Layer Assembly. *Chem. Rev.* **2016**, 116 (23), 14828–14867. DOI: 10.1021/acs.chemrev.6b00627
17. Zhang, X.; Chen, H.; Zhang, H. Layer-by-Layer Assembly: From Conventional to Unconventional Methods. *Chem. Comm.* **2007**, *14*, 1395–1405. DOI: 10.1039/b615590a
18. Ariga, K.; Hill, J. P.; Ji, Q. Layer-by-Layer Assembly as a Versatile Bottom-up Nanofabrication Technique for Exploratory Research and Realistic Application. *PhysChemChemPhys.* **2007**, *9* (19), 2319–2340. DOI: 10.1039/b700410a
19. Lipton, J.; Weng, G.-M.; Röhr, J. A.; Wang, H.; Taylor, A. D. Layer-by-Layer Assembly of Two-Dimensional Materials: Meticulous Control on the Nanoscale. *Matter* **2020**, 2 (5), 1148–1165. DOI: 10.1016/j.matt.2020.03.012
20. Ulman, A. Formation and Structure of Self-Assembled Monolayers. *Chem. Rev.* **1996**, *96* (4), 1533–1554. DOI: 10.1021/cr9502357
21. Love, J. C.; Estroff, L. A.; Kriebel, J. K.; Nuzzo, R. G.; Whitesides, G. M. Self-Assembled Monolayers of Thiolates on Metals as a Form of Nanotechnology. *Chem. Rev.* **2005**, *105* (4), 1103–1170. DOI: 10.1021/cr0300789
22. Vericat, C.; Vela, M. E.; Benitez, G.; Carro, P.; Salvarezza, R. C. Self-Assembled Monolayers of Thiols and Dithiols on Gold: New Challenges for a Well-Known System. *Chem. Soc. Rev.* **2010**, *39*, 1805–1834. DOI: 10.1039/b907301a
23. Ganesh, V.; Kumar Pal, S.; Kumar, S.; Lakshminarayanan, V. Self-Assembled Monolayers (SAMs) of Alkoxycyanobiphenyl Thiols on Gold-A Study of Electron Transfer Reaction Using Cyclic Voltammetry and Electrochemical Impedance Spectroscopy. *J. Colloid. Interface Sci.* **2006**, *296* (1), 195–203. DOI: .1016/j.jcis.2005.08.051
24. Kaur, I.; Zhao, X.; Bryce, M. R.; Schauer, P. A.; Low, P. J.; Kataky, R. Modification of Electrode Surfaces by Self-Assembled Monolayers of Thiol-Terminated Oligo(Phenyleneethynylene)s. *ChemPhysChem* **2013**, *14* (2), 431–440. DOI: 10.1002/CPHC.201200744
25. Kellon, J. E.; Young, S. L.; Hutchison, J. E. Engineering the Nanoparticle−Electrode Interface. *Chem. Mater.* **2019**, *31*, 2685–2701. DOI: 10.1021/acs.chemmater.8b04977
26. Chidsey, C. E. D. Free Energy and Temperature Dependence of Electron Transfer at the Metal-Electrolyte Interface. *Science* **1991**, *251* (4996), 919–922. DOI: 10.1126/science.251.4996.919
27. Bandyopadhyay, S.; Rana, A.; Mittra, K.; Samanta, S.; Sengupta, K.; Dey, A. Effect of Axial Ligand, Spin State, and Hydrogen Bonding on the Inner-Sphere Reorganization Energies of Functional Models of Cytochrome P450. *Inorg. Chem.* **2014**, *53* (19), 10150–10158. DOI: 10.1021/ic501112a
28. Collman, J. P.; Devaraj, N. K.; Eberspacher, T. P. A.; Chidsey, C. E. D. D. Mixed Azide-Terminated Monolayers: A Platform for Modifying Electrode Surfaces. *Langmuir* **2006**, *22* (6), 2457–2464. DOI: 10.1021/la052947q
29. Palomaki, P. K. B. B.; Dinolfo, P. H. A Versatile Molecular Layer-by-Layer Thin Film Fabrication Technique Utilizing Copper(I)-Catalyzed Azide-Alkyne Cycloaddition. *Langmuir* **2010**, *26* (12), 9677–9685. DOI: 10.1021/la100308j
30. Civic, M. R.; Dinolfo, P. H. Electrochemical Rectification of Redox Mediators Using Porphyrin-Based Molecular Multilayered Films on ITO Electrodes. *ACS Appl. Mater. Interfaces* **2016**, *8* (31), 20465–20473. DOI: 10.1021/acsami.6b05643

31. Palomaki, P. K. B.; Dinolfo, P. H. Structural Analysis of Porphyrin Multilayer Films on ITO Assembled Using Copper(I)-Catalyzed Azide-Alkyne Cycloaddition by ATR IR. *ACS Appl. Mater. Interfaces* **2011**, *3* (12), 4703–4713. DOI: 10.1021/am201125p
32. Gardner, T. J.; Frisbie, C. D.; Wrighton, M. S. Systems for Orthogonal Self-Assembly of Electroactive Monolayers on Au and ITO: An Approach to Molecular Electronics. *J. Am. Chem. Soc.* **1995**, *117* (26), 6927–6933. DOI: 10.1021/ja00131a015
33. Hotchkiss, P. J.; Jones, S. C.; Paniagua, S. A.; Sharma, A.; Kippelen, B.; Armstrong, N. R.; Marder, S. R. The Modification of Indium Tin Oxide with Phosphonic Acids: Mechanism of Binding, Tuning of Surface Properties, and Potential for Use in Organic Electronic Applications Modification of ITO with Phosphonic Acids. *Acc. Chem. Res.* **2012**, *45* (3), 337–346. DOI: 10.1021/ar200119g
34. Gawalt, E. S.; Lu, G.; Bernasek, S. L.; Schwartz, J. Enhanced Bonding of Alkanephosphonic Acids to Oxidized Titanium Using Surface-Bound Alkoxyzirconium Complex Interfaces. *Langmuir* **1999**, *15* (26), 8929–8933. DOI: 10.1021/la990906m
35. Zhao, W.; Chang, T.; Leygraf, C.; Johnson, M. Corrosion Inhibition of Copper with Octadecylphosphonic Acid (ODPA) in a Simulated Indoor Atmospheric Environment. *Corros. Sci.* **2021**, *192*, 109777. DOI: 10.1016/j.corsci.2021.109777
36. Acton, O.; Dubey, M.; Weidner, T.; O'Malley, K. M.; Kim, T. W.; Ting, G. G.; Hutchins, D.; Baio, J. E.; Lovejoy, T. C.; Gage, A. H.; Castner, D. G.; Ma, H.; Jen, A. K. Y. Simultaneous Modification of Bottom-Contact Electrode and Dielectric Surfaces for Organic Thin-Film Transistors through Single-Component Spin-Cast Monolayers. *Adv. Funct. Mater.* **2011**, *21* (8), 1476–1488. DOI: 10.1002/ADFM.201002035
37. Khramov, A. N.; Balbyshev, V. N.; Kasten, L. S.; Mantz, R. A. Sol-Gel Coatings with Phosphonate Functionalities for Surface Modification of Magnesium Alloys. *Thin Solid Films* **2006**, *514* (1-2), 174–181. DOI: 10.1016/j.tsf.2006.02.023
38. Touir, R.; Dkhireche, N.; Touhami, M. E.; Sfaira, M.; Senhaji, O.; Robin, J. J.; Boutevin, B.; Cherkaoui, M. Study of Phosphonate Addition and Hydrodynamic Conditions on Ordinary Steel Corrosion Inhibition in Simulated Cooling Water. *Mater. Chem. Phys.* **2010**, *122* (1), 1–9. DOI: 10.1016/j.matchemphys.2010.02.063
39. Guerrero, G.; Alauzun, J. G.; Granier, M.; Laurencin, D.; Mutin, P. H. Phosphonate Coupling Molecules for the Control of Surface/Interface Properties and the Synthesis of Nanomaterials. *Dalton Trans.* **2013**, *42*, 12569–12585. DOI: 10.1039/c3dt51193f
40. Bousseksou, A.; Molnár, G.; Salmon, L.; Nicolazzi, W. Molecular Spin Crossover Phenomenon: Recent Achievements and Prospects. *Chem. Soc. Rev.* **2011**, *40*, 3313–3335. DOI: 10.1039/c1cs15042a
41. Halcrow, M. A. The Foundation of Modern Spin-Crossover. *Chem. Comm.* **2013**, *49* (93), 10890–10892. DOI: 10.1039/c3cc44171g
42. Gütlich, P.; Goodwin, H. A. *Spin Crossover in Transition Metal Compounds II*; Springer, 2004.
43. Real, J. A.; Gaspar, A. B.; Carmen Muñoz, M. Thermal, Pressure and Light Switchable Spin-Crossover Materials. *Dalton Trans.* **2005**, 2062–2079. DOI: 10.1039/b501491c.
44. Miessler, G. L.; Fischer, P. J.; Tarr, D. A. *Inorganic Chemistry*, 5th ed.; Pearson Education, 2014.
45. Muñoz, M. C.; Real, J. A. Thermo-, Piezo-, Photo- and Chemo-Switchable Spin Crossover Iron(II)-Metallocyanate Based Coordination Polymers. *Coord. Chem. Rev.* **2011**, *225* (17-18) 2068–2093. DOI: 10.1016/j.ccr.2011.02.004

46. Halcrow, M. A. Trapping and Manipulating Excited Spin States of Transition Metal Compounds. *Chem. Soc. Rev.* **2008**, *37*, 278–289. DOI: 10.1039/b701085k
47. Kochem, A.; Kanso, H.; Baptiste, B.; Arora, H.; Philouze, C.; Jarjayes, O.; Vezin, H.; Luneau, D.; Orio, M.; Thomas, F. Ligand Contributions to the Electronic Structures of the Oxidized Cobalt(II) Salen Complexes. *Inorg. Chem.* **2012**, *51* (20), 10557–10571. DOI: 10.1021/ic300763t
48. Halcrow, M. A. Structure:Function Relationships in Molecular Spin-Crossover Complexes. *Chem. Soc. Rev* **2011**, *40*, 4119–4142. DOI: 10.1039/c1cs15046d
49. Kershaw Cook, L. J.; Kulmaczewski, R.; Mohammed, R.; Dudley, S.; Barrett, S. A.; Little, M. A.; Deeth, R. J.; Halcrow, M. A. A Unified Treatment of the Relationship Between Ligand Substituents and Spin State in a Family of Iron(II) Complexes. *Angew. Chem.* **2016**, *128* (13), 4399–4403. DOI: 10.1002/ange.201600165
50. Li, J.-Y.; He, C.-T.; Chen, Y.-C.; Zhang, Z.-M.; Liu, W.; Ni, Z.-P.; Tong, M.-L. Tunable Cooperativity in a Spin-Crossover Hoffman-like Metal-Organic Framework Material by Aromatic Guests. *J. Mater. Chem. C Mater.* **2015**, *3*, 7830-7835. DOI: 10.1039/C5TC00432B
51. Piñeiro-López, L.; Valverde-Muñoz, F. J.; Seredyuk, M.; Muñoz, M. C.; Haukka, M.; Real, J. A. Guest Induced Strong Cooperative One- and Two-Step Spin Transitions in Highly Porous Iron(II) Hofmann-Type Metal-Organic Frameworks. *Inorg. Chem.* **2017**, *56* (12), 7038–7047. DOI: 10.1021/acs.inorgchem.7b00639
52. Valverde-Muñoz, F. J.; Bartual-Murgui, C.; Piñeiro-López, L.; Muñoz, M. C.; Real, J. A. Influence of Host-Guest and Host-Host Interactions on the Spin-Crossover 3D Hofmann-Type Clathrates $\{Fe^{II}(Pina)[M^I(CN)_2]_2\} \cdot$ XMeOH (M^I = Ag, Au). *Inorg. Chem.* **2019**, *58* (15), 10038–10046. DOI: 10.1021/acs.inorgchem.9b01189
53. Mondal, D. J.; Roy, S.; Yadav, J.; Zeller, M.; Konar, S. Solvent-Induced Reversible Spin-Crossover in a 3D Hofmann-Type Coordination Polymer and Unusual Enhancement of the Lattice Cooperativity at the Desolvated State. *Inorg. Chem.* **2020**, *59* (18), 13024–13028. DOI: 10.1021/acs.inorgchem.0c02240
54. Brennan, A. T.; Zenere, K. A.; Brand, H. E. A. A.; Price, J. R.; Bhadbhade, M. M.; Turner, G. F.; Moggach, S. A.; Valverde-Muñoz, F. J.; Real, J. A.; Clegg, J. K.; et al. Guest Removal and External Pressure Variation Induce Spin Crossover in Halogen-Functionalized 2-d Hofmann Frameworks. *Inorg. Chem.* **2020**, *59* (19), 14296–14305. DOI: 10.1021/acs.inorgchem.0c02092
55. Zenere, K. A.; Duyker, S. G.; Trzop, E.; Collet, E.; Chan, B.; Doheny, P. W.; Kepert, C. J.; Neville, S. M. Increasing Spin Crossover Cooperativity in 2D Hofmann-Type Materials with Guest Molecule Removal. *Chem. Sci.* **2018**, *9* (25), 5623–5629. DOI: 10.1039/c8sc01040d
56. Kahn, O.; Jay Martinez, C. Spin-Transition Polymers: From Molecular Materials Toward Memory Devices. *Science* **1998**, *279*, 44–48.
57. Magri, G.; Folli, A.; Murphy, D. M. Monitoring the Substrate-Induced Spin-State Distribution in a Cobalt(II)-Salen Complex by EPR and DFT. *Eur. J. Inorg. Chem.* **2022**, *2022* (9), 202101071. DOI: 10.1002/ejic.202101071
58. Thies, S.; Bornholdt, C.; Köhler, F.; Sönnichsen, F. D.; Näther, C.; Tuczek, F.; Herges, R. Coordination-Induced Spin Crossover (CISCO) through Axial Bonding of Substituted Pyridines to Nickel-Porphyrins: σ-Donor versus π-Acceptor Effects. *Chem. Eur. J.* **2010**, *16* (33), 10074–10083. DOI: 10.1002/chem.201000603
59. Lada, Z. G. The Investigation of Spin-Crossover Systems by Raman Spectroscopy: A Review. *Magnetochemistry* **2022**, *8* (9), 108. DOI: 10.3390/magnetochemistry8090108

60. Brooker, S. Spin Crossover with Thermal Hysteresis: Practicalities and Lessons Learnt. *Chem. Soc. Rev.* **2015**, *44* (10), 2880–2892. DOI: 10.1039/c4cs00376d
61. Létard, J.-F.; Guionneau, P.; Goux-Capes, L. Towards Spin Crossover Applications. In *Spin Crossover in Transition Metal Compounds III*; Springer, 2006; pp 221–249.
62. Luo, X.; Zaitoon, A.; Lim, L. T. A Review on Colorimetric Indicators for Monitoring Product Freshness in Intelligent Food Packaging: Indicator Dyes, Preparation Methods, and Applications. *Compr. Rev. Food Sci. Food Saf.* **2022**, 21 (3), 2489–2519. DOI: 10.1111/1541-4337.12942
63. Khusniyarov, M. M. How to Switch Spin-Crossover Metal Complexes at Constant Room Temperature. *Chem. Eur. J.***2016**, *22* (43), 15178–15191. DOI: 10.1002/CHEM.201601140
64. Elgrishi, N.; Rountree, K. J.; McCarthy, B. D.; Rountree, E. S.; Eisenhart, T. T.; Dempsey, J. L. A Practical Beginner's Guide to Cyclic Voltammetry. *J. Chem. Educ.* **2018**, *95* (2), 197–206. DOI: 10.1021/acs.jchemed.7b00361
65. Bard, A. J.; Faulkner, L. R. *Electrochemical Methods Fundamentals and Applications*, 2nd ed.; John Wiley & Sons, Inc., 2001.
66. Turner, J. W.; Schultz, F. A. Coupled Electron-Transfer and Spin-Exchange Reactions. *Coord. Chem. Rev.* **2001**, *219–221*, 81–97. DOI: 10.1016/S0010-8545(01)00322-8
67. Guengerich, F. P. Mechanisms of Cytochrome P450-Catalyzed Oxidations. *ACS Catal.* **2018**, 8 (12), 10964–10976. DOI: 10.1021/acscatal.8b03401
68. Conner, K. P.; Woods, C. M.; Atkins, W. M. Interactions of Cytochrome P450s with Their Ligands. *Arch. Biochem. Biophys.* **2011**, *507* (1), 56–65. DOI: 10.1016/j.abb.2010.10.006
69. Collman, J. P.; Gagne, R. R.; Reed, C. A.; Halbert, T. R.; Lang, G.; Robinsonlc, W. T. "Picket Fence Porphyrins." Synthetic Models for Oxygen Binding Hemoproteins. *J. Am. Chem. Soc.* **1975**, *97* (6), 1427–1439. DOI: 10.1021/ja00839a026
70. Peters, M. K.; Hamer, S.; Jäkel, T.; Röhricht, F.; Sönnichsen, F. D.; Von Essen, C.; Lahtinen, M.; Naether, C.; Rissanen, K.; Herges, R. Spin Switching with Triazolate-Strapped Ferrous Porphyrins. *Inorg. Chem.* **2019**, *58* (8), 5265–5272. DOI: 10.1021/acs.inorgchem.9b00349
71. Weyermann, P.; Diederich, F. Dendritic Iron Porphyrins with a Tethered Axial Ligand as New Model Compounds for Heme Monooxygenases. *Helv. Chim. Acta* **2002**, *85* (2), 599–617. DOI: 10.1002/1522-2675(200202)85:2<599::AID-HLCA599>3.0.CO;2-V
72. Brown, K. L. Chemistry and Enzymology of Vitamin B 12. *Chem. Rev.* **2005**, *105* (6), 2075–2149. DOI: 10.1021/cr030720z
73. Sowmya, S.; Vijaikanth, V. Electrochemistry and Electrocatalytic Activity of Cobaloxime Complexes. *ChemistrySelect* **2022**, *7* (10), 1–18. DOI: 10.1002/SLCT.202104044
74. Geselowitz, D. A. Is Hexaamminecobalt(III/II) Electron Self-Exchange Spin-Forbidden? Photochemical Processes Analogy to Photochemical Processes. *Inorg. Chim. Acta* **1988**, *154* (2), 225–228. DOI: 10.1016/S0020-1693(00)90140-3
75. Larsson, S.; Ståhl, K.; Zerner, M. C. Hexaamminecobalt Electron-Self-Exchange Reaction. *Inorg. Chem.* **1986**, *25* (17), 3033–3037. DOI: 10.1021/ic00237a022
76. Newton, M. D. The $Co(NH_3)_6^{2+/3+}$ Exchange Reaction: Ground-State versus Thermally Excited Pathways. *J. Phys. Chem.* **1991**, *95* (1), 30–38. DOI: 10.1021/j100154a010
77. Creaser, I. I.; Sargeson, A. M.; Zanella, A. W. Outer-Sphere Electron-Transfer Reactions Involving Caged Cobalt Ions. *Inorg. Chem.* **1983**, *22* (26), 4022–4029. DOI: 10.1021/ic00168a041

78. Shalders, R. D.; Swaddle, T. W. The Ligand Cage Effect in Volumes of Activation for Electron Transfer Reactions of Cobalt(III/II) Complexes in Aqueous Solution. *Inorg. Chem.* **1995**, *34* (19), 4815–4820. DOI: 10.1021/ic00123a015
79. Harding, P.; Harding, D. J.; Daengngern, R.; Thurakitsaree, T.; Schutte, B. M.; Shaw, M. J.; Tantirungrotechai, Y. Redox Coupled-Spin Crossover in Cobalt β-Diketonate Complexes: Structural, Electrochemical and Computational Studies. *Polyhedron* **2012**, *42* (1), 291–301. DOI: 10.1016/j.poly.2012.05.037
80. Gütlich, P.; Goodwin, H. A. Spin Crossover-An Overall Perspective. In *Spin Crossover in Transition Metal Compounds I;* Springer, 2004; pp 1–47.
81. Li, H.; Peng, H. Recent Advances in Self-Assembly of Spin Crossover Materials and Their Applications. *Curr. Op. Colloid. Inter. Sci.* **2018**, *35*, 9–16. DOI: 10.1016/j.cocis.2017.12.007
82. Olguín, J. Unusual Metal Centres/Coordination Spheres in Spin Crossover Compounds. *Coord. Chem. Rev.* **2020**, *407*, 213148. DOI: 10.1016/j.ccr.2019.2131483
83. Zhang, X.; Mu, S.; Chastanet, G.; Daro, N.; Palamarciuc, T.; Rosa, P.; Létard, J. F.; Liu, J.; Sterbinsky, G. E.; Arena, D. A.; Etrillard, C.; Kundys, B.; Doudin, B.; Dowben, P. A. Complexities in the Molecular Spin Crossover Transition. *J. Phys. Chem. C* **2015**, *119* (28), 16293–16302. DOI: 10.1021/acs.jpcc.5b02220
84. Senthil Kumar, K.; Bayeh, Y.; Gebretsadik, T.; Elemo, F.; Gebrezgiabher, M.; Thomas, M.; Ruben, M. Spin-Crossover in Iron(II)-Schiff Base Complexes. *Dalton Trans.* **2019**, *48*, 15321–15337. DOI: 10.1039/c9dt02085c
85. Wolf, S. A.; Awschalom, D. D.; Buhrman, R. A.; Daughton, J. M.; Von Molnár, S.; Roukes, M. L.; Chtchelkanova, A. Y.; Treger, D. M. Spintronics: A Spin-Based Electronics Vision for the Future. *R. Allenspach, J. Magn. Magn. Mat.* **1993**, *294* (5546), 1488–1495.
86. Meng, Y. S.; Liu, T. Manipulating Spin Transition to Achieve Switchable Multifunctions. *Acc. Chem. Res.* **2019**, *52* (5), 1369–1379. DOI: 10.1021/acs.accounts.9b00049
87. Gamez, P.; Costa, J. S.; Quesada, M.; Aromí, G. Iron Spin-Crossover Compounds: From Fundamental Studies to Practical Applications. *Dalton Trans.* **2009**, *38*, 7845–7853. DOI: 10.1039/b908208e
88. Weiss, R.; Gold, A.; Terner, J. Cytochromes C′: Biological Models for the S = 3/2,5/2 Spin-State Admixture? *Chem. Rev.* **2006**, 106 (6), 2550–2579. DOI: 10.1021/cr040416l
89. Franzen, S. Spin-Dependent Mechanism for Diatomic Ligand Binding to Heme. *Proc. Natl. Acad. Sci.* **2002**, *99* (26), 16754–16759. DOI: 10.1073/PNAS.252590999
90. Murphy, M. J.; Zenere, K. A.; Ragon, F.; Southon, P. D.; Kepert, C. J.; Neville, S. M. Guest Programmable Multistep Spin Crossover in a Porous 2-D Hofmann-Type Material. *J. Am. Chem. Soc.* **2017**, *139* (3), 1330–1335. DOI: 10.1021/jacs.6b12465
91. Zhang, C. J.; Lian, K. T.; Huang, G. Z.; Bala, S.; Ni, Z. P.; Tong, M. L. Hysteretic Four-Step Spin-Crossover in a 3D Hofmann-Type Metal-Organic Framework with Aromatic Guest. *Chem. Comm.* **2019**, *55* (74), 11033–11036. DOI: 10.1039/c9cc06017k
92. Halcrow, M. A. Spin-Crossover Compounds with Wide Thermal Hysteresis. *Chem. Lett.* **2014**, *43* (8), 1178-1188. DOI: 10.1246/cl.140464
93. Martinho, P. N.; Ortin, Y.; Gildea, B.; Gandolfi, C.; Mckerr, G.; O’hagan, B.; Albrecht, M.; Morgan, G. G. Inducing Hysteretic Spin Crossover in Solution. *Dalton Trans.* **2012**, *41*, 7461–7463. DOI: 10.1039/c2dt12036d
94. Achey, D.; Meyer, G. J. Ligand Coordination and Spin Crossover in a Nickel Porphyrin Anchored to Mesoporous TiO2 Thin Films. *Inorg. Chem.* **2013**, *52* (16), 9574–9582. DOI: 10.1021/ic401286a

95. Köbke, A.; Gutzeit, F.; Röhricht, F.; Schlimm, A.; Grunwald, J.; Tuczek, F.; Studniarek, M.; Longo, D.; Choueikani, F.; Otero, E.; et al. Reversible Coordination-Induced Spin-State Switching in Complexes on Metal Surfaces. *Nat. Nanotechnol.* **2020**, *15* (1), 18–21. DOI: 10.1038/s41565-019-0594-8
96. Dommaschk, M.; Gutzeit, F.; Boretius, S.; Haag, R.; Herges, R. Coordination-Induced Spin-State-Switch (CISSS) in Water. *Chem. Comm.* **2014**, *50*, 12476. DOI: 10.1039/c4cc05525j
97. Armstrong, F. A.; Hill, H. A. O.; Walton, N. J. Direct Electrochemistry of Redox Proteins. *Acc. Chem. Res.* **1988**, *21* (11), 407–413. DOI: 10.1021/ar00155a004
98. Blackman, A. G. Cobalt: Inorganic & Coordination Chemistry. In *Encyclopedia of Inorganic Chemistry*; Scott, R. A., Atwood, D., Lukehart, C. M., Crabtree, R. H., Bruce King, R., Eds.; Wiley, 2005; pp 817–841. DOI: 10.1002/0470862106
99. Sligar, S. G. Coupling of Spin, Substrate, and Redox Equilibriums in Cytochrome P450. *Biochemistry* **1976**, *15* (24), 5399–5406. DOI: 10.1021/bi00669a029
100. Liu, J.; Chakraborty, S.; Hosseinzadeh, P.; Yu, Y.; Tian, S.; Petrik, I.; Bhagi, A.; Lu, Y. Metalloproteins Containing Cytochrome, Iron-Sulfur, or Copper Redox Centers. *Chem. Rev.* **2014**, *114* (8), 4366–4369. DOI: 10.1021/cr400479b
101. Poulos, T. L.; Follmer, A. H. Updating the Paradigm: Redox Partner Binding and Conformational Dynamics in Cytochromes P450. *Acc. Chem. Res.* **2022**, *55* (3), 373–380. DOI: 10.1021/acs.accounts.1c00632
102. Bertini, I.; Cavallaro, G.; Rosato, A. Cytochrome c: Occurrence and Functions. *Chem. Rev.* **2006**, *106* (1), 90–115. DOI: 10.1021/cr050241v
103. Denisov, I. G.; Makris, T. M.; Sligar, S. G.; Schlichting, I. Structure and Chemistry of Cytochrome P450. *Chem. Rev.* **2005**, *105* (6), 2253–2277. DOI: 10.1021/cr0307143
104. Yoshikawa, S.; Shimada, A. Reaction Mechanism of Cytochrome c Oxidase. *Chem. Rev.* **2015**, 115 (4), 1936–1989. DOI: 10.1021/cr500266a
105. Seyedi, S. S.; Waskasi, M. M.; Matyushov, D. V. Theory and Electrochemistry of Cytochrome c. *J. Phys. Chem. B* **2017**, *121* (19), 4958-4967. DOI: 10.1021/acs.jpcb.7b00917
106. Collman, J. P.; Boulatov, R.; Sunderland, C. J.; Fu, L. Functional Analogues of Cytochrome c Oxidase, Myoglobin, and Hemoglobin. *Chem. Rev.* **2004**, *104* (2), 561–588. DOI: 10.1021/cr0206059
107. Alvarez-Paggi, D.; Hannibal, L.; Castro, M. A.; Oviedo-Rouco, S.; Demicheli, V.; Tórtora, V.; Tomasina, F.; Radi, R.; Murgida, D. H. Multifunctional Cytochrome c: Learning New Tricks from an Old Dog. *Chem. Rev.* **2017**, *117* (21), 13382–13460. DOI: 10.1021/acs.chemrev.7b00257
108. Senge, M. O.; Sergeeva, N. N.; Hale, K. J. Classic Highlights in Porphyrin and Porphyrinoid Total Synthesis and Biosynthesis. *Chem. Soc. Rev.* **2021**, *50*, 4730–4789. DOI: 10.1039/c7cs00719a
109. Sessler, J. L.; Seidel, D. Synthetic Expanded Porphyrin Chemistry. *Angew. Chem. Int. Ed.*, **2003**, *42*, 5134–5175. DOI: 10.1002/anie.200200561
110. Harris, D.; Loew, G. Determinants of the Spin State of the Resting State of Cytochrome P450cam. *J. Am. Chem. Soc.* **1993**, *115* (19), 8775–8779. DOI: 10.1021/ja00072a034
111. Battistuzzi, G.; Borsari, M.; Cowan, J. A.; Ranieri, A.; Sola, M. Control of Cytochrome c Redox Potential: Axial Ligation and Protein Environment Effects. *J. Am. Chem. Soc.* **2002**, *124* (19), 5315–5324. DOI: 10.1021/ja017479v

112. Ye, T.; Kaur, R.; Wen, X.; Bren, K. L.; Elliott, S. J. Redox Properties of Wild-Type and Heme-Binding Loop Mutants of Bacterial Cytochromes c Measured by Direct Electrochemistry. *Inorg. Chem.* **2005**, *44* (24), 8999–9006. DOI: 10.1021/ic051003l
113. Raag, R.; Poulos, T. L. The Structural Basis for Substrate-Induced Changes in Redox Potential and Spin Equilibrium in Cytochrome P-450CAM. *Biochemistry* **1989**, *28* (2), 917–922. DOI: 10.1021/bi00428a077
114. Neves Cruz, J.; Santana de Oliveira, M.; Silva, G.; Pedro da Silva Souza Filho, A.; Santiago Pereira, D.; Henrique Lima Lima, A.; Helena de Aguiar Andrade, E. Insight into the Interaction Mechanism of Nicotine, NNK, and NNN with Cytochrome P450 2A13 Based on Molecular Dynamics Simulation. *J. Chem. Inf. Model.* **2019**, *60*, 766–776. DOI: 10.1021/acs.jcim.9b00741
115. Hedegaard, J.; Gunsalus, I. C. Mixed Function Oxidation. *J. Bio. Chem.* **1965**, *240* (10), 4038–4043. DOI: 10.1016/S0021-9258(18)97147-4
116. Podgorski, M. N.; Harbort, J. S.; Coleman, T.; Stok, J. E.; Yorke, J. A.; Wong, L.-L.; Bruning, J. B.; Bernhardt, P. V; De Voss, J. J.; Harmer, J. R.; Bell, S. G. Biophysical Techniques for Distinguishing Ligand Binding Modes in Cytochrome P450 Monooxygenases. *Biochemistry* **2020**, *59* (9), 1038–1050. DOI: 10.1021/acs.biochem.0c00027
117. Mohamed, H.; Ghith, A.; Bell, S. G. The Binding of Nitrogen-Donor Ligands to the Ferric and Ferrous Forms of Cytochrome P450 Enzymes. *J. Inorg. Biochem.* **2023**, *242*, 112168. DOI: 10.1016/j.jinorgbio.2023.112168
118. Sarewicz, M.; Osyczka, A. Electronic Connection Between the Quinone and Cytochrome c Redox Pools and Its Role in Regulation of Mitochondrial Electron Transport and Redox Signaling. *Physiol. Rev.* **2015**, *95* (1), 219–243.
119. Hunter, E. P. L.; Lias, S. G. Evaluated Gas Phase Basicities and Proton Affinities of Molecules: An Update. *J. Phys. Chem. Ref. Data* **1998**, *27* (3), 413–656. DOI: 10.1063/1.556018
120. Shang, Y.; Liu, F.; Wang, Y.; Li, N.; Ding, B. Enzyme Mimic Nanomaterials and Their Biomedical Applications. *ChemBioChem*. **2020**, *21* (17), 2408–2418. DOI: 10.1002/cbic.202000123
121. Raynal, M.; Ballester, P.; Vidal-Ferran Ab, A.; Van Leeuwen, P. W. N. M. Supramolecular Catalysis. Part 2: Artificial Enzyme Mimics. *Chem. Soc. Rev.* **2014**, *43*, 1734–1787. DOI: 10.1039/c3cs60037h.
122. Jane Wang, Z.; Clary, K. N.; Bergman, R. G.; Raymond, K. N.; Dean Toste, F. A Supramolecular Approach to Combining Enzymatic and Transition Metal Catalysis. *Nat. Chem.* **2013**, *6*, 1–4. DOI: 10.1038/NCHEM.1531
123. Schü, C.; Heitmann, G.; Wendler, T.; Krahwinkel, B.; Herges, R. Design and Synthesis of Photodissociable Ligands Based on Azoimidazoles for Light-Driven Coordination-Induced Spin State Switching in Homogeneous Solution. *J. Org. Chem.* **2016**, *81* (3), 1206–1215. DOI: 10.1021/acs.joc.5b02817
124. Thies, S.; Sell, H.; Bornholdt, C.; Schütt, C.; Köhler, F.; Tuczek, F.; Herges, R. Light-Driven Coordination-Induced Spin-State Switching: Rational Design of Photodissociable Ligands. *Chem. Eur. J.* **2012**, *18* (51), 16358–16368. DOI: 10.1002/chem.201201698
125. Buchwald, J. R.; Kal, S.; Civic, M. R.; deJoode, I. M.; Filatov, A. S.; Dinolfo, P. H. Spin Modulation and Electrochemical Behavior of a Five-Coordinate Cobalt(III) Salen Complex. *J. Coord. Chem.* **2016**, *69* (11–13), 1695–1708. DOI: 10.1080/00958972.2016.1175001

126. Kingsbury, C. J.; Senge, M. O. The Shape of Porphyrins. *Coord. Chem. Rev.* **2021**, *431*, 213760. DOI: 10.1016/j.ccr.2020.213760
127. Ghosh, A. Substituent Effects on Valence Ionization Potentials of Free Base Porphyrins: Local Density Functional Calculations and Their Relevance to Electrochemical and Photoelectron Spectroscopic Studies. *J. Am. Chem. Soc.* **1995**, *117* (16), 4691–4699. DOI: 10.1021/ja00121a025
128. Luciano, M.; Brückner, C. Modifications of Porphyrins and Hydroporphyrins for Their Solubilization in Aqueous Media. *Molecules* **2017**, *22* (6), 980. DOI: 10.3390/molecules22060980
129. Weyermann, P.; Gisselbrecht, J.-P.; Boudon, C.; Diederich, F.; Gross, M. Dendritic Iron Porphyrins with Tethered Axial Ligands: New Model Compounds for Cytochromes. *Angew. Chem. Int. Ed.* **1999**, *38* (21), 3215-3219. DOI: 10.1002/(SICI)1521-3773(19991102)38:21<3215::AID-ANIE3215>3.0.CO;2-S
130. Lv, H.; Zhang, X.-P.; Guo, K.; Han, J.; Guo, H.; Lei, H.; Li, X.; Zhang, W.; Apfel, U.-P.; Cao, R. Coordination Tuning of Metal Porphyrins for Improved Oxygen Evolution Reaction. *Angew. Chem. Int. Ed.* **2023**, *62* (38). 202305938. DOI: 10.1002/ANIE.202305938
131. Ludwig, J.; Helberg, J.; Zipse, H.; Herges, R. Azo-Dimethylaminopyridine-Functionalized Ni(II)-Porphyrin as a Photoswitchable Nucleophilic Catalyst. *Beilstein J. Org. Chem.* **2020**, *16*, 2119–2126. DOI: 10.3762/bjoc.16.179
132. Ishihara, S.; Labuta, J.; Van Rossom, W.; Ishikawa, D.; Minami, K.; Hill, J. P.; Ariga, K. Porphyrin-Based Sensor Nanoarchitectonics in Diverse Physical Detection Modes. *PhysChemChemPhys.* **2014**, *16*, 9713–9746. DOI: 10.1039/c3cp55431g
133. Amati, M.; Baerends, E. J.; Ricciardi, G.; Rosa, A. Origin of the Enhanced Binding Capability toward Axial Nitrogen Bases of Ni(II) Porphyrins Bearing Electron-Withdrawing Substituents: An Electronic Structure and Bond Energy Analysis. *Inorg. Chem.* **2020**, *59* (16), 11528–11541. DOI: 10.1021/acs.inorgchem.0c01327
134. Wijesekera, T. P.; Paine III, J. B.; Dolphin, D. Improved Synthesis of Covalently Strapped Porphyrins. Application to Highly Deformed Porphyrin Synthesis. *J. Chem. Soc. Chem. Comm.* **1988**, *53* (7), 1345–1352. DOI: 10.1021/jo00242a001
135. Margarit, C. G.; Schnedermann, C.; Asimow, N. G.; Nocera, D. G. Carbon Dioxide Reduction by Iron Hangman Porphyrins. *Organometallics* **2019**, *38* (6), 1219–1223. DOI: 10.1021/acs.organomet.8b00334
136. Dogutan, D. K.; Kwabena Bediako, D.; Teets, T. S.; Schwalbe, M.; Nocera, D. G. Efficient Synthesis of Hangman Porphyrins. *Org. Lett.* **2010**, *12* (5), 1036–1039. DOI: 10.1021/OL902947H
137. Collman, J. P.; Brauman, J. I.; Doxsee, K. M.; Halbert, T. R.; Bunnenberg, E.; Linder, R. E.; LaMar, G. N.; Del Gaudio, J.; George Lang; Spartalianlc, K. Synthesis and Characterization of "Tailed Picket Fence" Porphyrins. *J. Am. Chem. Soc.* **1980**, *102* (12), 4182–4192. DOI: 10.1021/ja00532a033.
138. Gonzaga, L.; Lopes, F.; Gouveia Júnior, F. S.; Medeiros Holanda, A. K.; Moreira De Carvalho, I. M.; Longhinotti, E.; Paulo, T. F.; Abreu, S.; Bernhardt, P. V; Gilles-Gonzalez, M.-A. et al. Bioinorganic Systems Responsive to the Diatomic Gases O_2 , NO, and CO: From Biological Sensors to Therapy. *Coord. Chem. Rev.* **2021**, *445*, 214096. DOI: 10.1016/j.ccr.2021.214096

139. Hoshino, M.; Laverman, L.; Ford, P. C. Nitric Oxide Complexes of Metalloporphyrins: An Overview of Some Mechanistic Studies. *Coord. Chem. Rev.* **1999**, *187* (1), 75–102. DOI: 10.1016/S0010-8545(98)00228-8
140. Bieza, S.; Mazzeo, A.; Pellegrino, J.; Doctorovich, F. H_2S/Thiols, NO•, and NO^-/HNO: Interactions with Iron Porphyrins. *ACS Omega* **2022**, *7* (2), 1602–1611. DOI: 10.1021/acsomega.1c06427
141. Wayland, B. B.; Olson, L. W.; Felton, H.; Owen, G. S.; Dolphin, D.; Fajer, J.; Amer, J.; Yonetani, T.; Yamamoto, H.; Erman, J. E.; et al. Spectroscopic Studies and Bonding Model for Nitric Oxide Complexes of Iron Porphyrins. *Chem. Comm.* **1973**, *93* (2), 30.
142. Nakagawa, S.; Yashiro, T.; Munakata, H.; Imai, H.; Uemori, Y. Binding of Nitric Oxide to Water-Soluble Iron(III) Porphyrins. *Inorg. Chim. Acta* **2003**, *349*, 17–22. DOI: 10.1016/S0020-1693(03)00037-9
143. Kadish, K. M.; Bottomley, L. A.; Beroiz, D. Reactions of Pyridine with a Series of Para-Substituted Tetraphenylporphyrincobalt and -Iron Complexes. *Inorg. Chem.* **1978**, *17* (5), 1124–1129. DOI: 10.1021/ic50183a006
144. Sahoo, D.; Mazumdar, R.; Pramanik, S.; Banerjee, S.; Patra, R.; Rath, S. P. Modulation of Iron Spin States in Highly Distorted Iron(III) Porphyrins: H-Bonding Interactions and Implications in Hemoproteins. *Dalton Trans.* **2023**, *52*, 8904–8917. DOI: 10.1039/d3dt00846k
145. Shankar, S.; Peters, M.; Steinborn, K.; Krahwinkel, B.; Sönnichsen, F. D.; Grote, D.; Sander, W.; Lohmiller, T.; Rüdiger, O.; Herges, R. Light-Controlled Switching of the Spin State of Iron(III). *Nat. Comm.* **2018**, 4750. DOI: 10.1038/s41467-018-07023-1
146. Kobayashi, M.; Shimizu, S. Cobalt Proteins. *Eur. J. Biochem.* **1999**, *261* (1), 1-19. DOI: 10.1046/j.1432-1327.1999.00186.x
147. Yan, C. W.; Lin, X. Q.; Lin, H. C.; Cao, C. N. Axial Coordination Effects of Pyridine on the Electrochemistry of (TPP)Co in 1,2-Dichloroethane Solution. *Chin. Chem. Lett.* **1997**, *8* (10), 905–908.
148. Truxillo, L. A.; Davis, D. G. Electrochemistry of Cobalt Tetraphenylporphyrin in Aprotic Media. *Anal. Chem.* **1975**, *47* (13), 2260–2267. DOI: 10.1021/AC60363A052
149. Jester, C. P.; Rocklin, R. D.; Murray, R. W. Electron Transfer and Axial Coordination Reactions of Cobalt Tetra(Aminophenyl)Porphyrins Covalently Bonded to Carbon Electrodes. *J. Electrochem. Soc.* **1980**, *127* (9), 1979–1985. DOI: 10.1149/1.2130048
150. Homma, Y.; Ishida, T. A New $S = 0 \rightleftarrows S = 2$ “Spin-Crossover” Scenario Found in a Nickel(II) Bis(Nitroxide) System. *Chem. Mat.* **2018**, *30*, 1835–1838. DOI: 10.1021/acs.chemmater.7b05357
151. Ono, K.; Yoshlzawa, M.; Aklta, M.; Kato, T.; Tsunobuchl, Y.; Ohkoshi, S. I.; Fujita, M. Spin Crossover by Encapsulation. *J. Am. Chem. Soc.* **2009**, *131* (8), 2782–2783. DOI: 10.1021/ja8089894
152. Walker, F. A.; Hui, E.; Walker, J. M. Electronic Effects in Transition Metal Porphyrins. I. The Reaction of Piperidine with a Series of Para- and Meta-Substituted Nickel(II) and Vanadium(IV) Tetraphenylporphyrins. *J. Am. Chem. Soc.* **1975**, *97* (9), 2390–2397.
153. Sahyun, M. R. V; Knox, G. R. SPecies Equilibria in Nickel(II) Porphyrin Solutions: Effect of Porphyrin Structure, Solvent and Temperature. *J. Am. Chem. Soc.* **1962**, *84* (9), 1734–1735. DOI: 10.1021/ja00868a049
154. Sturmeit, H. M.; Cojocariu, I.; Windischbacher, A.; Puschnig, P.; Piamonteze, C.; Jugovac, M.; Sala, A.; Africh, C.; Comelli, G.; Cossaro, A.; et al. Room-Temperature On-Spin-Switching

and Tuning in a Porphyrin-Based Multifunctional Interface. *Small* **2021**, *17* (50), 2104779. DOI: 10.1002/SMLL.202104779
155. Wäckerlin, C.; Tarafder, K.; Girovsky, J.; Nowakowski, J.; Hählen, T.; Shchyrba, A.; Siewert, D.; Kleibert, A.; Nolting, F.; Oppeneer, P. M.; et al. Ammonia Coordination Introducing a Magnetic Moment in an On-Surface Low-Spin Porphyrin. *Angew. Chem.* **2013**, *125* (17), 4666–4669. DOI: 10.1002/ANGE.201208028
156. Venkataramani, S.; Jana, U.; Dommaschk, M.; Sonnichsen, F. D.; Tuczek, F.; Herges, R. Magnetic Bistability of Molecules in Homogeneous Solution at Room Temperature. *Am. Inst. Aeronaut. Astronaut. J.* **2011**, *331* (6016), 445–447. DOI: 10.1126/science.1199492
157. Dommaschk, M.; Schütt, C.; Venkataramani, S.; Jana, U.; Näther, C.; Sönnichsen, F. D.; Herges, R. Rational Design of a Room Temperature Molecular Spin Switch. the Light-Driven Coordination Induced Spin State Switch (LD-CISSS) Approach. *Dalton Trans.* **2014**, *43*, 17395–17405. DOI: 10.1039/c4dt03048f
158. Ludwig, J.; Grobner, J.; Dommaschk, M.; Huber, L. M.; Peters, M. K.; Hovener, J.-B.; Herges, R. Ni(II)Porphyrins as pH Dependent Light-Driven Coordination-Induced Spin-State Switches (LD-CISSS) in Aqueous Solution. *J. Porphyr. Phthalocyanines* **2020**, *24,* 480–488. DOI: 10.1142/S1088424619501803
159. Cozzi, P. G. Metal-Salen Schiff Base Complexes in Catalysis: Practical Aspects. *Chem. Soc. Rev.* **2004**, *33* (7), 410–421. DOI: 10.1039/b307853c
160. Schulz, E. Chiral Cobalt-Salen Complexes: Ubiquitous Species in Asymmetric Catalysis. *Chem. Rec.* **2021**, *21* (2), 427–439. DOI: 10.1002/tcr.202000166
161. Ding, B.; Solomon, M. B.; Leong, C. F.; D'Alessandro, D. M. Redox-Active Ligands: Recent Advances towards Their Incorporation into Coordination Polymers and Metal-Organic Frameworks. *Coord. Chem. Rev.* **2021**, *439*, 213891. DOI: 10.1016/j.ccr.2021.213891
162. Clarke, R. M.; Herasymchuk, K.; Storr, T. Electronic Structure Elucidation in Oxidized Metal-Salen Complexes. *Coord. Chem. Rev.* **2017**, *352*, 67–82. DOI: 10.1016/j.ccr.2017.08.019
163. Zhang, C.; Sutherland, M.; Herasymchuk, K.; Clarke, R. M.; Thompson, J. R.; Chiang, L.; Walsby, C. J.; Storr, T. Octahedral Co(III) Salen Complexes: The Role of Peripheral Ligand Electronics on Axial Ligand Release upon Reduction. *Can. J. Chem.* **2018**, *96* (2), 110–118. DOI: 10.1139/cjc-2017-0277
164. Dyers, L.; Que, S. Y.; Vanderveer, D.; Bu, X. R. Synthesis and Structures of New Salen Complexes with Bulky Groups. *Inorg. Chim. Acta* **2006**, *359*, 197–203. DOI: 10.1016/j.ica.2005.06.068
165. Chaładaj, W.; Kwiatkowski, P.; Jurczak, J. Sterically Modified Chiral (Salen)Cr(III) Complexes-Efficient Catalysts for the Oxo-Diels-Alder Reaction between Glyoxylates and Cyclohexa-1,3-Diene. *Synlett* **2006**, *19*, 3263–3266. DOI: 10.1055/s-2006-951535
166. Elbert, S. M.; Mastalerz, M. Metal Salen-and Salphen-Containing Organic Polymers: Synthesis and Applications. *Org, Mat,* **2020**, *2*, 182–203. DOI: 10.1055/s-0040-1708501
167. Kennedy, B. J.; Mcgrath, A. C.; Murray, K. S.; Skelton, B. W.; White10, A. H. Variable-Temperature Magnetic, Spectral, and X-Ray Crystallographic Studies of "Spin-Crossover" Iron (III) Schiff-Base-Lewis-Base Adducts. Influence of Noncoordinated Anions on Spin-State Interconversion Dynamics in $[Fe(Salen)(Imd)_2]Y$ Species ($Y = ClO_4$, BF_4, PF_6, BPh_4 ; Imd = Imidazole). *Inorg. Chem.* **1987**, *26* (4), 483–495. DOI: 10.1021/ic00251a003
168. Kennedy, B. J.; Fallon, G. D.; Gatehouse, B. K. C.; Murray, K. S. Spin-State Differences and Spin Crossover in Five-Coordinate Lewis Base Adducts of Cobalt(II) Schiff Base

Complexes. Structure of the High-Spin (N,N-o-Phenylenebis(Salicylaldiminato))Cobalt(II)-2-Methylimidazole Adduct. *Inorg. Chem.* **1984**, *23* (5), 580–588. DOI: 10.1021/ic00173a019
169. Zarembowitch, J.; Kahn, O. Magnetic Properties of Some Spin-Crossover, High-Spin, and Low-Spin Cobalt(II) Complexes with Schiff Bases Derived from 3-Formylsalicylic Acid. *Inorg. Chem.* **1984**, *23* (5), 589–593. DOI: 10.1021/ic00173a020
170. Eichhorn, E.; Rieker, A.; Speiser, B.; Stahl, H. Electrochemistry of Oxygenation Catalysts. 3. Thermodynamic Characterization of Electron Transfer and Solvent Exchange Reactions of Co(Salen)/[Co(Salen)]$^+$ in DMF, Pyridine, and Their Mixtures. *Inorg. Chem.* **1997**, *36* (15), 3307–3317. DOI: 10.1021/ic9703336
171. Servedio, L. T.; Lawton, J. S.; Zawodzinski, T. A. An Electrochemical Study of Cobalt-Salen (N,N′-Bis(Salicylidene) Ethylenediaminocobalt(II) in the Oxidation of Syringyl Alcohol in Acetonitrile. *J. Appl. Electrochem.* **2021**, *51* (3), 87–98. DOI: 10.1007/s10800-020-01459-4
172. Jacobsen, E. N. Asymmetric Catalysis of Epoxide Ring-Opening Reactions. *Acc. Chem. Res.* **2000**, *33* (6), 421–431. DOI: 10.1021/ar960061v
173. Katsuki, T. Unique Asymmetric Catalysis of Cis-b Metal Complexes of Salen and Its Related Schiff-Base Ligands. *Chem. Soc. Rev.* **2004**, *33*, 437–444. DOI: 10.1039/b304133f
174. Darensbourg, D. J.; Mackiewicz, R. M.; Phelps, A. L.; Billodeaux, D. R. Copolymerization of CO_2 and Epoxides Catalyzed by Metal Salen Complexes. *Acc. Chem. Res.* **2004**, *37* (11), 836–844. DOI: 10.1021/ar030240u
175. Elder, T.; Bozell, J. J.; Cedeno, D. The Effect of Axial Ligand on the Oxidation of Syringyl Alcohol by Co(Salen) Adducts. *PhysChemChemPhys* **2013**, *15*, 7328–7337. DOI: 10.1039/c3cp44404j
176. Santiago-Rodríguez, Y.; María, C.; Curet-Arana, C. Quantum Mechanical Study of the Reaction of CO_2 and Ethylene Oxide Catalyzed by Metal–Salen Complexes: Effect of the Metal Center and the Axial Ligand. *React. Kinet. Mech. Catal.* **2015**, *116*, 351–370. DOI: 10.1007/s11144-015-0904-6
177. Rajagopalan, B.; Hu, A. E.; Ae, C.; Busch Ae, D. H.; Subramaniam, B. The Catalytic Efficacy of Co(Salen)(AL) in O_2 Oxidation Reactions in CO_2-Expanded Solvent Media: Axial Ligand Dependence and Substrate Selectivity. *Catal. Lett.* **2008**, *123*, 46–50. DOI: 10.1007/s10562-007-9379-z
178. Kal, S.; Filatov, A. S.; Dinolfo, P. H. Electrocatalytic Proton Reduction by a Dicobalt Tetrakis-Schiff Base Macrocycle in Nonaqueous Electrolyte. *Inorg. Chem.* **2014**, *53* (14), 7137–7145. DOI: 10.1021/ic500121f
179. Klaß, M.; Krahmer, J.; Näther, C.; Tuczek, F. Design, Synthesis, and Evaluation of Nickel Dipyridylmethane Complexes for Coordination-Induced Spin State Switching (CISSS). *Dalton Trans.* **2018**, *47*, 1261–1275. DOI: 10.1039/c7dt03952b
180. Brandenburg, H.; Krahmer, J.; Fischer, K.; Schwager, B.; Flöser, B.; Näther, C.; Tuczek, F. Coordination-Induced Spin-State Switching with Nickel(II) Salpn Complexes: Electronic versus Steric Effects and Influence of Intermolecular Interactions. *Eur. J. Inorg. Chem.* **2018**, *2018* (5), 576–585. DOI: 10.1002/ejic.201701281
181. Nowak, R.; Prasetyanto, E. A.; De Cola, L.; Bojer, B.; Siegel, R.; Senker, J.; Rössler, E.; Weber, B. Proton-Driven Coordination-Induced Spin State Switch (PD-CISSS) of Iron(II) Complexes. *Chem. Comm.* **2017**, *53* (5), 971–974. DOI: 10.1039/c6cc08618g
182. Barrett, S. A.; Kilner, C. A.; Halcrow, M. A. Spin-Crossover in [Fe(3-Bpp)2][BF4]2 in Different Solvents - A Dramatic Stabilization of the Low-Spin State in Water. *Dalton Trans.* **2011**, *40*, 12021–12024. DOI: 10.1039/C1DT10876J

183. Kurz, H.; Schötz, K.; Papadopoulos, I.; Heinemann, F. W.; Maid, H.; Guldi, D. M.; Köhler, A.; Hörner, G.; Weber, B. A Fluorescence-Detected Coordination-Induced Spin State Switch. *J. Am. Chem. Soc.* **2021**, *143* (9), 3466–3480. DOI: 10.1021/jacs.0c12568
184. Zhao, Y.; Wang, L.; Xue, S.; Guo, Y. Reversible Coordination-Induced Spin State Switching in a Nickel(II) Complex via a Crystal-to-Crystal Transformation. *Inorg. Chem. Front.* **2022**, *9*, 4127–4135. DOI: 10.1039/d2qi01059c
185. Solis, B. H.; Hammes-Schiffer, S. Theoretical Analysis of Mechanistic Pathways for Hydrogen Evolution Catalyzed by Cobaloximes. *Inorg. Chem.* **2011**, *50* (21), 11252–11262. DOI: 10.1021/IC201842V
186. Mirra, S.; Strianese, M.; Pellecchia, C.; Bertolasi, V.; Monaco, G.; Milione, S. Influence of Coordinated Ligands in a Series of Inorganic Cobaloximes. *Inorg. Chim. Acta* **2016**, *444*, 202–208. DOI: 10.1016/J.ICA.2016.01.040
187. Lawrence, M. A. W.; Celestine, M. J.; Artis, E. T.; Joseph, L. S.; Esquivel, D. L.; Ledbetter, A. J.; Cropek, D. M.; Jarrett, W. L.; Bayse, C. A.; Brewer, M. I.; Holder, A. A. Computational, Electrochemical, and Spectroscopic Studies of Two Mononuclear Cobaloximes: The Influence of an Axial Pyridine and Solvent on the Redox Behaviour and Evidence for Pyridine Coordination to Cobalt(I) and Cobalt(II) Metal Centres. *Dalton Trans.* **2016**, *45*, 10326–10342. DOI: 10.1039/C6DT01583B
188. Pantani, O.; Anxolabéhère-Mallart, E.; Aukauloo, A.; Millet, P. Electroactivity of Cobalt and Nickel Glyoximes with Regard to the Electro-Reduction of Protons into Molecular Hydrogen in Acidic Media. *Electrochem. Comm.* **2007**, *9* (1), 54–58. DOI: 10.1016/J.ELECOM.2006.08.036
189. Panagiotopoulos, A.; Ladomenou, K.; Sun, D.; Artero, V.; Coutsolelos, A. G. Photochemical Hydrogen Production and Cobaloximes: The Influence of the Cobalt Axial N-Ligand on the System Stability. *Dalton Trans.* **2016**, *45*, 6732. DOI: 10.1039/c5dt04502a
190. De March, M.; Demitri, N.; Geremia, S.; Hickey, N.; Randaccio, L. Trans and Cis Influences and Effects in Cobalamins and in Their Simple Models. *J. Inorg. Biochem.* **2012**, *116*, 215–227. DOI: 10.1016/j.jinorgbio.2012.07.018
191. Dolui, D.; Khandelwal, S.; Majumder, P.; Dutta, A. The Odyssey of Cobaloximes for Catalytic H_2 Production and their Recent Revival with Enzyme-Inspired Design. *Chem. Comm.* **2020**, *56*, 8166–8181. DOI: 10.1039/d0cc03103h
192. Niklas, J.; Kohler, L.; Potocny, A. M.; Mardis, K. L.; Mulfort, K. L.; Poluektov, O. G. Electronic Structure of Molecular Cobalt Catalysts for H_2 Production Revealed by Multifrequency EPR. *J. Phys. Chem. C* **2022**, *126* (29), 11889–11899. DOI: 10.1021/ACS.JPCC.2C02576
193. Razavet, M.; Artero, V.; Fontecave, M. Proton Electroreduction Catalyzed by Cobaloximes: Functional Models for Hydrogenases. *Inorg. Chem.* **2005**, *44* (13), 4786–4795. DOI: 10.1021/ic050167z
194. Sato, O.; Tao, J.; Zhang, Y. Z. Control of Magnetic Properties through External Stimuli. *Angew. Chem. Int. Ed.* **2007**, *46* (13), 2152–2187. DOI: 10.1002/anie.200602205
195. Tsukiashi, A.; Min, K. S.; Kitayama, H.; Terasawa, H.; Yoshinaga, S.; Takeda, M.; Lindoy, L. F.; Hayami, S. Application of Spin-Crossover Water Soluble Nanoparticles for Use as MRI Contrast Agents. *Sci. Rep.* **2018**, *8* (1), 14911. DOI: 10.1038/s41598-018-33362-6
196. Schnaubelt, L.; Petzold, H.; Dmitrieva, E.; Rosenkranz, M.; Lang, H. A Solvent- and Temperature-Dependent Intramolecular Equilibrium of Diamagnetic and Paramagnetic States in

Co Complexes Bearing Triaryl Amines. *Dalton Trans.* **2018**, *47* (37), 13180–13189. DOI: 10.1039/c8dt02538j.

197. Schnaubelt, L.; Petzold, H.; Speck, J. M.; Dmitrieva, E.; Rosenkranz, M.; Korb, M. Redox Properties and Electron Transfer in a Triarylamine-Substituted HS-Co^{2+}/LS-Co^{3+} Redox Couple. *Dalton Trans.* **2017**, *46* (8), 2690–2698. DOI: 10.1039/C6DT04748C

198. Troeppner, O.; Lippert, R.; Shubina, T. E.; Zahl, A.; Jux, N.; Ivanović-Burmazović, I. Reverse Spin-Crossover and High-Pressure Kinetics of the Heme Iron Center Relevant for the Operation of Heme Proteins under Deep-Sea Conditions. *Angew. Chem. Int. Ed.* **2014**, *53* (43), 11452–11457. DOI: 10.1002/anie.201406954

199. Kepp, K. P. Heme: From Quantum Spin Crossover to Oxygen Manager of Life. *Coord. Chem. Rev.* **2017**, *344*, 363–374. DOI: 10.1016/j.ccr.2016.08.008

200. Sieber, R.; Decurtins, S.; Stoeckli-Evans, H.; Wilson, C.; Yufit, D.; Howard, J. A.; Capelli, S. C.; Hauser, A. A Thermal Spin Transition in $[Co(Bpy)_3][LiCr(Ox)_3]$ (Ox = C_2O_4(2-); Bpy = 2,2’-Bipyridine). *Chemistry* **2000**, *6* (2), 361–368. DOI: 10.1002/(SICI)1521-3765(20000117)6:2%3C361::AID-CHEM361%3E3.0.CO;2-Y

201. Zerara, M.; Hauser, A. Cobalt(II)-Tris-2,2’-Bipyridine as a Spin-Crossover Complex: Evidence for Cooperative Effects in Three-Dimensional Oxalate Networks. *Chem. Phys. Chem.* **2004**, *5* (3), 395–399. DOI: 10.1002/cphc.200301044

202. Judge, J. S.; Baker, W. A. On the Spin Equilibrium in Bis(2,2′,2″-Terpyridine) Cobalt(II) Salts. *Inorg. Chim. Acta.* **1967**, *1*, 68–72. DOI: 10.1016/S0020-1693(00)93141-4

203. Hendry, P.; Ludi, A. Structure, Reactivity, Spectra, and Redox Properties of Cobalt(III) Hexaamines. In *Advances in Inorganic Chemistry,* Vol. 35. Wiley, 1990; pp 117–198.

204. Turner, J. W.; Schultz, F. A. Intramolecular and Environmental Contributions to Electrode Half-Reaction Entropies of $M(Tacn)_2^{3+/2+}$ (M = Fe, Co, Ni, Ru; Tacn = 1,4,7-Triazacyclononane) Redox Couples. *Inorg. Chem.* **1999**, *38* (2), 358–364. DOI: 10.1021/IC980977T

205. Lord, R. L.; Schultz, F. A.; Baik, M. H. Spin Crossover-Coupled Electron Transfer of $[M(Tacn)_2]^{3+/2+}$ Complexes (Tacn) 1,4,7-Triazacyclononane; M = Cr Mn Fe Co Ni). *J. Am. Chem. Soc.* **2009**, *131* (17), 6189–6197. DOI: 10.1021/ja809552p

206. Leblond, T.; Dinolfo, P. H. Density Functional Theory Prediction of the Electrocatalytic Mechanism of Proton Reduction by a Dicobalt Tetrakis(Schiff Base) Macrocycle. *Inorg. Chem.* **2020**, *59*, 3764–6774. DOI: 10.1021/acs.inorgchem.9b03411

207. Boca, R.; Elias, H.; Haase, W.; Hüber, M.; Klement, R.; Müller, L.; Paulus, H.; Svoboda, I.; Valko, M. Spectroscopic and Magnetic Properties and Structure of a Five-Coordinate, O_2-Binding Cobalt(II) Schiff Base Complex and of the Copper(II) Analogue. *Inorg. Chim. Acta* **1998**, *278* (2), 127–135. DOI: 10.1016/S0020-1693(97)06175-6

208. Böttcher, A.; Takeuchi, T.; Hardcastle, K. I.; Meade, T. J.; Gray, H. B.; Cwikel, D.; Kapon, M.; Dori, Z. Spectroscopy and Electrochemistry of Cobalt(III) Schiff Base Complexes. *Inorg. Chem.* **1997**, *36* (12), 2498–2504. DOI: 10.1021/ic961146v

209. Thordarson, P. Determining Association Constants from Titration Experiments in Supramolecular Chemistry. *Chem. Soc. Rev.* **2011**, *40* (3), 1305–1323. DOI: 10.1039/c0cs00062k

210. *Binding Constant Calculators*. http://supramolecular.org/ (accessed 2020-05-12).

211. *CrysAlisPro*. Rigaku Oxford Diffraction: Tokyo, 2022. https://www.rigaku.com/products/crystallography/crysalis (accessed 2023-06-20).

212. *SCALE3 ABSPACK – A Rigaku Oxford Diffraction Program for Absorption Corrections.* Rigaku Oxford Diffraction: Tokyo, 2017. https://www.rigaku.com (accessed 2023-06-20).
213. Sheldrick, G. M. SHELXT - Integrated Space-Group and Crystal-Structure Determination. *Acta Crystallogr. A* **2015**, *71* (1), 3–8. DOI: 10.1107/S2053273314026370
214. Sheldrick, G. M. Crystal Structure Refinement With SHELXL. *Acta Crystallogr. C* **2015**, *71* (1), 3–8. DOI: 10.1107/S2053229614024218
215. Dolomanov, O. V.; Bourhis, L. J.; Gildea, R. J.; Howard, J. A. K.; Puschmann, H. OLEX2: A Complete Structure Solution, Refinement and Analysis Program. *J. Appl. Crystallogr.* **2009**, *42* (2), 339–341. DOI: 10.1107/S2053229614024218
216. Spek, A. L. Structure Validation in Chemical Crystallography. *Acta Crystallogr. D Biol. Crystallogr.* **2009**, *65* (2), 148–155. DOI: 10.1107/S090744490804362X
217. MacRae, C. F.; Sovago, I.; Cottrell, S. J.; Galek, P. T. A.; McCabe, P.; Pidcock, E.; Platings, M.; Shields, G. P.; Stevens, J. S.; Towler, M.; Wood, P. A. Mercury 4.0: From Visualization to Analysis, Design and Prediction. *J. Appl. Crystallogr.* **2020**, *53* (1), 226–235. DOI: 10.1107/S1600576719014092
218. *Mercury*. Cambridge Crystallographic Data Centre; Cambridge, 2022. http://www.ccdc.cam.ac.uk/ (accessed 2023-06-13).
219. Ketkaew, R.; Tantirungrotechai, Y.; Harding, P.; Chastanet, G.; Guionneau, P.; Marchivie, M.; Harding, D. J. OctaDist: A Tool for Calculating Distortion Parameters in Spin Crossover and Coordination Complexes. *Dalton Trans.* **2021**, *50* (3), 1086–1096. DOI: 10.1039/d0dt03988h
220. Toomsalu, E.; Koppel, I. A.; Burk, P. Critical Test of Some Computational Chemistry Methods for Prediction of Gas-Phase Acidities and Basicities. *J. Chem. Theory. Comput.* **2013**, *9* (9), 3947–3958. DOI: 10.1021/ct4003916
221. Adamo, C.; Barone, V. Toward Reliable Density Functional Methods without Adjustable Parameters: The PBE0 Model. *J. Chem. Phys.* **1999**, *110* (13), 6158–6170. DOI: 10.1063/1.478522
222. *Gaussian 09 Revision D.01.* Gaussian Inc; Dordrecht, The Netherlands, 2009. https://gaussian.com
223. King, A. P.; Gellineau, H. A.; Macmillan, S. N.; Wilson, J. J. Physical Properties, Ligand Substitution Reactions, and Biological Activity of Co(III)-Schiff Base Complexes. *Dalton Trans.* **2019**, *48* (18), 5987–6002. DOI: 10.1039/c8dt04606a
224. Buron-Le Cointe, M.; Hébert, J.; Baldé, C.; Moisan, N.; Toupet, L.; Guionneau, P.; Létard, J. F.; Freysz, E.; Cailleau, H.; Collet, E. Intermolecular Control of Thermoswitching and Photoswitching Phenomena in Two Spin-Crossover Polymorphs. *Phys. Rev. B Condens. Matter Mater. Phys.* **2012**, *85* (6), 064114. DOI: 10.1103/PhysRevB.85.064114
225. Alonso, J. A.; Martínez-Lope, M. J.; Casais, M. T.; Fernández-Díaz, M. T. Evolution of the Jahn-Teller Distortion of MnO6 Octahedra in RMnO3 Perovskites (R = Pr, Nd, Dy, Tb, Ho, Er, Y): A Neutron Diffraction Study. *Inorg. Chem.* **2000**, *39* (5), 917–923. DOI: 10.1021/ic990921e
226. Drew, M. G. B.; Harding, C. J.; McKee, V.; Morgan, G. G.; Nelson, J. Geometric Control of Manganese Redox State. *Chem. Comm.* **1995**, *10*, 1035–1038. DOI: 10.1039/C39950001035
241
227. McCusker, J. K.; Rheingold, A. L.; Hendrickson, D. N. Variable-Temperature Studies of Laser-Initiated $5T_2 \rightarrow 1A_1$ Intersystem Crossing in Spin-Crossover Complexes: Empirical Correlations between Activation Parameters and Ligand Structure in a Series of Polypyridyl Ferrous Complexes. *Inorg. Chem.* **1996**, *35* (7), 2100–2112. DOI: 10.1021/ic9507880

228. Marchivie, M.; Guionneau, P.; Létard, J. F.; Chasseau, D. Photo-Induced Spin-Transition: The Role of the Iron(II) Environment Distortion. *Acta Crystallogr. B* **2005**, *61* (1), 25–28. DOI: 10.1107/S0108768104029751
229. Jacq, J. Schema Carre. Etablissement et Discussion de L'equation Generale de La Courbe Intensite-Potentiel En Regime Stationnaire et Diffusion Convective. *J. Electroanal. Chem.* **1971**, *29* (1), 149–180. DOI: 10.1016/S0022-0728(71)80080-3
230. Dinolfo, P. H.; Williams, M. E.; Stern, C. L.; Hupp, J. T. Rhenium-Based Molecular Rectangles as Frameworks for Ligand-Centered Mixed Valency and Optical Electron Transfer. *J. Am. Chem. Soc.* **2004**, *126* (40), 12989–13001. DOI: 10.1021/ja0473182
231. Hansch, C.; Leo, A.; Taft, R. W. A Survey of Hammett Substituent Constants and Resonance and Field Parameters. *Chem. Rev.* **1991**, *91* (2), 165–195. DOI: 10.1021/cr00002a004
232. McPherson, J. N.; Hogue, R. W.; Akogun, F. S.; Bondì, L.; Luis, E. T.; Price, J. R.; Garden, A. L.; Brooker, S.; Colbran, S. B. Predictable Substituent Control of $Co^{III/II}$ Redox Potential and Spin Crossover in Bis(Dipyridylpyrrolide)Cobalt Complexes. *Inorg. Chem.* **2019**, *58* (3), 2218–2228. DOI: 10.1021/acs.inorgchem.8b03457
233. *NIST Chemistry WebBook*. https://webbook.nist.gov/chemistry/ (accessed 2023-06-07).
234. Shen, J.; Brodbelt, J. Evaluation of Proton-Binding Capabilities of Polyether and Pyridyl Ligands. *J. Mass Spec.* **1998**, *33* (2), 118–129. DOI: 10.1002/(SICI)1096-9888(199802)33:2<118::AID-JMS613>3.0.CO;2-L
235. Kawaguchi, S. Variety in the Coordination Modes of Β-Dicarbonyl Compounds in Metal Complexes. *Coord. Chem. Rev.* **1986**, *70*, 51–84. DOI: 10.1016/0010-8545(86)80035-2.
236. Tocher, J. H.; Fackler, J. P. Electrochemical Investigations of Several Transition Metal Tris-(Acetylacetonate) Complexes. *Inorg. Chim. Acta* **1985**, *102*, 211–215. DOI: 10.1016/S0020-1693(00)86761-4
237. Conradie, J. Redox Chemistry of Tris(β-Diketonate)Cobalt(III) Complexes: A Molecular View. *J. Electrochem. Soc.* **2022**, *169*, 046522. DOI: 10.1149/1945-7111/ac6705
238. Harding, P.; Harding, D. J.; Daengngern, R.; Thurakitsaree, T.; Schutte, B. M.; Shaw, M. J.; Tantirungrotechai, Y. CCDC 829131: Experimental Crystal Structure Determination. Cambridge Crystallographic Data Centre. DOI: 10.5517/ccwts5m
239. Harding, P.; Harding, D. J.; Daengngern, R.; Thurakitsaree, T.; Schutte, B. M.; Shaw, M. J.; Tantirungrotechai, Y. CCDC 829130: Experimental Crystal Structure Determination. Cambridge Crystallographic Data Centre. DOI: 10.5517/ccwts4l
240. D'souza, D. M.; Leigh, D. A.; Papmeyer, M.; Woltering, S. L. A Scalable Synthesis of 5,5′-Dibromo-2,2′-Bipyridine and Its Stepwise Functionalization via Stille Couplings. *Nat. Protoc.* **2012**, *7* (11), 2022–2028. DOI: 10.1038/nprot.2012.122
241. Pedersen, D. S.; Rosenbohm, C. Dry Column Vacuum Chromatography. *Synthesis* **2001**, *2001* (16), 2431–2434. DOI: 10.1055/S-2001-18722.
242. Fulmer, G. R.; Miller, A. J. M.; Sherden, N. H.; Gottlieb, H. E.; Nudelman, A.; Stoltz, B. M.; Bercaw, J. E.; Goldberg, K. I. NMR Chemical Shifts of Trace Impurities: Common Laboratory Solvents, Organics, and Gases in Deuterated Solvents Relevant to the Organometallic Chemist. *Organomet.* **2010**, *29* (9), 2176–2179. DOI: 10.1021/om100106e.
243. *Ethynyltrimethylsilane 98 1066-54-2*. https://www.sigmaaldrich.com/US/en/product/aldrich/218170 (accessed 2024-02-27).

244. Gagnè, R. R.; Koval, C. A.; Lisensky, G. C. Ferrocene as an Internal Standard for Electrochemical Measurements. *Inorg. Chem.* **1980**, *19*, 2854–2855. DOI: 10.1021/ic50211a080.
245. Connor, J. A.; Overton, C. Electronic Spectra and Electrochemistry of Disubstituted 2,2'-Bipyridinetetracarbonylmolybdenum Complexes. Solvent and Substituent Effects. *J. Organomet. Chem*. **1984**, *277*, 277–284. DOI: 10.1016/0022-328X(84)80709-3
246. Hino, J. K.; Ciana, L. Della; Dressick, W. J.; Sullivan B. Patrick. Substituent Constant Correlations as Predictors of Spectroscopic, Electrochemical, and Photophysical Properties in Ring-Substituted 2,2'-Bipyridine Complexes of Rhenium(I). *Inorg. Chem.* **1992**, *31*, 1072–1080. DOI: 10.1021/ic00032a029
247. Yang, X.-J.; Janiak, C.; Rgen Heinze, J.; Drepper, F.; Mayer, P.; Piotrowski, H.; Klü, P. Heteroleptic 5,5'-Disubstituted-2,2'-Bipyridine Complexes of Ruthenium(II): Spectral, Electrochemical, and Structural Investigations. *Inorg. Chem. Acta* **2001**, *318*, 103–116. DOI: 10.1016/S0020-1693(01)00414-5
248. Osipova, E. S.; Gulyaeva, E. S.; Filippov, O. A.; Safronov, S. V; Pavlov, A. A.; Polukeev, A. V; Kirkina, V. A.; Titova, E. M.; Shubina, E. S.; Belkova, N. V. Effect of Ligands on the Lewis Acidity of the Metal and the Binding of N-Bases to Iridium Pincer Complexes. *Eur. J. Inorg. Chem.* **2019**, 1389–1397. DOI: 10.1002/ejic.201801341
249. Chatt, J.; Kan, C. T.; Leigh, G. J.; Pickett, C. J.; Stanley, D. R. Transition-Metal Binding Sites and Ligand Parameters. *J.C.S. Dalton* **1980**, 2032–2038. DOI: 10.1039/DT9800002032
250. Angelici, R. J. Basicities of Transition Metal Complexes from Studies of Their Heats of Protonation: A Guide to Complex Reactivity. *Acc. Chem. Res.* **1995**, *28* (2), 51–60. DOI: 10.1021/ar00050a001
251. Alévêque, O.; Gautier, C.; Levillain, E. Real-Time Absorption Spectroelectrochemistry: From Solution to Monolayer. *Curr. Op. Electrochem.* **2019**, 15, 34–41. DOI: 10.1016/j.coelec.2019.03.015
252. Zheng, H.; Li, K.; Cody, G. D.; Tulk, C. A.; Dong, X.; Gao, G.; Molaison, J. J.; Liu, Z.; Feygenson, M.; Yang, W.; Ivanov, I. N.; Basile, L.; Idrobo, J. C.; Guthrie, M.; Mao, H. K. Polymerization of Acetonitrile via a Hydrogen Transfer Reaction from CH_3 to CN under Extreme Conditions. *Angew. Chem. Int. Ed.* **2016**, *55* (39), 12040–12044. DOI: 10.1002/ANIE.201606198.
253. Zhu, L.; Brassard, C. J.; Zhang, X.; Guha, P. M.; Clark, R. J. On the Mechanism of Copper(I)-Catalyzed Azide–Alkyne Cycloaddition. *Chem. Rec.* **2016**, *16* (3), 1501–1517. DOI: 10.1002/TCR.201600002
254. Meldal, M.; Tornøe, C. W. Cu-Catalyzed Azide-Alkyne Cycloaddition. *Chem. Rev.* **2008**, *108* (8), 2952–3015. DOI: 10.1021/cr0783479
255. Remzi Becer, C.; Hoogenboom, R.; Schubert, U. S. Click Chemistry beyond Metal-Catalyzed Cycloaddition. *Angew. Chem. Int. Ed.* **2009**, *48* (27), 4900–4908. DOI: 10.1002/ANIE.200900755
256. Shiraishi, T.; Kitamura, Y.; Ueno, Y.; Kitade, Y. Synthesis of Oligonucleotides Possessing Versatile Probes for PET Labelling and Their Rapid Ligand-Free Click Reaction. *Chem. Comm.* **2011**, *47*, 2691–2693. DOI: 10.1039/c0cc04979d
257. Mukhopadhyay, C.; Tapaswi, P. K.; Butcher, R. J. A Ligand-Free Copper (1) Catalyzed Intramolecular N-Arylation of Diazoaminobenzenes in PEG-Water: An Expeditious Protocol towards Regiospecific 1-Aryl Benzotriazoles. *Org Biomol. Chem.* **2010**, *8*, 4720–4729. DOI: 10.1039/c0ob00177e

258. Kitamura, Y.; Sakamoto, R.; Shiraishi, T.; Oguri, H.; Ohno, S.; Kitade, Y. Practical Modification of Peptides Using Ligand-Free Copper-Catalyzed Azideealkyne Cycloaddition. *Tetrahedron* **2016**, *72*, 4016–4021. DOI: 10.1016/j.tet.2016.05.029

259. Rodionov, V. O.; Presolski, S. I.; Díaz Díaz, D.; Fokin, V. V; Finn, M. G. Ligand-Accelerated Cu-Catalyzed Azide-Alkyne Cycloaddition: A Mechanistic Report. *J. Am. Chem. Soc.* **2007**, *129* (42), 12705-12712. DOI: 10.1021/ja072679d

260. Palomaki, P. K. B.; Krawicz, A.; Dinolfo, P. H. Thickness, Surface Morphology, and Optical Properties of Porphyrin Multilayer Thin Films Assembled on Si(100) Using Copper(I)-Catalyzed Azide-Alkyne Cycloaddition. *Langmuir* **2011**, *27* (8), 4613–4622. DOI: 10.1021/la104499b

261. Yamaguchi, R.; Hosomi, T.; Otani, M.; Nagashima, K.; Takahashi, T.; Zhang, G.; Kanai, M.; Masai, H.; Terao, J.; Yanagida, T. Maximizing Conversion of Surface Click Reactions for Versatile Molecular Modification on MEtal Oxide Nanowires. *Langmuir* **2021**, *37* (17), 5172–5179. DOI: 10.1021/acs.langmuir.1c00106

262. *Avogadro: An Open-Source Molecular Builder and Visualization Tool*. Pittsburgh, 2017. https://avogadro.cc/ (accessed 2024-01-30).

263. Hanwell, M. D.; Curtis, D. E.; Lonie, D. C.; Candermeersch, T.; Zurek, E.; Hutchison, G. R. Avogadro: An Advanced Semantic Chemical Editor, Visualization, and Analysis Platform. *J.* 2024. *Cheminform.* **2012**, *4* (17), 1-17. DOI: 10.1186/1758-2946-4-17

264. Nitschke, J. R.; Zu, S.; Don Tilley, T.; Chem, D. J. Macrocyclic Chemistry: Aspects of Organic and Inorganic Supramolecular Chemistry. *J. Am. Chem. Soc.* **1995**, *117* (2), 10345–10352. DOI: 10.1021/ja0020310

265. Daum, P.; Murray, R. W. Charge-Transfer Diffusion Rates and Activity Relationships during Oxidation and Reduction of Plasma-Polymerized Vinylferrocene Films. *J. Electroanal. Chem.* **1981**, *85* (4), 389–396.

266. Inzelt, G.; Horányi, G. Combined Electrochemical and Radiotracer Study on the Ionic Charge Transport Coupled to Electron Transfer and Ionic Equilibria in Electroactive Polymer Films on Electrodes. *J. Electrochem. Soc.* **1989**, *136*, 1774–1752.

267. Gooßen, L. J.; Ferwanah, A.-R. S. A Mild and Efficient Protocol for the Catalytic Silylation of Aryl Bromides. *Synlett.* **2000**, *12*, 1801–1803.

268. Suzuki, T.; Takase, K.; Takahashi, K.; Laws, A. P.; Taylor, R. Electrophilic Substitution in Annulenes. Part 4.' Transmission of Substituent Effects in 1,6-Methano[LO]Annulene, Determined via Protiodesilylation: Evidence for Substantial C(l)-C(6) Transannular Orbital Interaction. *Perkin Trans. II* **1988**, 697–700. DOI: 10.1039/P29880000697

269. Jia, X.; Nedzbala, H. S.; Bottum, S. R.; Cahoon, J. F.; Concepcion, J. J.; Donley, C. L.; Gang, A.; Han, Q.; Hazari, N.; Kessinger, M. C.; Lockett, M. R.; Mayer, J. M.; Mercado, B. Q.; Meyer, G. J.; Pearce, A. J.; Rooney, C. L.; Sampaio, R. N.; Shang, B.; Wang, H. Synthesis and Surface Attachment of Molecular Re(I) Complexes Supported by Functionalized Bipyridyl Ligands. *Inorg Chem.* **2022**, *62* (5), 2359-2375. DOI: 10.1021/acs.inorgchem.2c041373

APPENDIX A. LIGAND TITRATION CURVE FITS

Table 4: Collected bindfit links for the N-containing heterocycles bound to $\mathrm{Co^{III}Sln^{+}}$ and $\mathrm{Co^{II}Sln}$ studied in Chapter 3.

Host Complex	Ligand	Bindfit Link
$\mathrm{Co^{III}Sln^{+}}$	**Py trial 1**	http://app.supramolecular.org/bindfit/view/9e9d41b6-7b8b-4cf5-990f-0bf5191a66f2
	Py trial 2	http://app.supramolecular.org/bindfit/view/bbd1956d-dbd0-4945-b1bb-7b276b87b30e
	Py trial 3	http://app.supramolecular.org/bindfit/view/85debc6c-df86-4b67-9749-d256589e1091
	Py trial 4	http://app.supramolecular.org/bindfit/view/98f85df3-f35e-4580-bd51-1764e3f5f63b
	Im trial 1	http://app.supramolecular.org/bindfit/view/09ee6464-7cfc-4d51-ade6-d3b1f882889b
	Im trial 2	http://app.supramolecular.org/bindfit/view/5af4cebd-0d47-4e5a-8ad1-ad1298323824
	Im trial 3	http://app.supramolecular.org/bindfit/view/2352a47e-f867-42b4-bcb2-52027e97f32c
	Im trial 4	http://app.supramolecular.org/bindfit/view/19f3ba8c-4352-4529-aff6-b594bb881954
	Im trial 5	http://app.supramolecular.org/bindfit/view/e51658bd-da9d-4f20-9653-a37b462fd9f9
	Pic trial 1	http://app.supramolecular.org/bindfit/view/3c24c2ff-8c1b-4726-b653-6b9647f9de99
	Pic trial 2	http://app.supramolecular.org/bindfit/view/eb2c08bc-7795-412d-b831-2c158f9b9294
	Pic trial 3	http://app.supramolecular.org/bindfit/view/b264046f-5e48-446d-91ce-ad8fd10dfd4b
	Pryzl trial 1	http://app.supramolecular.org/bindfit/view/efc2a21e-aa57-49d5-9c92-18ba03ea51ea
	Pryzl trial 2	http://app.supramolecular.org/bindfit/view/46f52dd7-47d3-4954-96c8-e9aa1a2a0f64
	Pryzl trial 3	http://app.supramolecular.org/bindfit/view/7a9210a6-3e0d-4300-9cee-2a55e76dbab7
	Pryzn trial 1	http://app.supramolecular.org/bindfit/view/206fda01-12f9-401c-ba7a-298e5e6ebfc9
	Pryzn trial 2	http://app.supramolecular.org/bindfit/view/1e0ca2cb-e853-4883-bcd3-ff537824577e
	Cnpy trial 1	http://app.supramolecular.org/bindfit/view/469c1889-18fa-4e5c-bb71-c41e067eab9d
	Cnpy trial 2	http://app.supramolecular.org/bindfit/view/5e1ef86f-02c9-478d-9297-12e4026570fc
	Cnpy trial 3	http://app.supramolecular.org/bindfit/view/d2f0de3e-e120-4a69-bb52-313f81d3d319
	Ampy trial 1	http://app.supramolecular.org/bindfit/view/17908546-311b-4381-9f8c-0957fc08ea9a
	Ampy trial 2	http://app.supramolecular.org/bindfit/view/bba27482-f9d1-4fe9-892d-25f0e933bf60
	Ampy trial 3	http://app.supramolecular.org/bindfit/view/01efbfc4-46d8-4f9f-9768-d5741fcc75c8
	Bpy trial 1	http://app.supramolecular.org/bindfit/view/49c682cf-b517-44ad-b558-17f81675fee6
	Bpy trial 2	http://app.supramolecular.org/bindfit/view/6422c6f4-dbd1-405a-8efa-6f141afb91c2
	Dmapy trial 2	http://app.supramolecular.org/bindfit/view/de7330dc-10f1-496a-bb70-c2c35ed022bd
	Dmapy trial 3	http://app.supramolecular.org/bindfit/view/9a99201c-13b4-421c-8147-9e39c9ee83ee
	Dmapy trial 4	http://app.supramolecular.org/bindfit/view/efa6b584-0736-4034-a1bb-5d6576ee6ed5
	Dmapy trial 5	http://app.supramolecular.org/bindfit/view/4219d492-e83f-4e01-8d49-1c3ff92de4b0
	Bix trial 1	http://app.supramolecular.org/bindfit/view/70918de1-a42e-4ce1-a0b7-24a5ff7d3da3
	Bix trial 2	http://app.supramolecular.org/bindfit/view/486803a1-9e07-4b33-8346-8d8e2b1cc19f
	Bix trial 3	http://app.supramolecular.org/bindfit/view/c875ee2b-b648-490a-8f4d-10b156835e70
$\mathrm{Co^{II}Sln}$	**Py Trial 1**	http://app.supramolecular.org/bindfit/view/0d43c2c2-d439-4405-b471-8e48c59f
	Im Trial 1	http://app.supramolecular.org/bindfit/view/5d4bf8fd-1edf-4512-a0f0-363eb27dd0e0
	Im Trial 2	http://app.supramolecular.org/bindfit/view/e55f286d-0203-48a5-b666-b161769bae0b
	Pic Trial 1	http://app.supramolecular.org/bindfit/view/0fb3408a-320d-45cb-9f70-b8d58307a147
	Dmapy Trial 1	http://app.supramolecular.org/bindfit/view/0fb3408a-320d-45cb-9f70-b8d58307a147
	Dmapy Trial 2	http://app.supramolecular.org/bindfit/view/0fb3408a-320d-45cb-9f70-b8d58307a147
	Dmapy Trial 3	http://app.supramolecular.org/bindfit/view/849157d0-cee1-4d2d-9c30-1c3c908cdea
	Dmapy Trial 4	http://app.supramolecular.org/bindfit/view/849157d0-cee1-4d2d-9c30-1c3c908c
	Ampy Trial 1	http://app.supramolecular.org/bindfit/view/a859478e-3c42-420c-837d-ed536b65d28
	Bix Trial 1	http://app.supramolecular.org/bindfit/view/6fc0f7eb-21cd-469d-b9ca-06d9232abf11
	Bpy Trial 1	http://app.supramolecular.org/bindfit/view/33fa7639-b21c-42d2-a217-9982e98cc903
	Bpy Trial 2	http://app.supramolecular.org/bindfit/view/99a864b9-5966-419c-85bf-0255ab57c2fb

ProQuest Number: 31145948

INFORMATION TO ALL USERS
The quality and completeness of this reproduction is dependent on the quality
and completeness of the copy made available to ProQuest.

Distributed by ProQuest LLC (2024).
Copyright of the Dissertation is held by the Author unless otherwise noted.

This work may be used in accordance with the terms of the Creative Commons license
or other rights statement, as indicated in the copyright statement or in the metadata
associated with this work. Unless otherwise specified in the copyright statement
or the metadata, all rights are reserved by the copyright holder.

This work is protected against unauthorized copying under Title 17,
United States Code and other applicable copyright laws.

Microform Edition where available © ProQuest LLC. No reproduction or digitization
of the Microform Edition is authorized without permission of ProQuest LLC.

ProQuest LLC
789 East Eisenhower Parkway
P.O. Box 1346
Ann Arbor, MI 48106 - 1346 USA